# Memristors and Superconducting Quantum Interference Filters in RF Systems

by

Lin Wang

Department of Electrical and Computer Engineering
Duke University

Date: _____

Approved:

_____
Qing Huo Liu, Supervisor

_____
William Joines

_____
Martin A. Brooke

_____
Gary Ybarra

_____
John Trangenstein

Dissertation submitted in partial fulfillment of the requirements for the degree of
Doctor of Philosophy in the Department of Electrical and Computer Engineering
in the Graduate School of Duke University
2014

ABSTRACT

(Electrical and Computer Engineering)

# Memristors and Superconducting Quantum Interference Filters in RF Systems

by

Lin Wang

Department of Electrical and Computer Engineering
Duke University

Date: _____

Approved:

_____
Qing Huo Liu, Supervisor

_____
William Joines

_____
Martin A. Brooke

_____
Gary Ybarra

_____
John Trangenstein

An abstract of a dissertation submitted in partial fulfillment of the requirements for
the degree of Doctor of Philosophy in the Department of Electrical and Computer
Engineering
in the Graduate School of Duke University
2014

# Abstract

Complex nonlinear dynamical systems have been appeared in many fields of science and engineering. We are curious about two specific instances of those systems. Those two instances connect memristors and Josephson junctions to the electromagnetic fields. The first instance investigated microstrip patch antenna embedding dual memristors. This hybrid system produces broadband radiation in a narrow band radiation structure. The second one studies the novel ultra-sensitive magnetic field receiver implemented by superconducting quantum interference filters (SQIFs).

For the first instance, we notice that memristor has been proposed as the fourth passive element. We start with investigating the circuit model of this memristive element. Then, we embedded this circuit model into an EM radiation structure. We first report an efficient broadband electromagnetic radiation from a narrowband microstrip patch antenna. The directly modulated microstrip patch antenna system with dual memristors is calculated by using an integrated full-wave finite-difference time-domain solver and an embedded SPICE3 solver. Nonlinear transient electromagnetic responses are analyzed. The radiation frequency spectrum demonstrates the broadband radiation performance from the narrowband antenna system. We predict that the conceptual challenge of high frequency memristors will stimulate pioneering work in the fields of microwave and memristors.

For the second one, we predict that superconducting quantum interference filters (SQIFs) might play a key role in future quantum wireless communication systems.

We analyze the dynamic behavior of this large-scale 2D DC SQIF (two-dimensional superconducting direct current quantum interference filter) array in a dynamic electromagnetic environment. The investigation under this framework starts from the SPICE circuit description of a RCSJ (resistively and capacitively shunted junction) model of a Josephson junction and then extends to the 2D SQIF with few device parameters. We separate the interface and the implementation of 2D DC SQIF. This approach can significantly improve circuit-level design efficiency of 2D SQIF array and ultimately allows us to accelerate the hybrid design with an electromagnetic radiation structure. Our findings on the average voltage response of this device offer compelling evidence that the bias static magnetic field plays a key role in designing an effective far-field magnetic field sensor. Since this device can function as both a robust and sensitive low noise pre-amplifier as well as a receiving antenna which only senses the magnetic field component of far-field electromagnetic wave signals, we call it magnetic-antenna or B-antenna. We believe that our research not only directly benefits the sensor design for Information Operations/Signals Intelligence (IO/SIGINT) applications in Very High Frequency/Ultra High Frequency (VHF/UHF) bands, but also opens new dimension of novel ultra-sensitive receiving antenna technology.

To the times.

# Contents

# List of Tables

# List of Figures

xvi

# List of Abbreviations and Symbols

Symbols

**E**      The electric field. SI unit: Volts per meter (V/m)

**H**      The magnetic field. SI unit: Amperes per meter (A/m)

**B**      The magnetic field. SI unit: Tesla or Newton per ampere · meter (N/Am). For example $B = \mu_0 H = 4\pi \times 10^{-7} \times 0.2 = 2.5133 \times 10^{-6}$ T

Gauss      $1\ gauss = 1 \times 10^{-4}$ Tesla

# Acknowledgements

I would like to acknowledge my parents who give me the birth and then I have the possibility to complete this Ph.D. work.

During the years at Duke, I am extremely grateful for the guidance and research resources from my supervisor, Dr. Qing Huo Liu. The professional skills and personal lessons that I learned from him will be invaluable in my future life path.

I would also like to thank Professors William Joines, Gary Ybarra, Matthew Reynolds, Dev Palmer, Martin A. Brooke and John Trangenstein for their guidance and the feedback throughout my research.

I appreciate my officemates, Zhe Li, Zhiru Yu and Jibing Zhen for our joys and friendship. I am thankful to Wave Computation Technologies, Inc. for providing simulation tools and Dr. Tian Xiao and Dr. Mengqing Yuan for their technical support.

Finally, a special thank you message to Pei-Wen Chen — for your loving, lasting spiritual accompany and the unforgotten happiness. The whole experience with you is an astonishing miracle!

# 1

# Introduction

It is interesting that we are going to treat the mixture of traditional antennas, electrical circuit elements and SQIFs in a view of the system and network. The antenna, circuit elements or SQIFs could be one node in the framework of system and network. The physical relation among nodes could be serial or parallel, coupled or decoupled, small scale or large scale. This perspective of system and network adds a higher level of abstraction and therefore open new dimension of research territory.

Before we discuss the details of specific examples, it is useful that we review certain nonlinear dynamical features arising in complex systems and networks.

First, we observed that complex systems and networks have been aroused in a variety of nature science and engineering fields. These fields include neuroscience, social science, meteorology, chemistry, physics, computer science, psychology, artificial life, evolutionary computation, economics, earthquake prediction, molecular biology and electrical engineering[9, 14, 20, 23, 49, 66, 3, 22, 26, 47, 56]. The existence of complex systems and networks demonstrates the diversity of the world. Furthermore, the cross-discipline study in different scientific and engineering fields opens new vitality in complex systems and networks.

The natural question arouses. We need first answer what is a system. And then what is a network. How do we analyze those systems and networks? Finally, in the particular systems and networks, what can we benefit from their nonlinear/linear dynamical behavior?

## 1.1 Systems and Networks

Before we are going to answer those questions and dive into the inner structure and behavior of complex system and network, we would like to clarify some fundamental concepts. First, let us consider what we mean by *system*. What is system? It would be nice if we could find a good definition of system. Newbury house defines "system" as "a group of related parts" [1], which does not be very useful. Alternative definition gives that a system is an object with varying degrees of complexity, which does not give us future far [4]. A proper view is that a system has certain logical relations which connect one element to another one. This logical relation is often refined precisely by a mathematical expression.

Following the introduction of a system, the second concept which we want to illustrate is *network*. We have seen a lot of objects ending by the name of network. For example, a national power network delivers the electricity power to target users. Social network connects people with the information flow. Neural network could process the external data and build the data model. So, what is a network? Again, Newbury house defines "a network" as "a system of connected travel routes or communication lines"[2], which is obviously not useful. However, we could obtain an intuition view from a geometrical picture.

For a specific example, Fig. 1.1 shows a regular and random network [57]. From this figure, we observed that a network is a topological structure with connecting

---

[1] http://nhd.heinle.com/Definition.aspx?word=system

[2] http://nhd.heinle.com/Definition.aspx?word=network

nodes. As data organized in data structure, in an abstract way, those topological structures consist of large amounts of nodes and edges. Nodes can be any objects: air stations or circuit elements; the edge can be directional, or undirectional, or weighted.

Finally, we turn to the difference between a network and a system. A network is a subset of a system. A network is a special class of a system with a different implication. System gives a broader view of the study object. Although we will not cover the detail of network and system theory, we perceive the conceptual difference between a network and a system. We will use both concepts to describe an antenna system embedding dual memristors and a magnetic antenna based on the Josephson junction network.

## 1.2 Linear System and Nonlinear System

In practice, what really matters is not how we define a *system*, but how we express it, that it makes a system more specific and meaningful. One way to express a system is to add some determiners and therefore to narrow down the field.

For example, we say a *linear system.* So, what is it? It is an abstract concept which summarizes the mathematical relation among variables. For an oscillation electrical circuit consisting of a resistor, a capacitor and an inductor, this linear system is modeled by the differential equation

$$L\frac{dq^2}{dt^2} + R\frac{dq}{dt} + q/C = V(t). \tag{1.1}$$

The left side of above equation has combinational operations of the variable $q$. If we substitute $(q + p)$ for $q$, we obtain

$$\mathcal{L}(q + p) = L\frac{d(q+p)^2}{dt^2} + R\frac{d(q+p)}{dt} + (q+p)/C. \tag{1.2}$$
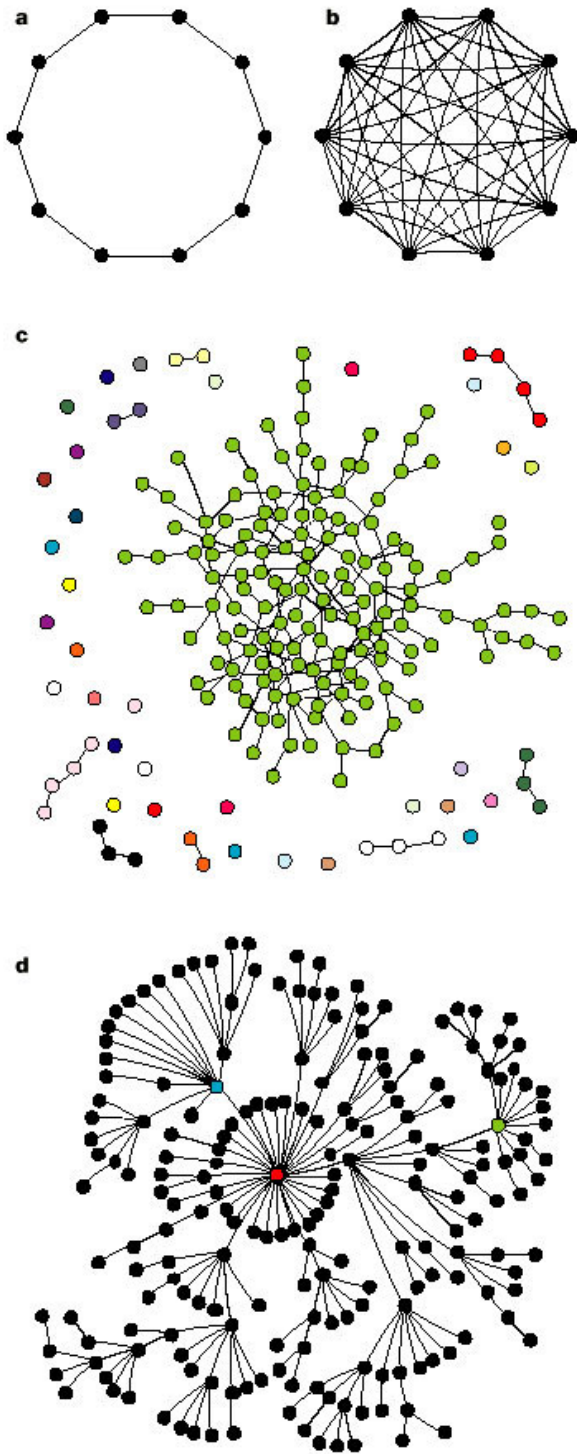
FIGURE 1.1: Illustration of regular and random network architectures. (a), Ring of ten nodes connected to their nearest neighbors. (b), Graph of ten nodes. (c), Random graph islands. (d), Scale-free trees

Here we use the operator $\mathcal{L}$ to replace the whole operation of the right side of Equ. 1.2.

It is obvious that we have two statements on the operator $\mathcal{L}$

$$\mathcal{L}(q + p) = \mathcal{L}(q) + \mathcal{L}(p) \tag{1.3}$$

$$\mathcal{L}(aq) = a\mathcal{L}(q). \tag{1.4}$$

In generalized situations, $\mathcal{L}$ may include more derivatives and other operations. The justification of the linear system is whether Equ. 1.3 and 1.4 are satisfied or not.

If above superposition principle is broken, we say a nonlinear system. Those equations of nonlinear systems can be nonlinear algebraic equations, nonlinear recurrence relations and nonlinear differential equations. Many natural systems can be modeled by nonlinear systems, which results in uncommon dynamical patterns. For example, the weather movement can be chaotic due to the nonlinear behavior of this kind of system.

## 1.3 Dynamical System

Alternatively, how can we make a system more specific and meaningful? We may say a *dynamical system*. A dynamical system is *not* a stationary system. So, what is it? It is an abstract mathematical concept which summarizes the time dependence of a point in a geometrical space. From the above description, we obtain some interesting information. *time* tells us *when* and *geometry* tells us *where*. For example, the flow of water in a pipe can be described as a dynamical system. For generalization, the geometry information can be replaced by any variables.

We have introduced the dynamical system. Let us look at some interesting concepts and properties of a dynamical system. The first concept is about the *state* in a dynamical system. A state $x(t)$ at a given time $t$ can be represented by a vector. From the geometrical perspective, a state $x(t)$ is a point in a state space.

The dynamical behavior of a system is that how does a current state evolve into the future state after a certain time interval. The trick of evolving rules is not random but deterministic. For random cases, an evolution process of a state might belong to Markov Chain process, which is beyond our discussion in this dissertation. So, what is a deterministic process? It just can be summarize into one sentence: if you know the current state value, the future state can be predicted by certain steps of rules. The vague rules can be further clarified under the framework of the system equations.

Let us do an interesting movement in our brain. According to the fixed rules, if we plot the initial state $X_0$ of a dynamical system, we could deduce and plot the next state $X_1$, and the next next state $X_2$ and so on. We connected all states one by one in the space and then we will get a trace, which is called a trajectory or an orbit. Either trajectory or orbit is a qualitative and geometrical concept, which gives the visualized geometrical structure of states. The concept of trajectory for the dynamical system is originated from the contribution of Poincaré. Why does this concept draw huge attention just in recent decades? The direct clue is that human being was discovering variously astonishing phenomena, such as classical chaos, multistability, aperiodic oscillations, amplitude death and solitons. How do we solve a dynamical system? Solving general dynamical systems by hand is difficult. In the early century, we don't have right calculation tools to capture the quantitative behavior. The computer or computing machine also does not exist and therefore no corresponding scientific algorithms are available. Finding the motion pattern of a state of a dynamical system becomes extremely difficulty. So what's the situation now? Many numerical algorithms running on the personal computer or cloud can easily handle this solvable difficulty and capture the trajectory of the dynamical system with thousands of equations.

We had illustrated the situation of computing trajectory. Let us briefly point out

some applied aspects beyond the trajectory. We might know the qualitative properties of a trajectory, but we still need understand the complexity of an individual trajectory. Let us consider a trivial example, how does a trajectory response to a small perturbation or change of system initial value. Is this trajectory stable? This related analysis is own to the study of *Lyapunov stability* of a dynamical system. We want to stop here and come back again in the following chapter when we talked about the possible stability issue in a memristor system.

It is worth to have a space peek a trajectory shifting from one pattern to another one, which we call the phase transition. The pattern of trajectory might be periodic; of course, the trajectory might be other in other patterns. For example, the bifurcation might happen if parameters of the dynamical system are slightly changed. Or a periodic motion of the fluid flow is shifted into the turbulence movement. I will leave the space since this whole field is well introduced in ergodic theory.

## 1.4 Special Cases: Memristor Systems and Josephson Junction Networks

Surprising enough, in spite of the tremendous amount of experimental and theoretic research that has been conducted in electromagnetic field, antenna, circuit, superconducting quantum interference and microwave engineering. However, these researches are studied independently. It is possible for us to condense the enormous mass of cross-discipline knowledge to a higher recognition level. That is, to find shared patterns which might leverage existing information and knowledge. Even so, all research fields are highly dynamically developed; it is so hard to grasp all details and relationship of each part of subject to each other and to control the complexity. We have certain depth of antenna theory. It is our work to find more insight by starting exploring embedding complex nonlinear dynamical systems into antennas and even designing new type antenna based on the system and network. Following these

preliminary commentary, the first part therefore investigates the hybrid memristor-antenna system. The second part studies the novel complex antenna system arising from the network of Josephson Junctions.

The following paragraph will introduce the memristor system. Recently, the memristor has been proposed as the fourth passive electrical element. The governing equations of a memristor are two coupled differential equations. We investigated the circuit model based on the equations of a memristive system. The circuit model is then embedded into a radiation structure. We first report on an efficient broadband electromagnetic radiation from a narrowband microstrip patch antenna. The directly modulated microstrip patch antenna system with dual memristors is calculated by using an integrated full-wave finite-difference time-domain method with an embedded SPICE3 solver. Nonlinear transient electromagnetic response is analyzed. The radiation frequency spectrum demonstrates the broadband radiation performance from the narrowband antenna system. We predict that the conceptual challenge of high frequency memristors will stimulate pioneering work in microwave and material fields.

After illustrating the memristor system in a patch antenna, we explore a new type antenna: magnetic antenna (B-antenna) based on Josephson junction network. The network of Josephson junction is named as superconducting quantum interference filters (SQIFs), which plays a key role in future quantum wireless communication. The feature of the SQIF is to receive a tiny magnetic signal but insensitive to the electromagnetic signal wavelength. We developed a fundamental modeling framework. First, we investigated the equivalent resistively shunted junction (RSJ) model and superconducting quantum interference device (SQUID). Our model considers physical parameters, such as critical current, magnetic quantum effects, variations of parallel resistance and capacitance, self and mutual inductances. To capture the tiny dynamic magnetic field, 1D and 2D superconducting quantum interference

(SQIFs) hybrid E-B system is proposed. This E-B antenna system can be used as high-precision positioning and ultra-sensitive antenna in the battlefield environment.

## 1.5   Research Contributions

The innovation of traditional antennas poses a big challenge for researchers and practitioners. The breakthrough of wireless communication and sensing technology need new creations of antennas. Historically, primary antenna types, such dipoles, monopoles, patches and their derivatives, are still used in current products. As all we know, the dynamic behaviors of those antennas are governed by Maxwells equation. How do I make a breakthrough in this well-researched field? I observed two issues which might be turned into a good research topic. One issue is that there are not enough creative research efforts focusing on embedding the nonlinear electronic devices into antennas; another one is that it is hard to find promising alternative methods to receive electromagnetic signal due to the fundament physics limitation. My work provides actionable solutions for above issues and pushes traditional antennas into more fruitful research world.

In the following sections, I summarize my major contributions. Overall, I built two complex nonlinear antenna systems and analyzed the dynamic behaviors of two systems. For the first system, the patch antenna embedded dual memristors allows a nonlinear transient electromagnetic radiation. For the second one, I extend the investigation of two-dimensional superconducting quantum interference filters (2D SQIFs) in a dynamic electromagnetic environment.

### 1.5.1   Embedded Dual Memristors into the Patch Antenna

Major contributions are listed here:

1. Demonstrated that the memristor, as a fourth passive circuit element, has a huge potential for use in radio frequency systems.

2. Built a new nonlinear element-on-antenna research territory by integrating two memristors into the patch antenna. In previous research, researchers are focusing on the non-volatile storage applications by using memristors as digital logic and memory circuits.

3. Developed two alternative SPICE circuit models, the closed-loop OP-AMP model and the integrator model, to simulating a normalized current-controlled memristor. Comparing with traditional numerical methods, two models accelerates the design speed for the large scale memristor circuit system.

4. Analyzed the numerical stability when we use a SPICE solver.

5. First theoretically identify the broadband radiation modulated by dual-memristor.

### 1.5.2  2D Superconducting Quantum Interference Filter Framework

Major contributions are listed here:

1. Extended the analysis of a large-scale 2D SQIF (two-dimensional superconducting quantum interference filter) in a dynamic electromagnetic environment.

2. Identified the linear operation region and the saturation region. Our findings offer compelling evidence that the biased static magnetic field plays a key role in designing an effective far-field magnetic field sensor.

3. First investigated the geometric effects with three array configurations: a $20 \times 10$ array, a $20 \times 15$ array and a $15 \times 20$ array.

4. First investigated electrical parameter effects for a 2D SQIF: the bias current and the junction resistance.

5. First Extracted the envelop signal from the transient voltage signal by a probabilistic amplitude demodulation (PAD) technique.

6. First designed an impedance-matched U-slot patch antenna with its maximum radiation direction points to the $z$ direction and a minimum magnetic field value component $H_x = 0.006$ A/m.

7. Demonstrated that a 2D SQIF can function as both a robust and sensitive low noise pre-amplifier as well as a receiving antenna. Since it only senses one directional magnetic field component of a far-field electromagnetic wave signal, we call it a directed magnetic-antenna or a directed B-antenna.

8. Designed a co-mingled E and B field antennas system and analyzed the inference from the near-field patch antenna.

## 1.6   Directions of Future Works

In our work, we have seen that the cross-discipline investigation opens a promising and exciting research field beyond traditional antenna research fields. This interesting combination, either through embedding complex nonlinear dynamics systems or developing new sensing SQIF network, inspires the future antenna structures. We will continue to investigate theory, optimize the design process, seek novel applications based on current work. Here are some encouraging directions for future explorations:

- Investigate nonlinear chaotic radiation based on memristors.

- Intelligent computing with memristor synapses.

- Numerical analysis for a more complex memristor model.

- Evaluate the critical SQIF parameters with experiments.

- Novel dynamical magnetic field detecting system with SQIFs.

# 2

# Embedding Memristor into Antennas

## 2.1   Background

Recently, the memristor (the abbreviation for memory resistor), displaying remarkable electronic properties, has attracted several studies due to its extraordinary role in microwave applications[28, 8]. In 1971, based on symmetry consideration, L. Chua first postulated the existence of a two-terminal *memristor* $M$ as the missing fourth passive electrical circuit element besides the resistor $R$, capacitor $C$, and inductor $L$[17]. As shown in Fig. 2.1, memristors is one of more general class of dynamical devices, memristive systems. Note that R, C, L and M can be functions of the independent variable in their defining equations, yielding nonlinear elements. For example, a charge-controlled memristor is defined by a single-valued function M(q). Specifically, this fundamental circuit element theoretically unfolds the hidden constitutive relationship $F(q, \varphi) = 0$ between the electric charge $q$ and the magnetic flux $\varphi$. [46, 45] The unique feature of a memristor is that it behaves as a linear resistor with memory; technically, the resistance (or conductance) at a given time $t$ depends on the time integral of the entire history of its current (or voltage) value. Further-
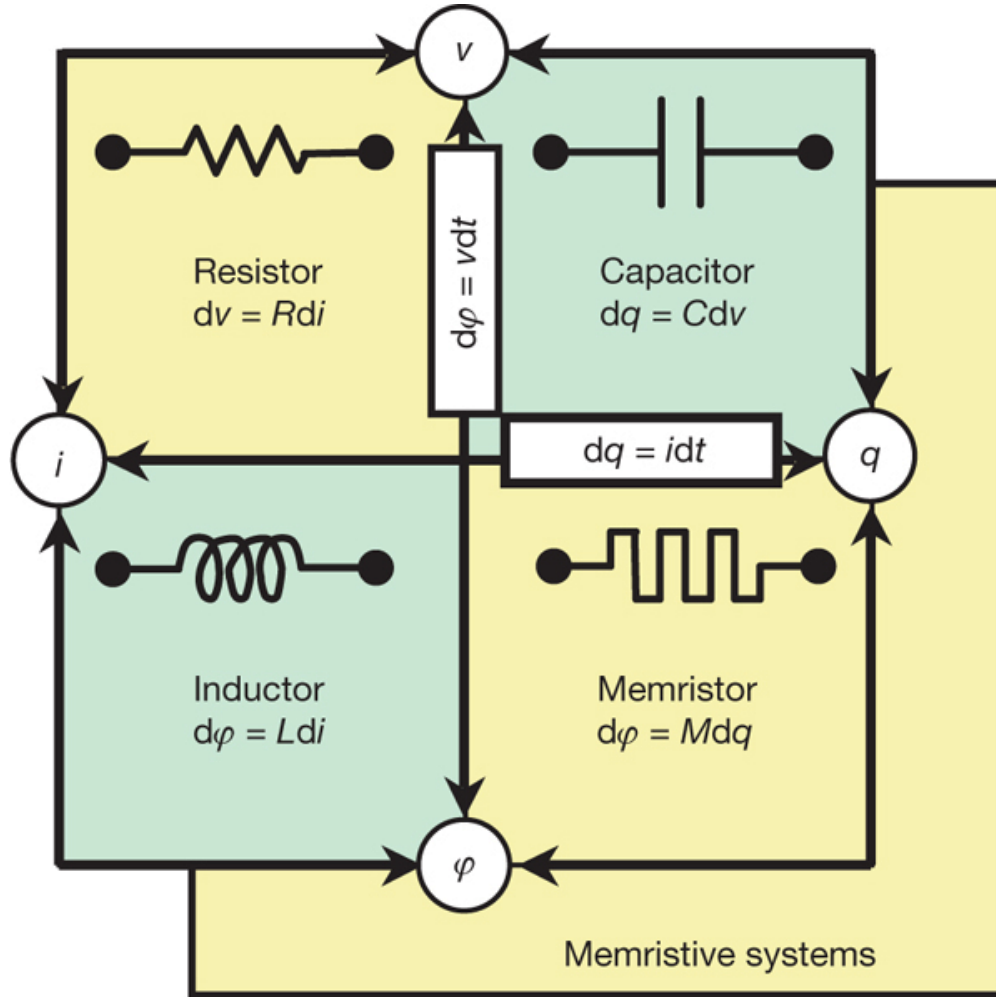
FIGURE 2.1: The four fundamental two-terminal circuit elements: resistor, capacitor, inductor and memristor.[10]

more, a broader quantitative description of a memristor has been mathematically generalized into a memristive system.

Strukov *et. al* from Hewlett-Packard (HP) clearly shows a simplified physical model, which is based on a thin film of titanium dioxide[59], to characterize nanoscale memristive effects, such as negative differential resistance, multiple conductance and switching and hysteretic conductance. Fig. 2.2 shows an array of 17 oxygen-depleted titanium dioxide memristors built at HP Labs, which is imaged by an atomic force microscope. The wires are about 50 nm, or 150 atoms, wide. Electric current through
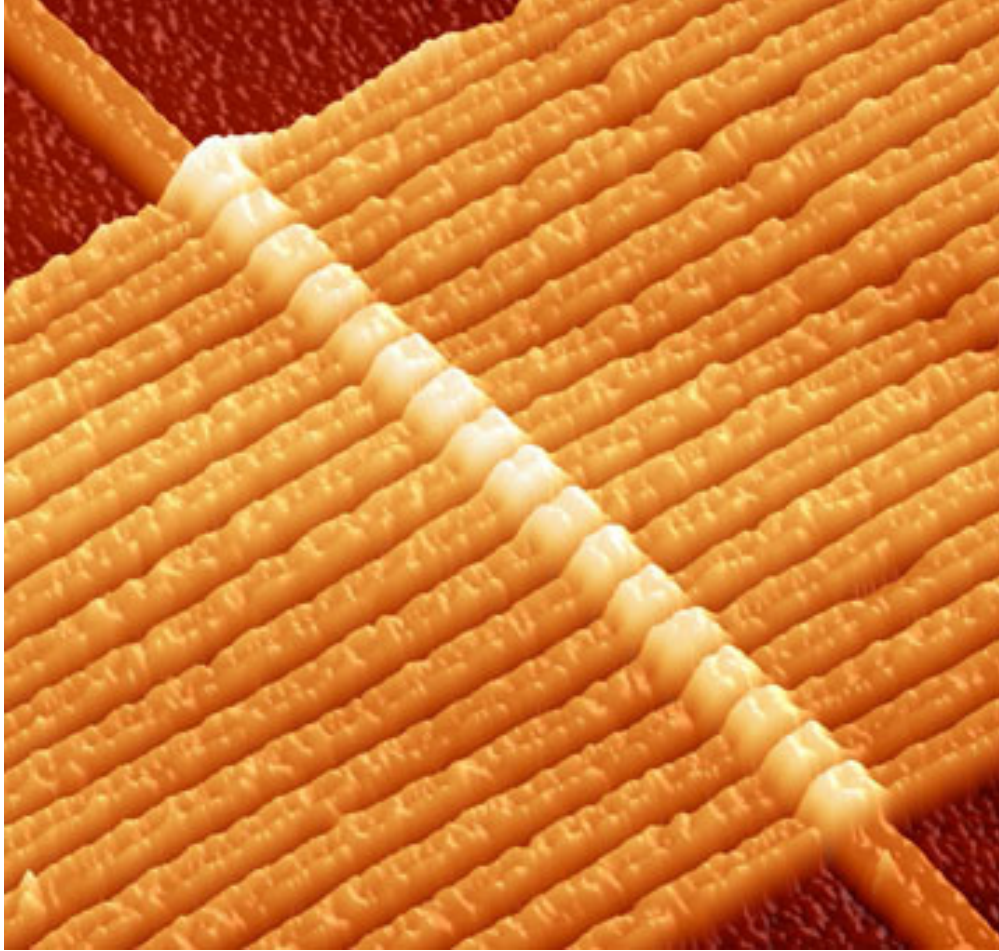
FIGURE 2.2: An image of a circuit with 17 memristors captured by an atomic force microscope. Each memristor is composed of two layers of titanium dioxide connected by wire. As electrical current is applied to one layer, the small signal resistance of the other layer is changed, which may in turn be used as a method to register data. [59]

the memristors shifts the oxygen vacancies, causing a gradual and persistent change in electrical resistance.

The major application of memristor is in computer memory. According to the report of International Technology Roadmap for Semiconductors (ITRS), it predicted that by 2019, 16 nm half-pitch Dynamic Random Access Memory (DRAM) cells will provide a capacity around 46 GB/cm$^2$, assuming 100% area efficiency. HP team

claims that memristors promise extremely high capacity more than 110 GB/cm$^2$ and 460 GB/cm$^2$ for 10 nm and 5 nm half-pitch devices, respectively. Comparing with DRAM memory, memristors can provide nonvolatile operation as provided by flash memories.

The research around memristor has been in various areas, such as memristor based on spintronic memristors, mathematical analysis of memristor system equation, memristor circuit simulation and design and memcapacitor. [18, 24, 48, 5, 65].

Let's look at some disadvantage of memristor. Since the DRAM cells must be refreshed at least every 16 ms, endurance becomes very important issue for memristor. Other major issue of memristor is switching speed. In HP cross-bar structure, the volatility-to-switching speed ratio formemristor cells is around 103. This ratio is much lower than the ratio for DRAM cells. Therefore, the switching speed of memristors is much slower the traditional DRAM. Finally, the critical issue for memristor is the readability. Finally, another advantage of RRAM is readability.

Some dynamic devices and systems, such as a thermistor, a Hodgkin-Huxley model of the nerve axon membrane, and discharge tubes, exhibit rich memristive effects and could be modeled by a group of memristive system equations. [17, 18] However, in various nanoscale physical devices, such an astonishing diversity of memristive phenomena has not been widely adopted even after almost forty years since Chua's original paper, primarily due to the absence of a straightforward linkage between a practical physical nanosystem and a mathematical model. [24, 48, 5, 65].

Since the birth of the HP memristor, a wide range of nanoscale memristive systems, including spin memeristive systems, a polymeric memristor and a resonant tunneling diode memristor have been identified and fabricated. The excitement of those memristive devices lies in expanding the electronic information processing methodology by using the state variables instead of using conventional voltage or current[65, 6, 7, 51]. For instance, digital applications associated with memris-

tors are focussed on the low power and ultra-dense programmable logic and non-volatile solid-state resistive memory, which are traditionally provided by semiconductor transistors[21, 51, 27, 67]. Beyond this, an interesting question is whether nanoscale memristive systems can go through a profound transformation and be utilized in microwave radiation fields. In the path of exploration, a passive reconfigurable frequency selective surface (FSS) using memristors for testing the roles of resistance switching in the low frequency regime has been investigated[8]. Recently, an ionic bottle memristor with low switching energy and high state retention time (switching speed ~100 ns ), and a spintronic memristor with ~10 MHz switching frequency have been reported[58, 62]. The impact of transferring such resistive switching features into the higher frequency regime may promise to be attractive for the microwave community.

## 2.2 Method

In this work, we report the first broadband radiation properties of a microstrip patch antenna modulated by dual high frequency resistive memristors. To implement a high frequency memristor model, we first consider a general first order current-controlled memristive system, which is modeled by [17]

$$
\begin{aligned}
\frac{dx(t)}{dt} &= f(x, i, t), &\text{(2.1a)}\\
v(t) &= R(x, i, t)i(t). &\text{(2.1b)}
\end{aligned}
$$

here $x, v$ and $i$ denotes the time-dependent state variable, the port voltage and the current, respectively. The functions $f$ and $R$ are explicit functions of the time $t$. For a HP memristor, based on the proposition of atomic arrangement modulating the current, the sandwich model of the semiconductor thin film device is proposed[59]. The structure of this model includes a low dopant concentration region with a high

resistance and a high dopant concentration region with a low resistance. When the external excitation $v(t)$ is applied , the internal boundary between the high region and the low region will move because of the drift of the charged dopants. Furthermore, considering the frequency response of the memristive device, the $i$-$v$ curve (Lissajous figure) will shrink to a straight line passing through the origin when we increase the applied excitation frequency. The fact is the HP memristor employs the dynamical coupling of nonlinear ionic drift and ohmic electronic conductance; hence, the system settles to the equilibrium state due to its relatively slow response to the rapid applied excitation. Several memristive-implementing mechanisms, such the interaction between magnetization dynamics and electronic charge transport, however, may hold promise to produce a faster system response[68, 64, 63]. Therefore, it is possible to generalize the memristive concept to a higher frequency band. Suppose that we have a group of normalized current-controlled memristive equations[59]

$$\frac{d\overline{w}(t)}{dt} = 4\gamma \cdot \overline{w}(t)(1 - \overline{w}(t)) \cdot i(t) \tag{2.2a}$$

$$v(t) = R_{OFF}i(t) + \overline{w}(t) \cdot (R_{ON} - R_{OFF}) \cdot i(t) \tag{2.2b}$$

where $R_{OFF}$ is the high resistance, $R_{ON}$ is the low resistance, $\overline{w}(t)$ is the normalized dopant penetration $w(t)/L$ and the window function $f(w)$ is defined by $4w(L-w)/L^2$. Our window function is four times larger than the one given in Ref. 11 in order to satisfy the normalized condition at $w = L/2$. Fig. 2.3 shows the block diagram of a nonlinear resistive memristor described in Eq. (2). The circuit diagram on right in Fig. 1 describes a variable resistor whose value is controlled by an integrator ($\int$) and a feedback ($f$). In order to implement this memristor circuit in SPICE3, Eq. (2.2a) has been rewritten in an integral form, $\overline{w}(t) = \int 4\gamma \cdot \overline{w}(t)(1-\overline{w}(t)) \cdot i(t)dt + W_0$. Here $W_0$ is the initial condition of the state variable $w(t)$, which is modeled by the voltage in SPICE3. The hard switch, dynamical properties of state variable $\overline{w}(t)$ and circuit parameter settings are illustrated in Fig. 2.4. In Fig. 2.4a, the current exhibits a
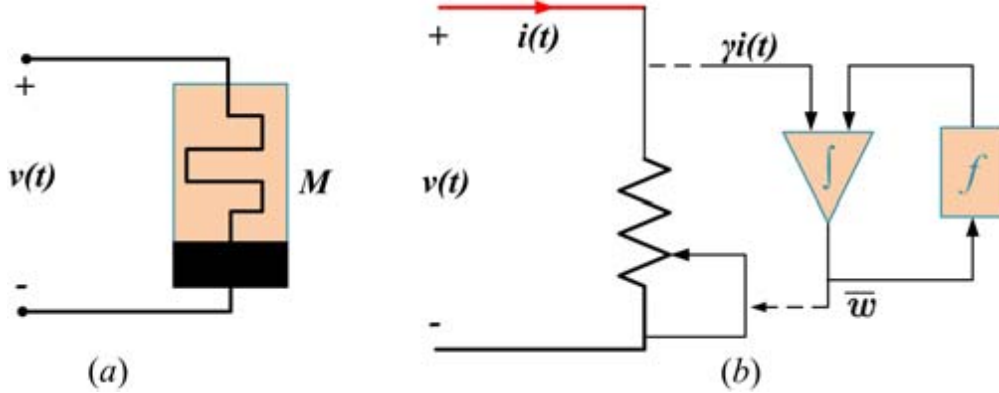
FIGURE 2.3: (a) a simplified nonlinear resistor model. $v(t)$, applied time-varying voltage; $M$, the memristance of the system. (b) Block diagram of a nonlinear resistor model. $f$ represents the circuit feedback and $\int$ means the circuit integrator. Both model the memory effect.

nonlinear dynamical relationship to the applied high frequency voltage signal $v(t)$. The periodic hysteresis I-V curve emerges with the evolution of the time-varying sinusoidal voltage excitation $v(t) = 5.5\sin(2\pi \times 10^8 t)$ V. This memristive system has the zero-crossing property in a form of Lissajous figure, which represents no current through the system when the voltage drops to zero. We also found that the applied voltage swings are large enough (relative to time) that the memristor hits its minimum resistance value (50 $\Omega$), causing spikes ($\sim 51.14 mA$) in current. Fig. 2.4b shows the dynamical property of the state variable $\overline{w}(t)$ (here modeled as a voltage in SPICE3) given the initial value of 0.6 V. The state variable periodically saturates between the normalized boundary "1" from $4.2 + 10(N - 1)$ $ns$ to $5.5 + 10(N - 1)$ $ns$, where $N$ is a natural number starting from 1.

## 2.3  Combined with Patch Antenna

In this work, we report the first broadband radiation properties of a microstrip patch antenna modulated by dual high frequency resistive memristors.

In order to explore the electromagnetic modulation characteristics of dual high frequency memristors, an L-band directly modulated microstrip patch antenna, as
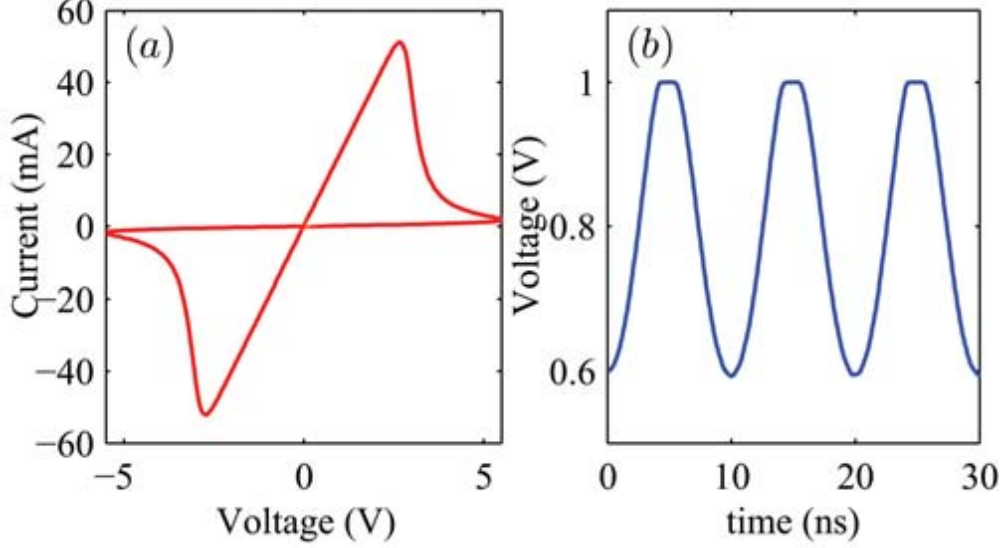
FIGURE 2.4: Simulated circuit properties of high frequency voltage-driven memristive system. (a) I-V hysteresis shape . (b) Normalized state variable curve. Hard switching occurs when $w(t)$ hits the upper boundary of 1 V. Here, applied voltage $v(t) = 5.5\sin(2\pi \times 10^8 t)$, $R_{OFF} = 15~k\Omega$, $R_{ON} = 50~\Omega$, and $\gamma = 1.2273 \times 10^{11}$.

show in Fig. 2.5a, is utilized[69, 29, 2]. The dielectric constant $\epsilon_r$ is 4.24 and permeability $\mu_r$ is 1. The area of the square patch is $47.5 \times 47.5$ mm$^2$, approximately equally to half-wavelength in the dielectrics. Fig. 2.5b shows this microstrip patch antenna resonates at 1.46 GHz with a -10 dB bandwidth of 4.8%. The probe-fed point is located at (24.3, 24.3) mm ( approximately quarter-wavelength in the dielectrics) on the top patch plane. This feeding technique allows microstrip patch antenna to transmit the orthogonal polarization radiation with a 50 $\Omega$ impedance matching. The dual high frequency memristors are placed at (23.75, -23.75) mm and (-23.75, 23.75) mm, respectively. This memristor based field-circuit model is numerically solved by a hybrid analyzing technique, which incorporates a finite-difference time-domain (FDTD) and SPICE3 solver. The whole FDTD model includes $27 \times 29 \times 18$ Yee cells. The total duration time, $T$, is 50 ns.

The electric field distributions with two different time windows are shown at 1.46 GHz in Fig. 2.6. Fig. 2.6a clearly shows the fringing field is excited at the edge of
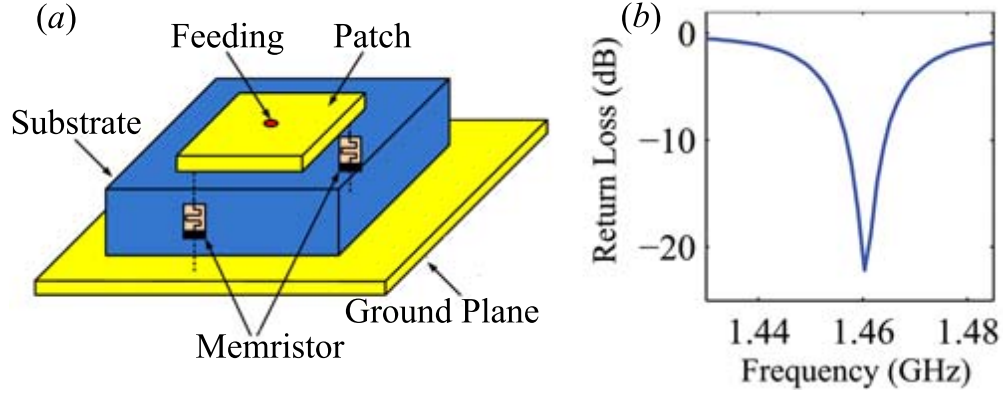
FIGURE 2.5: (a) Schematic of dual memristors embedding in a L-band directly modulated patch antenna. (b) Reflection coefficient for microwave patch antenna without the modulation.

patch. However, the fringing field is weak in Fig. 2.6b due to the low resistance of the memristor. Furthermore, Fig. 2.7a shows the time domain near-field waveform at the observer point of (0, 0, 20) mm; Fig. 2.7b shows the far field electric field waveform at (0, 0, 100) m. We can clearly observe that both received electrical field waveforms represent the amplitude modulated signal, whose amplitude is modulated by embedded nonlinear memristors. When memristors exhibits high resistance states of $14,950\ \Omega$, the microstrip patch antenna produces the EM radiation. After the 12 ns duration, the resistance of memristors drops to $50\ \Omega$, which corresponds to the "OFF" state of the antenna; hence a tiny radiation is generated. Therefore, we conclude that the narrow band microstrip patch antenna has been periodically switched "OFF" and "ON". Compared with the tradition amplitude modulation (AM) scheme, which employs the antenna's linear frequency response, the nonlinear response of this patch antenna with memristors directly switches the antenna's radiation current. Since the charging and dissipation speed of charges determine the change of the resonant current, the pulse beyond the antenna bandwidth will be radiated due to the fast nonlinear transient response.

To demonstrate the wideband radiation, Fig. 2.7c shows the spectrum of the
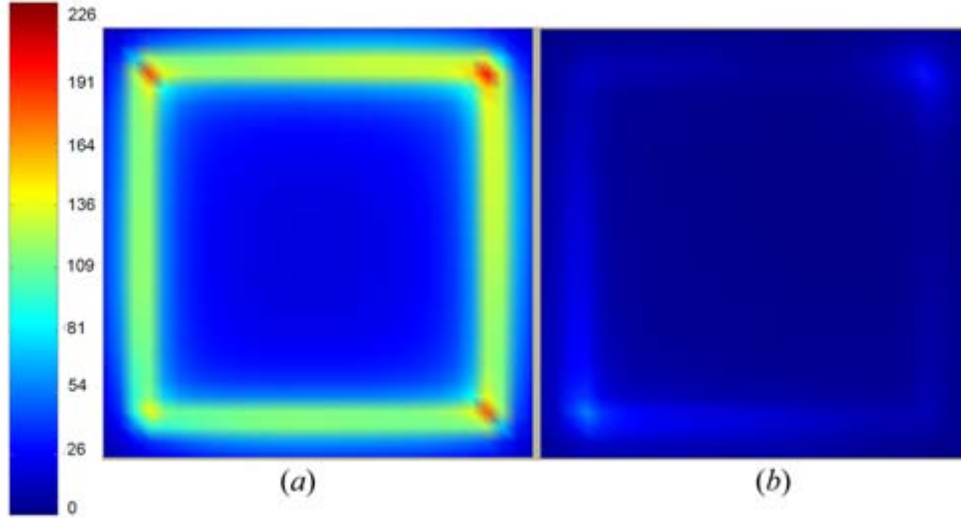
FIGURE 2.6: The electric field distribution on the microstrip patch antenna. (a) antenna is "ON" mode, switch by memristor. (b) Microstrip patch antenna is turned "OFF" by the memristor. Plotting plane location: the lower corner at (-30, -30, 3) mm and the higher corner at (30, 30, 3) mm.

modulated receiving waveform, which is computed through a fast Fourier transform algorithm. The frequencies labeled with $C$ and $T_{ij}$ stand for the carrier wave and side bands, respectively. Here the index $j$ in $T_{ij}$, of value 1 or 2, represents the lower side band or the upper side band, respectively. The index $i$, ranging from 1 to $\infty$, represents the ith tone. We observed that the first two tones, 1.35 GHz and 1.55 GHz, are suppressed to 12 dB and 13 dB with respect to the carrier signal. The other frequency components, which are beyond our microstrip patch antenna linear bandwidth, are visible. Therefore, the nonlinear response of the microstrip patch antenna produces the higher harmonics and their modulation. This bandwidth with memristors is much larger than the bandwidth with a traditional mixer[29]. Furthermore, Fig. 2.7d compares the far-field broadside radiation spectrum performance of a microstrip patch antenna modulated by diodes and one modulated by memristors. The -10 dB level bandwidth with memristors ($\sim$ 200 MHz) is twice as large as the one with diodes. However, we should notice that 100 MHz bandwidth enhancement

21

with memristors is compromised by the radiation decrease ($\sim$ 9 dB) at the central resonant frequency.

## 2.4 Summary

We first present a nonlinear transient electromagnetic radiation modulated by dual memristors. The memristor is based on the nonlinear resistor model. We use the circuit feedback and the Integrator to model the memory effect. A methodology of using a directly modulated patch antenna system with dual memristors has been developed using a hybrid circuit-field simulator. A variety of mechanisms underlying the direct modulation effects were analyzed. Broadband electromagnetic radiation has been achieved. We predict that this work on high frequency memristors will raise broad implications and stimulate pioneering work in microwave and material fields.
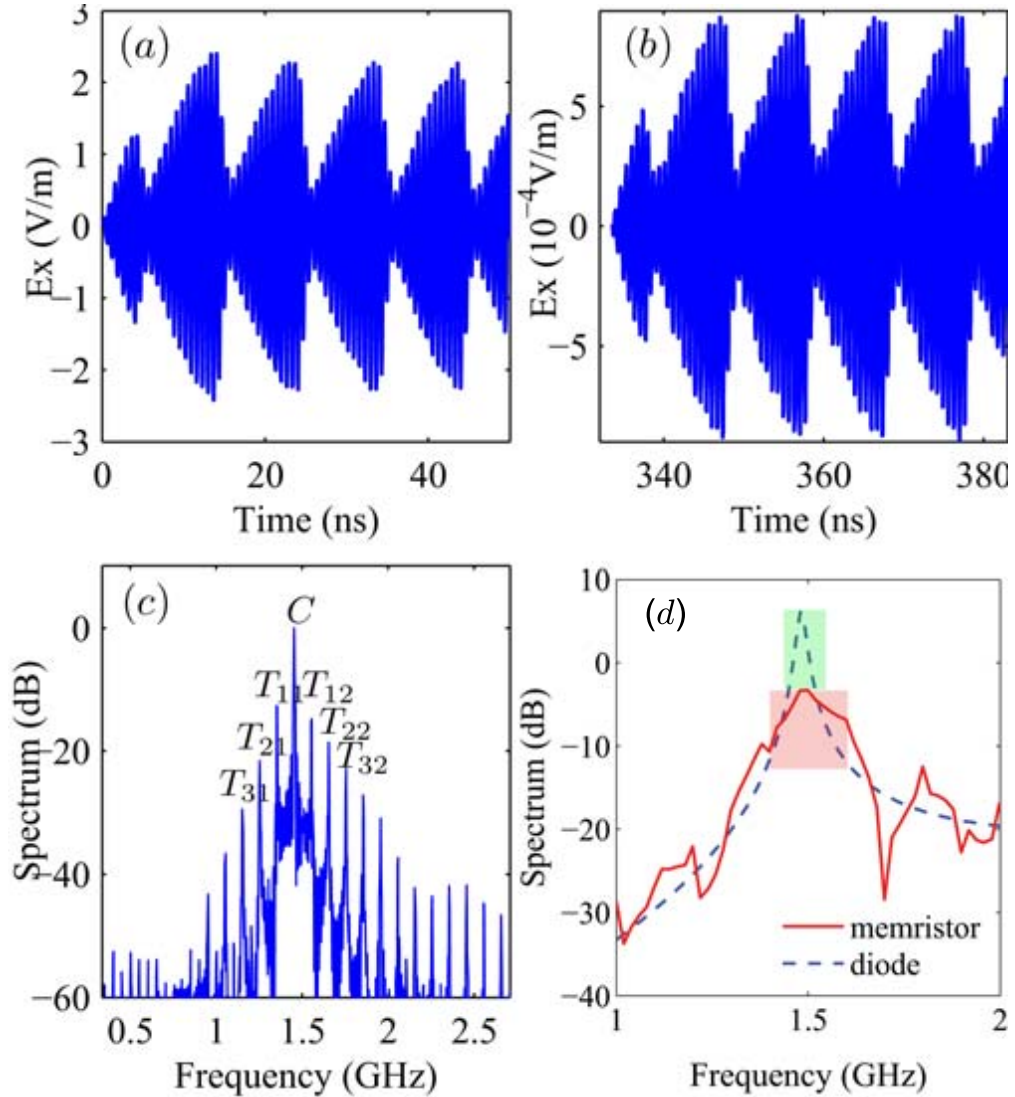
FIGURE 2.7: (Color online) (a) Received near field time-domain $E_x$ waveform at (0, 0, 20 ) mm. This electric field is a combined nonlinear response of a 1.455 GHz sinusoidal carrier wave and a 100 MHz baseband signal. (b) Received field time-domain $E_x$ waveform at (0, 0, 200) m. (c) Power spectrum of received modulation signal is normalized by it maximum value. Wideband radiation is clearly observed. (d) Far-field radiation spectrum comparisons between diodes and memristors. The -10 dB level bandwidth is used here. The -10 dB bandwidth of microstrip patch antenna (indicated by the pink box) with memristors is twice the one of microstrip patch antenna with diodes (indicated by the green box). Parameters for diodes: the saturation current, $IS = 0.1$ pA, the emission coefficient, $N = 1$, the series resistance, $RS = 0$ $\Omega$, junction capacitance, $CJO = 0$ F, transit time, $TT = 0$ sec, reverse bias breakdown voltage, $BV = 100$ V and the reverse bias breakdown current, $IBV = 0.1$ pA.

# 3

## Two-dimensional Superconducting Quantum Interference Filter in a Dynamical Electromagnetic Field Environment

The motivation of this work directly comes from how to design next-generation electromagnetic wave sensor with wider frequency band, smaller volume and also high sensitivity. For example, Guided Missile Destroyers (DDG) 1000 class ship requires such sensor system for Information perations/Signals Intelligence (IO/SIGINT) applications in Very High Frequency/Ultra High Frequency (V/UHF) bands. As shown in 3.1, because the current antennas on the radars are large in the high frequency range, the electromagnetic signature of ship is hard to be minimized into the proper size. However, employing superconducting technology, we might shrink the size of RF front, reduce radar cross-section and design a streamlined ship. Fig. 3.2 shows the envisioned Navy ship equipped by superconducting antenna technology. The other examples include that modern SATCOM communications and commercial wireless and medical systems also require high performance RF front.

We will discuss the novel magnetic antenna, which is based on superconducting quantum interference filters. We would like to start from the superconducting tech-
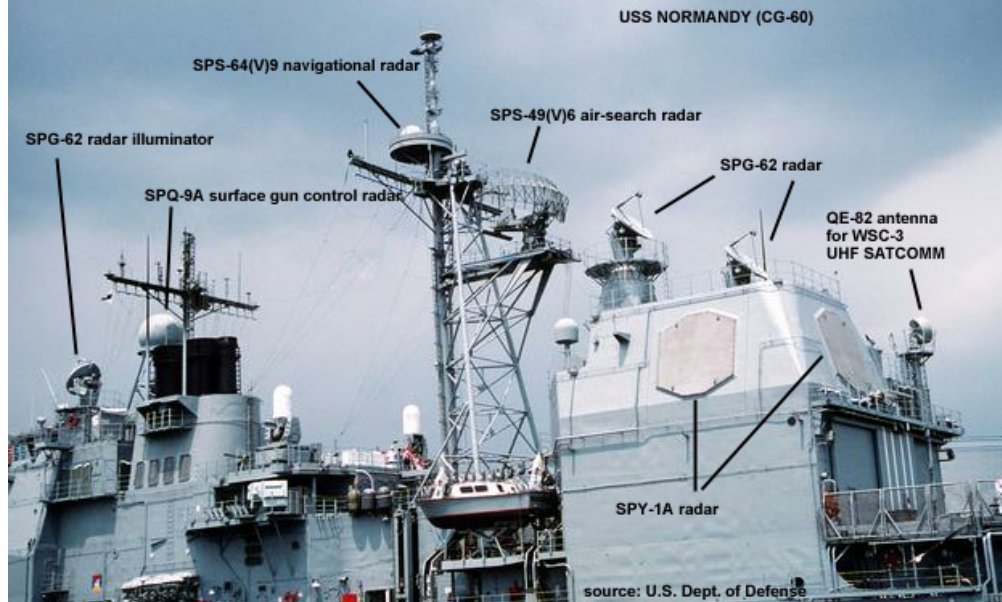
FIGURE 3.1: The current antennas installing at USS Normandy (CG-60), which is a Ticonderoga-class guided-missile cruiser in the service of the United States Navy. It includes AN/SPY-1A/B multi-function radar, AN/SPS-49 air search radar, AN/SPG-62 fire control radar, AN/SPS-73 surface search radar AN/SPQ-9 gun fire control radar.

nology, so we have a solid understanding on how does Josephson junction and its network work. Then, we march to hybrid circuit-field design and applications.

## 3.1 Macroscopic Quantum Model of Superconductivity

For better modeling and designing novel superconducting quantum interference structures, we will review key concepts and ideas starting from quantum mechanics principles. Since we are focusing on the design, modeling and simulation of superconducting quantum interference filters from the perspective of electrical engineering, our discussion focuses on applications instead of the theoretic part of quantum mechanics[36, 44].

The superconductivity is discovered by Kamerlingh Onnes in 1911. He found that a small resistance in mercury exists below a critical temperature of 4.2 K. Since then,

FIGURE 3.2: Envisioned Navy ship equipped by SQUID antenna technology. SQIF benefits to the War fighter include significant reduction in antenna signature to meet the critical goal of a DDG 1000 class ship.

there is a march for searching superconductor materials with the highest critical temperature. If we measure the transition temperature of the superconductor material, the superconductor can be classified into copper-oxide, iron-based and metallic low-temperature superconductors. Fig. 3.3 shows the transition temperature timeline.

The basic properties of a superconductor are zero resistance, Meissner effect and magnetic flux quantization and Josephson effects.

It is fascinating that superconductivity with zero resistance is a quantum phenomenon but on a macroscopic length scale. A quantum is the minimum quantity of a physical entity. Specially,the magnetic flux quantum $\Phi_0$ is the minimum quantity of magnetic flux going through a superconductor ring.

First, let us look at the *Einstein-de Broglie relations*. Einstein postulated that the electromagnetic radiation can be viewed as a collection of particles, called photons.
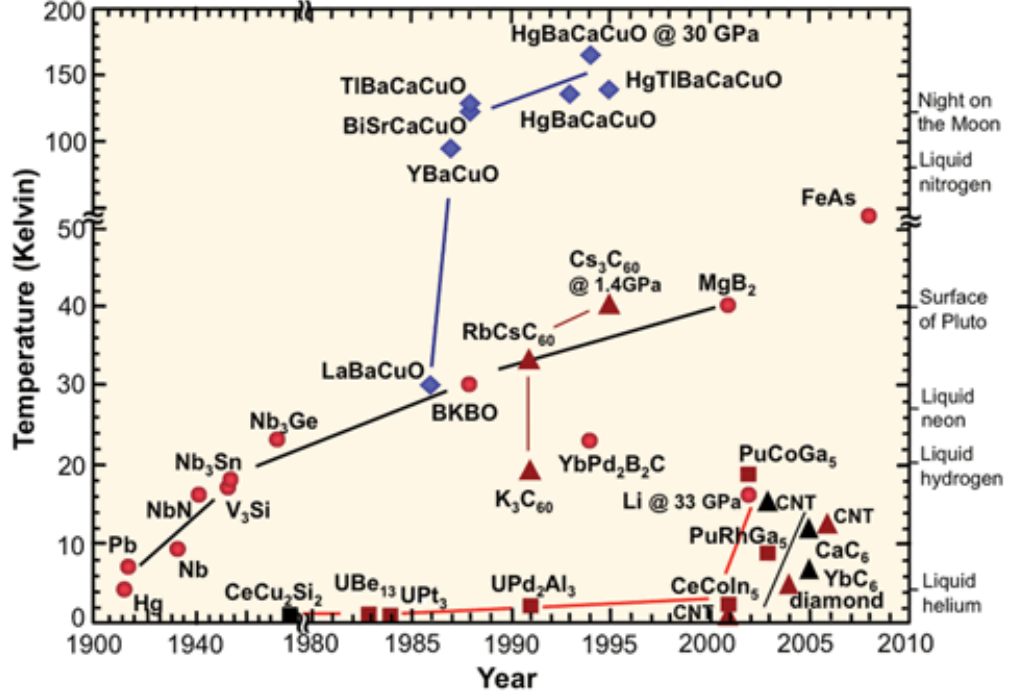
FIGURE 3.3: The transition temperature timeline of the superconductor.

He claimed that the total energy $\mathcal{E}$ is proportional to the angular frequency $\omega$ by

$$\mathcal{E} = \hbar\omega. \tag{3.1}$$

Here $\hbar$ is the reduced Planck's constant and $\hbar \equiv \frac{h}{2\pi} = 1.0546 \times 10^{-34}$ J/s.

In 1924, Louis-Victor de Broglie claimed that all matter has a wave-like behavior. The wavenumber-momentum relation is governed by

$$\boldsymbol{p} = \hbar\boldsymbol{k}. \tag{3.2}$$

Assuming that the total energy of a free particle is the kinetic energy, if we replace the velocity of the free particle by the momentum definition $\boldsymbol{p} = m\boldsymbol{v}$, the energy-momentum relation is

$$\mathcal{E} = \frac{1}{2}m(\boldsymbol{v} \cdot \boldsymbol{v}) = \frac{(\boldsymbol{p} \cdot \boldsymbol{p})}{2m}. \tag{3.3}$$

Furthermore, assuming the free particle does not encounter any external forces or potentials, we can combine above Equation 3.1 and Equation 3.3 into one equation, we obtain the dispersion relation of a free particle:

$$\hbar\boldsymbol{\omega} = \frac{\hbar^2}{2m}(\boldsymbol{k} \cdot \boldsymbol{k}). \tag{3.4}$$

We notice that the free particle is expressing in the wavevector space and frequency $(\boldsymbol{k}, \omega)$.

Assuming that the quantum particle is the superposition of all matter waves, we find that the complex wave function $\psi = \hat{\psi}e^{i(\boldsymbol{k}\cdot\boldsymbol{r}-\omega t)}$ satisfies the dispersion relation. However, the dynamic behavior of a general particle is governed by Schrödinger's equation

$$i\hbar\frac{\partial\psi}{\partial t} = -\frac{\hbar^2}{2m}\nabla^2\psi + V(\boldsymbol{r})\psi. \tag{3.5}$$

Here $V(\boldsymbol{r})\psi$ is the potential energy of the quantum system.

The probability $\mathcal{P}$ of single particle found at position of $\boldsymbol{r}$ and at time $t$ is given by the square of magnitude of the complex wave function:

$$\mathcal{P}(\boldsymbol{r},t) = |\psi(\boldsymbol{r},t)|^2 = \psi^*(\boldsymbol{r},t)\psi(\boldsymbol{r},t) \tag{3.6}$$

$$\tag{3.7}$$

Here, $\int \psi^*(\boldsymbol{r},t)\psi(\boldsymbol{r},t)d\boldsymbol{r} = 1$.

We define that the probability current $\boldsymbol{J}_\mathcal{P}$ of a charged quantum particle in an electromagnetic field

$$\boldsymbol{J}_\mathcal{P} = \Re\{\psi^*(\frac{\hbar}{im}\nabla - \frac{q}{m}\boldsymbol{A})\psi\}. \tag{3.8}$$

We can obtain the similar current expression for the macroscopic wave function $\Psi$. We define the density of supereletrons $\Psi^*(\boldsymbol{r},t)\Psi(\boldsymbol{r},t) = n^*$ and the total number of supereletrons $N^* = \int d\boldsymbol{r}\Psi^*(\boldsymbol{r},t)\Psi(\boldsymbol{r},t)$. The physical current density of the

28

supereletrons is given by

$$\boldsymbol{J}_{\mathcal{S}} \quad = \quad q^\star \Re\{\Psi^*(\frac{\hbar}{im^\star}\nabla - \frac{q^\star}{m^\star}\boldsymbol{A})\Psi\}. \tag{3.9}$$

Let the macroscopic wave function $\Psi(\boldsymbol{r},t) = \sqrt{n^\star}e^{i\theta(\boldsymbol{r},t)}$, this supercurrent can be expressed as

$$\boldsymbol{J}_{\mathcal{S}} \quad = \quad q^\star n^\star(\frac{\hbar}{im^\star}\nabla\theta(\boldsymbol{r},t) - \frac{q^\star}{m^\star}\boldsymbol{A}(\boldsymbol{r},t)) \tag{3.10}$$

If the density $n^\star(\boldsymbol{r},t)$ is independent with the space and time, then we can find the energy-phase relationship

$$-\hbar\frac{\partial\theta}{\partial t} \quad = \quad \frac{1}{2n^\star} \wedge J_S^2 + q^\star\phi. \tag{3.11}$$

Here, the London coefficient $\wedge$ is $\wedge = \mu_0\lambda^2 = \frac{m^\star}{n^\star(q^\star)^2}$, which is related to the penetration depth. The right hand side of Equation 3.11 represents the energy of a superelectron. If we take the time derivative of the supercurrent equation:

$$\frac{\partial(\wedge J_S)}{\partial t} \quad = \quad -[\frac{\partial\boldsymbol{A}}{\partial t} - \frac{\hbar}{q^\star}\nabla(\frac{\partial\theta}{\partial t})]. \tag{3.12}$$

We can get *the first London's equation*. It explains the perfect conductivity by

$$\frac{\partial(\wedge J_S)}{\partial t} \quad = \quad \boldsymbol{E} - \frac{1}{n^\star q^\star}\nabla(\frac{1}{2} \wedge J_S^2). \tag{3.13}$$

The supercurrent in a superconductor is a function of magnetic vector potential $\boldsymbol{A}$ and the phase $\theta$. The localized supercurrent can be expressed as

$$\wedge\boldsymbol{J}_s \quad = \quad \frac{\hbar}{q^\star}\nabla\theta - \boldsymbol{A}. \tag{3.14}$$

With the basic localized supercurrent expression, we would like to look at the summation expression of localized supercurrent along an oriented path $L$. The integral form along the certain path will give us a real number which provides certain

29

insight in a bigger picture. So, let's see what will happen if the integral path $L$ is chosen with a closed contour $C$.

$$\oint_C (\wedge \boldsymbol{J}_S) \cdot d\boldsymbol{l} + \oint_C \boldsymbol{A} \cdot d\boldsymbol{l} = \frac{\hbar}{q^\star} \oint_C \nabla \theta \cdot d\boldsymbol{l}. \tag{3.15}$$

First, let us look at the second term of Equation. 3.15. This term is very interesting. It states the contour integral of the magnetic vector potential $\boldsymbol{A}$. According to the Stokes's theorem,

$$\oint_C \boldsymbol{A} \cdot d\boldsymbol{l} = \int_S (\nabla \times \boldsymbol{A}) \cdot d\boldsymbol{s} = \int_S \boldsymbol{B} \cdot d\boldsymbol{s}. \tag{3.16}$$

It says that the contour integral of a magnetic vector potential is replaced by the area integral of the corresponding magnetic field. Now the supercurrent equation 3.15 can be written as

$$\oint_C (\wedge \boldsymbol{J}_S) \cdot d\boldsymbol{l} + \int_S \boldsymbol{B} \cdot d\boldsymbol{s} = \frac{\hbar}{q^\star} \oint_C \nabla \theta \cdot d\boldsymbol{l}. \tag{3.17}$$

Through the process of magnetic flux quantization, we get

$$\oint_C (\wedge \boldsymbol{J}_S) \cdot d\boldsymbol{l} + \int_S \boldsymbol{B} \cdot d\boldsymbol{s} = n\Phi_0. \tag{3.18}$$

The left side is called fluxiod and the flux quantum is defined as $\Phi_0 \equiv \frac{2\pi\hbar}{|q^\star|} = \frac{h}{|-2e|} = 2.07 \times 10^{-15}$ T-m$^2$. $n$ can be any integer for multiple connected region.

## 3.2  Basic Josephson Junction Model ($I < I_C$)

From the framework of macroscopic quantum theory of the superconductor, we note that the supercurrents are induced by electric and magnetic fields. However, the suppercurrent can be produced by the phase difference through a process of electron tunnelling.
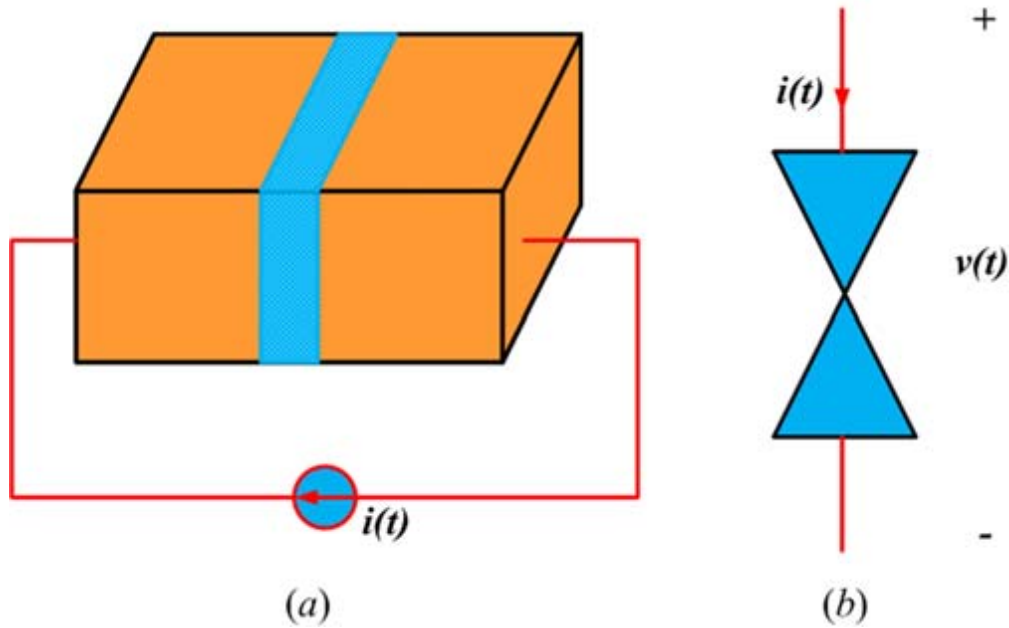
FIGURE 3.4: (a) A Josephson junction driving by a current source $i(t)$. The yellow part indicates the superconductor. The blue part denotes the insulator layer. (b) a simplified lumped model of a Josephson junction, which considers an uniform distribution of gauge invariant phase difference and an uniform current density.

Two kinds of electron tunnelings have been discovered in superconductors: a normal electron tunneling with an applied voltage of $\frac{2\Delta}{e}$ and a cooper pair tunneling with zero applied voltage. Fig. 3.4 shows a sandwich structure of a Josephson junction. This junction is the superconductor-insulator-superconductor (SIS) structure. The insulator is very thin with a thickness of about 10 Å. Due to the existence of the Cooper pairs, the minimum voltage for breaking the Cooper pairs to produce a current is $2\Delta/e$. Josephson reasons that the Cooper pairs could tunnel through barriers like single electron does. In other words, it is the macroscopic wavefunction that tunnels from one superconductor to the other.

The Cooper pairs can only carry a limited current. Otherwise, the Josephson effect will be disappear. The maximum current density passing though the junction at zero voltage is called the *Josephson critical current density* $J_C$. The critical current

density $J_C$ is an important phenomenological parameter of the junction device that can be affected by the temperature as well as an applied magnetic field $\boldsymbol{B}$. When the applied DC current density exceeds the critical current density $J_C$, a voltage drop $\Delta V$ will be produced.

We are not diving into the details of how we arrive to the formulation of a Josephson junction. However, the the fundamental circuit law governing the Josephson junction is summarized by the Josephson *current-phase difference* equation and the Josephson *voltage-phase difference* equation. First, let us look at the relation of Josephson *current-phase difference*

$$\boldsymbol{J}_s(\boldsymbol{r},t) \quad = \quad \boldsymbol{J}_c(\boldsymbol{r},t)\sin\varphi(\boldsymbol{r},t). \tag{3.19}$$

Here the guage-invariant phase difference $\varphi$ is defined by

$$\varphi(\boldsymbol{r},t) \quad = \quad \theta_1(\boldsymbol{r},t) - \theta_2(\boldsymbol{r},t) - \frac{2\pi}{\Phi_0}\int_1^2 A(\boldsymbol{r},t)\cdot d\boldsymbol{l}. \tag{3.20}$$

From above equation, we find that the guage-invariant phase difference is contributed from two different physical parts. The first part is general phase difference $\theta_1 - \theta_2$ of wave functions at two ends of the Josephson junction. The other part is from the line integral of magnetic vector potential $\boldsymbol{A}$. Apparently, magnetic vector potential $\boldsymbol{A}$ modifies the values of gauge-invariant phase difference $\varphi$ along different paths.

On the other hand, the relation of Josephson voltage-phase difference is given by

$$\frac{\partial\varphi(\boldsymbol{r},t)}{\partial t} \quad = \quad \frac{2\pi}{\Phi_0}\int_1^2 \boldsymbol{E}(\boldsymbol{r},t)\cdot d\boldsymbol{l}. \tag{3.21}$$

For a lumped Josephson junction, the localized Equation 3.20 and 3.21 can be
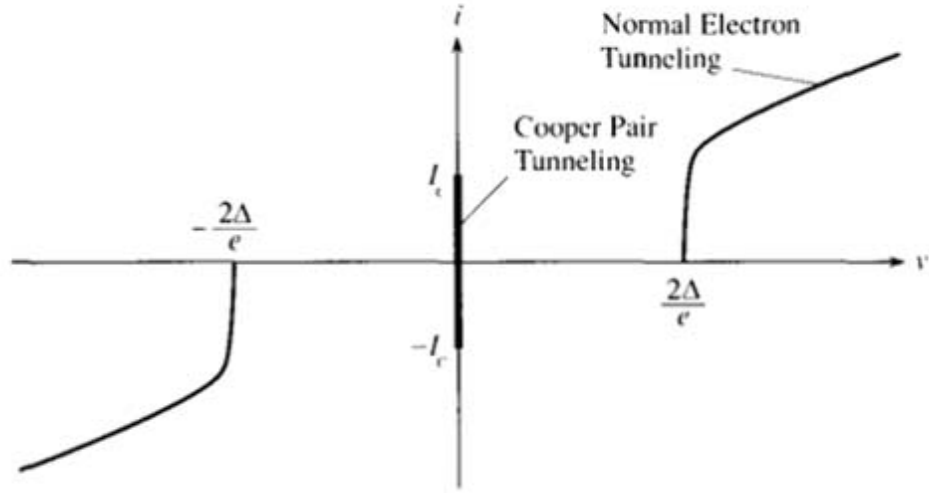
FIGURE 3.5: The i-v curve for a Josephson junction. The current at zero voltage is called the Josephson current induced by the Cooper pair tunneling. This current represents the range of current following through the Josephson junction.

written in terms of the voltage and the current.

$$i(t) = I_c \sin \varphi(t) \tag{3.22}$$

$$v(t) = \frac{\Phi_0}{2\pi} \dot{\varphi}(t) \tag{3.23}$$

$$\varphi(t) = \theta_1 - \theta_2 - \frac{2\pi}{\Phi_0} \int_1^2 \boldsymbol{A}(\boldsymbol{r}, t) \cdot d\boldsymbol{l}. \tag{3.24}$$

The typical value of $I_c$ is about 1 mA.

It is convenient for circuit simulation that Equation 3.22 and 3.23 can be transformed into a single equation by eliminating the gauge-invariant phase difference $\varphi(t)$,

$$i(t) = I_c \sin(\varphi_0 + \frac{2\pi}{\Phi_0} \int v(t) dt). \tag{3.25}$$

Now, we can discuss the dynamic behavior of the junction with different driven sources. The first interesting thing is that if we apply a small DC voltage($< 2\Delta/e$)

across the Josephson junction will, the Cooper pairs will oscillate and generate a very small RF radiation which can be detected by the EM sensor. This phenomena is called *ac Josephson effect*. For example, if $v(t) = V_0$, then

$$\varphi(t) \;=\; \varphi(0) + \frac{2\pi}{\Phi_0} V_0 t. \tag{3.26}$$

The Josephson frequency is $f_J = \frac{V_0}{\Phi_0} = 483.6 \times 10^{12} V_0$ Hz. Therefore, a DC voltage of 10 $\mu$V can generate an oscillation frequency of 5 GHz.

When the junction is supplied by a hybrid AC and DC source, the induced current $i(t)$ is

$$i(t) \;=\; I_c \sin(\varphi(0) + \frac{2\pi V_0}{\Phi_0} t + \frac{2\pi v_s}{\Phi_0 \omega_s} \sin \omega_s t). \tag{3.27}$$

In this equation, the gauge invariant phase is modulated by the linear term and a nonlinear sinusoidal term. By using the Fourier-Bessel series to express the current, we get

$$i(t) \;=\; I_c \sum_{n=-\infty}^{\infty} (-1)^n [J_n(\frac{2\pi v_s}{\Phi_0 \omega_s})] \sin[(2\pi f_J - n\omega_S)t + \varphi(0)] \tag{3.28}$$

If the DC voltage and the applied AC voltage frequency meet the linear relationship of $2\pi f_J = n\omega_S$ or $V_0 = n\Phi_0 f_S$, the current $i(t)$ will be invariable and independent with the time $t$.

## 3.3 Resistively Shunted Junction (RSJ) Model $(I > I_C)$

Let us consider a normal electron tunneling channel model. The electron tunneling can be modeled by the normal resistance $R_J$. When we connect an external current

source $i(t)$, we had the following current relationship:

$$i(t) = i_S(t) + i_N(t) \tag{3.29}$$

$$= i_S(t) + \frac{v(t)}{R_J} \tag{3.30}$$

$$= I_C \sin \varphi(t) + \frac{\Phi_0}{2\pi R_N} \dot{\varphi}(t) \tag{3.31}$$

Considering two cases. First, when the driving direct current $I$ is smaller than the critical current $I_C$, all current flows into the junction at zero voltage. Therefore, we have a constant phase expression as following

$$\varphi = \sin^{-1} \frac{i}{I_C} \tag{3.32}$$

When $I > I_C$, the partial current enters the Josephson junction and the other $i_N(t)$ enters the resistance channel. This resistance will produces the voltage across the junction which cause the time-changed phase $\varphi$

$$\varphi(t) = 2\tan^{-1}[\sqrt{1 - (\frac{I_C}{i})^2} \tan(\frac{t\sqrt{(i/I_C)^2 - 1}}{2\tau_J}) + \frac{I_C}{i}]. \tag{3.33}$$

Here $\tau_J = \frac{\Phi_0}{2\pi I_C R}$. We can see the phase has a period

$$T = \tan(\frac{2\pi\tau_J}{\sqrt{(i/I_C)^2 - 1}}) \tag{3.34}$$

If $i \gg I_C$, the above equation gives $\varphi(t) = \frac{2\pi}{\Phi_0} iRt$. That means both current and voltage will vary sinusoidally.

## 3.4 Superconductor quantum interference devices(SQUIDs)

Macroscopic quantum interference in superconductors is a spectacular physical phenomenon that the supercurrent $i_s$ flowing through the Josephson junction without the external voltage source.
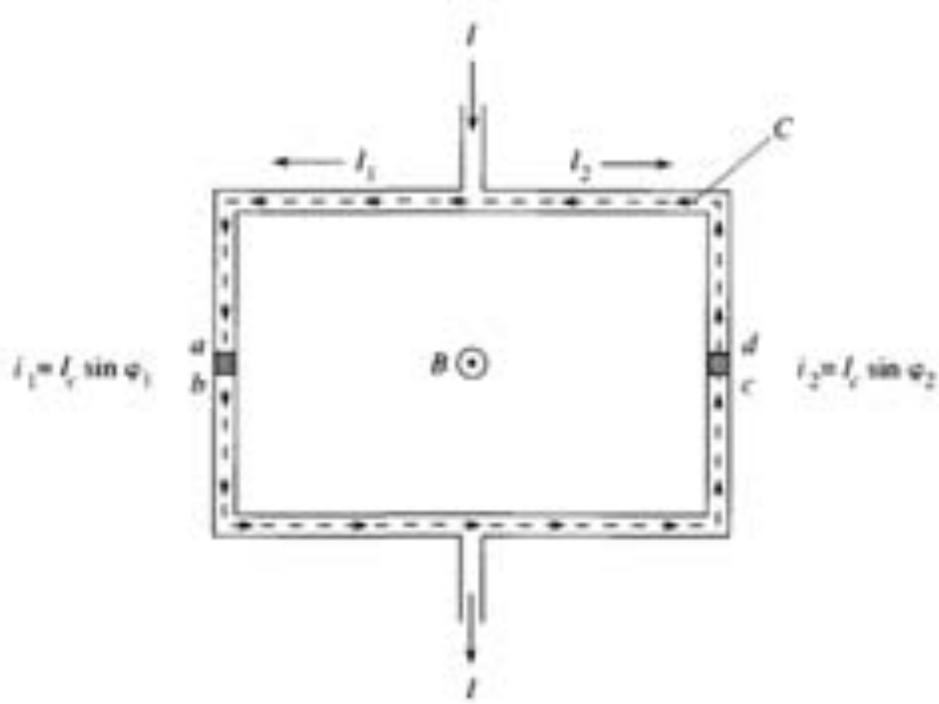
FIGURE 3.6: The configuration of SQUID.

Now let us look at macroscopic quantum interference in a system of two junctions, called superconducting quantum interference device (SQUID). So, what is SQUID? A SQUID is a sandwich structure that consists of two parallel Josephson junctions connected by superconducting wires.

The maximum Josephson current in this structure can be modulated by the external magnetic field. It has the application on the sensitive magnetic field sensor.

We would associate a vector $\boldsymbol{B}(x, y, z, t)$ as magnetic field. In science and measurement fields, the unit of magnetic field $\boldsymbol{B}$ is often chose as one tesla in SI units. It is interesting that the Tesla is a very big unit, so scientists trend to use Nanotesla,

$$1 \text{ Tesla} = 10^9 \text{ Nanotesla.} \tag{3.35}$$

Table 3.4 gives typical orders of magnetic field $\boldsymbol{B}$ magnitude.

In engineering fields, engineers often use magnetic field intensity $\boldsymbol{H}$ in stead of

36

Table 3.1: *Orders of magnetic field **B** magnitude.*

| Value | SI prefix | Example |
|---|---|---|
| $10^{-15}$ | femtoteslas | SQUID magnetometers on Gravity Probe B gyros in one second |
| $10^{-12}$ | picoteslas | Human brain magnetic field |
| $10^{-11}$ | | the natural magnetic field at 60 Hz |
| $10^{-5}$ | | Earth's magnetic field |
| $10^{-3}$ | milliteslas | The suggested exposure limit for cardiac pacemakers |
| $10^{0}$ | teslas | MRI system |
| $10^{3}$ | kiloteslas | Strongest (pulsed) magnetic field ever obtained in a laboratory |

**B**. The unit of magnetic field intensity $H$ is one ampere per meter in SI units. The relationship between **H** and **B** is simple in air:

$$\boldsymbol{B} = \mu_0 \boldsymbol{H} \tag{3.36}$$

$$= 4\pi \times 10^{-7} \boldsymbol{H}. \tag{3.37}$$

Assuming that we are considering a SQIF placing in a static magnetic field environment, the SQIF loop occupies an area of $50 \times 50 \ \mu m^2$ and the SQIF has detected 0.1 magnetic flux quantum. How large the magnetic field is?

The simple linear relation between magnetic flux and magnetic field **B** gives us

$$\Phi = \boldsymbol{B} \times S \tag{3.38}$$

$$= \mu_0 \boldsymbol{H} \times S. \tag{3.39}$$

We can get the magnetic field intensity $H$ is

$$H = \frac{\Phi}{\mu_0 \times S} \tag{3.40}$$

$$= \frac{0.1 \times 2.067 \times 10^{-12}}{4\pi \times 10^{-7} \times 50 \times 50 \times 10^{-12}} \tag{3.41}$$

$$= 0.0658 \ \text{A/m}. \tag{3.42}$$

This value gives us the sense how large do our SQUIDs deal with magnetic fields.
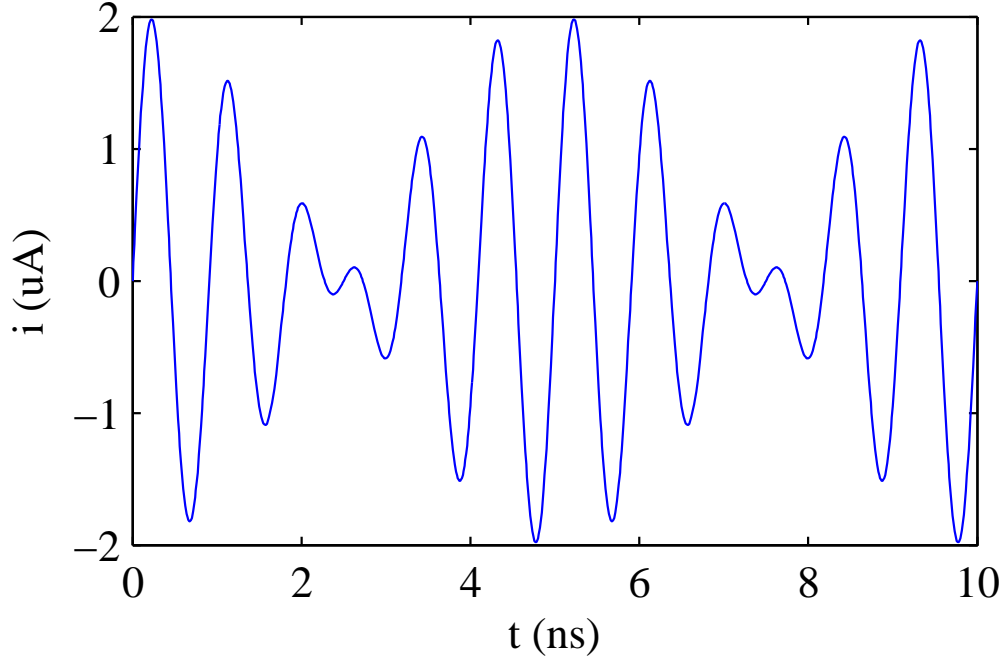
FIGURE 3.7: The superconducting quantum interference pattern with $\varphi_1 = 2\pi \times 1 \times 10^9\ t$ and $\varphi_2 = 2\pi \times 1.2 \times 10^9 t$.

A vector field can lead to an interesting quantity, called flux. Flux is the normal component of a vector field times the area of the surface. For example, magnetic flux $\Phi$ is

$$\Phi = \int \boldsymbol{B} \times d\boldsymbol{s}. \tag{3.43}$$

If we had two Josephson currents $i_1(t)$ and $i_2(t)$, the sum of two currents $i(t)$ will be

$$
\begin{aligned}
i(t) &= i_1(t) + i_2(t) & \text{(3.44)} \\
&= I_C \sin \varphi_1 + I_C \sin \varphi_2 & \text{(3.45)} \\
&= 2I_C \cos(\frac{\varphi_1 - \varphi_2}{2}) \sin(\frac{\varphi_1 + \varphi_2}{2}). & \text{(3.46)}
\end{aligned}
$$

Fig. 3.7 gives the interference pattern with two different phases.

38

Since the phase is given by

$$\oint_C \nabla\theta \cdot dl = \lim_{\mathbf{r}_b \to \mathbf{r}_a} (\theta(\mathbf{r}_a, t) - \theta(\mathbf{r}_b, t))2\pi n \tag{3.47}$$

$$= (\theta_b - \theta_a) + (\theta_c - \theta_b) + (\theta_d - \theta_c) + (\theta_a - \theta_d). \tag{3.48}$$

Supercurrent equation gives the gauge invariant phase difference

$$\varphi_2 - \varphi_1 = 2\pi n + \frac{2\pi}{\Phi_0} \oint_C A(\mathbf{r}, t) \cdot dl + \wedge \int_b^c \mathbf{J} \cdot dl + \wedge \int_d^a \mathbf{J} \cdot dl. \tag{3.49}$$

The current integral can be equal to zero if we choose the proper contour $path_{ac}$ and $path_{da}$. Therefore, the phase difference is reduced to

$$\varphi_2 - \varphi_1 = 2\pi n + \frac{2\pi\Phi}{\Phi_0}. \tag{3.50}$$

The total interference current will be

$$i(t) = i_1(t) + i_2(t) \tag{3.51}$$

$$= I_C \sin\varphi_1 + I_C \sin\varphi_2 \tag{3.52}$$

$$= 2I_C \cos(\frac{\pi\Phi}{\Phi_0}) \sin(\varphi_1 + \frac{\pi\Phi}{\Phi_0}). \tag{3.53}$$

The flux in the contour includes the external flux and the flux induced by the circulating current

$$\Phi = \Phi_{ext} + Li_{cir} \tag{3.54}$$

$$= \Phi_{ext} + \frac{LI_C}{2} \sin(\frac{\pi\Phi}{\Phi_0}) \cos(\varphi_1 + \frac{\pi\Phi}{\Phi_0}). \tag{3.55}$$

Here $i_{cir} = (i_1 - i_2)/2$.

If there is no self-inductance $L$, then $\Phi = \Phi_{ext}$. Therefore, the superconducting current will be

$$i(t) = 2I_C \cos(\frac{\pi\Phi_{ext}}{\Phi_0}) \sin(\varphi_1 + \frac{\pi\Phi_{ext}}{\Phi_0}) \tag{3.56}$$

39
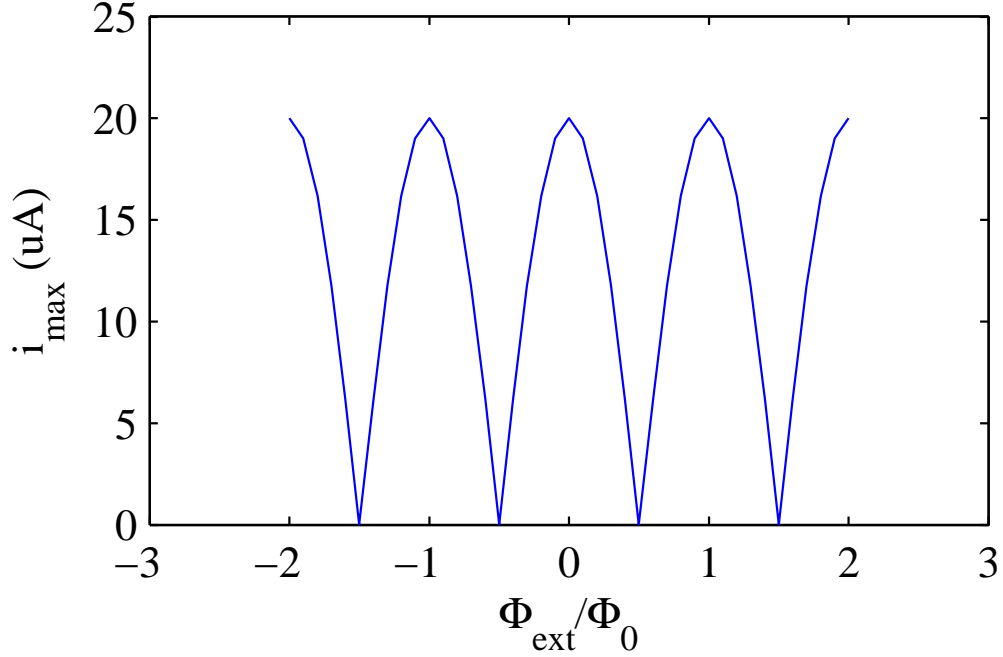
FIGURE 3.8: The maximum superconducting current as a function of normalized external magnetic flux $\Phi_{ext}/\Phi_0$

.

The extremal condition of $i_{max}$ will give the derivatives of $i(t)$ with respect of $\varphi_1$. The the maximum superconducting current will be a function of the external flux

$$i(t)_{max} \quad = \quad 2I_C|\cos(\frac{\pi\Phi_{ext}}{\Phi_0})| \tag{3.57}$$

The period of achieving the maximum current is 1 or the external flux satisfies the condition of $\Phi_{ext} = n\phi_0$. Fig. 3.8 shows the $i_{max}$ distribution with different external magnetic flux with the absence of self-inductance. For the situation of SQUID with an inductance, we define the normalized inductance rate is $\beta_L = 2\pi L I_C/\phi_0 = L/L_J$.

The generalized Josephson junction includes a basic Josephson junction, a resistive channel and a capacitive channel. According to the microscopic quantum mechanics explanation, the resistance $R$ of the Josephson junction is due to the normal electrons tunneling, which is formed by the breaking of the Cooper pairs into
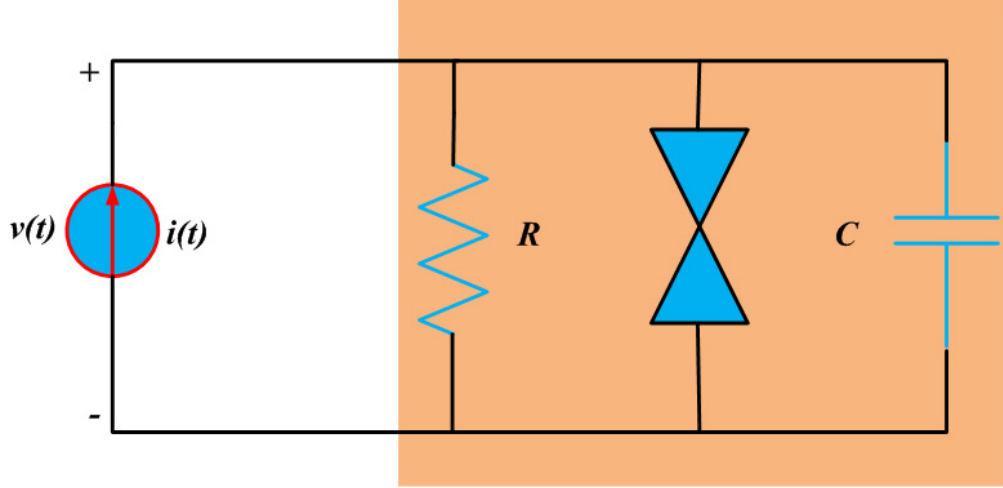
FIGURE 3.9: The equivalent circuit model of generalized Josephson junction model with parallel capacitance $C$ and resistance $R$. $i(t)$ is applied current source.

normal electrons. On the other hand, the junction capacitance $C$ is formed by the classic parallel structure of the junction. An electrical engineer, who are focusing on the relation of voltage and the current, is interested in this device as building elements of the circuit, especially for the specular current-voltage relation of this generalized Josephson junction model with the existence of either DC, AC sources or magnetic fields.

Fig. 3.9 gives the resistively and capacitively shunted junction $RCSJ$ model. In this model, the resistance $R$ is simplified and independent of the junction voltage. Based on Kirchhoff's current law, the circuit can be described by

$$i(t) = I_c \sin \varphi + \frac{v(t)}{R} + C\frac{v(t)}{dt}. \tag{3.58}$$

. Here, the left hand side $i(t)$ in Equation 3.58 gives a DC driving current across the generalized Josephson junction. The first term $I_c \sin \varphi$ in the right hand side represents the Josephson junction current, the second term $\frac{v(t)}{R}$ represents the current though the normal resistance channel $R$. The last term $C\frac{v(t)}{dt}$ gives the capacitive channel.

41

Substituting the phase-voltage relationship into Equation 3.58 results in a second order nonlinear differential equation for the phase difference $\varphi$:

$$C\frac{\Phi_0}{2\pi}\frac{d^2\varphi}{dt^2} + \frac{1}{R}\frac{\Phi_0}{2\pi}\frac{d\varphi}{dt} + I_c\sin\varphi \;=\; i(t). \tag{3.59}$$

Here $\sin\varphi$ is the nonlinear term and can be solved numerically. If the whole equation is normalized by the critical current $I_C$, then Equation 3.59 becomes

$$\beta_C\frac{d^2\varphi}{d\tau^2} + \frac{d\varphi}{d\tau} + \sin\varphi \;=\; i(t)/I_C. \tag{3.60}$$

Here $\beta_C = \frac{RC}{\tau_J} = \frac{\tau_R C}{\tau_J}$ and called *stewart-McCumber* parameter. $\tau_J = \frac{\Phi_0}{2\pi}\frac{1}{I_c R}$ and $\tau = \frac{t}{\tau_J}$. Fig. 3.10 gives the numerical solution of Josephson junction $V - I$ relationship with the DC source. The $ODE45$ solver is used to solve this equation.

For the case of $\beta_C \ll 1$, we can neglect the effect of the shunt capacitance $C$. The Kirchoff's current law gives

$$\frac{i}{I_C} \;=\; \sin(\varphi) + \frac{d\varphi}{d\tau}. \tag{3.61}$$

Solving this first order differential equation produces

$$\varphi(t) \;=\; 2\tan^{-1}[\sqrt{1 - (\frac{I_C}{i})^2}\tan(\frac{t\sqrt{(i/I_C)^2 - 1}}{2\tau_J}) + \frac{I_C}{i}]. \tag{3.62}$$

From the term of $\tan(\frac{t\sqrt{(i/I_C)^2-1}}{2\tau_J})$, we obtained the period of the phase :

$$\Theta \;=\; \frac{2\tau_J\pi}{\sqrt{(i/I_C)^2 - 1}} \tag{3.63}$$

42
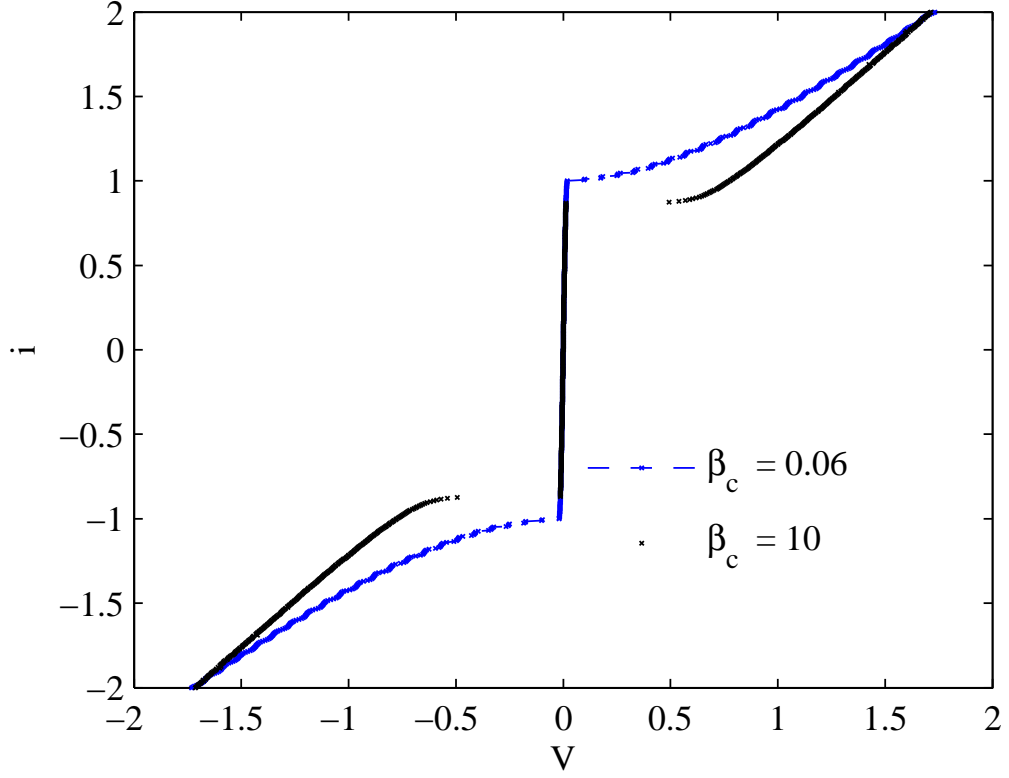
FIGURE 3.10: The numerical solution of Josephson junction $V - I$ relationship with the DC source. $i \in [-2, 2]$

The time average voltage $< v(t) >$ over one period is defined by

$$< v(t) > \quad = \quad \frac{1}{\Theta} \int_0^\Theta v(t)dt \qquad (3.64)$$

$$= \quad \frac{1}{\Theta} \int_0^\Theta \frac{\Phi_0}{2\pi} \frac{d\varphi}{dt} dt \qquad (3.65)$$

$$= \quad \frac{1}{\Theta} \frac{\Phi_0}{2\pi} [\varphi(\Theta) - \varphi(0)]. \qquad (3.66)$$

Since the phase difference over one period is $2\pi$, the average voltage $< v(t) >$ becomes
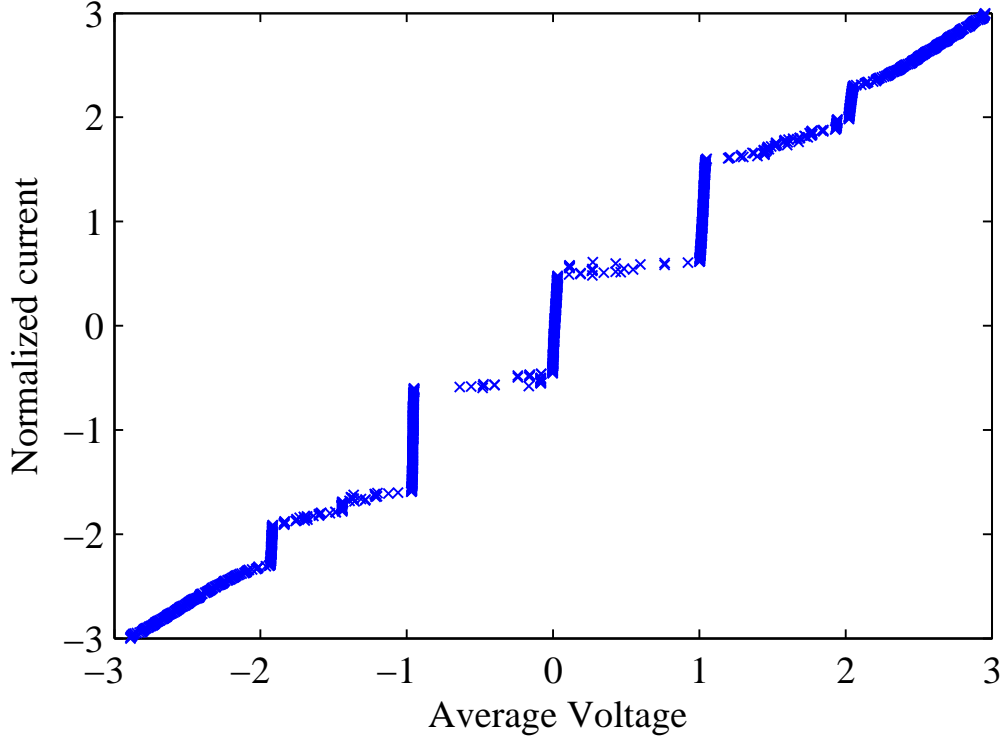
FIGURE 3.11:   The numerical solution of Josephson junction $V - I$ relationship with the AC source. $\beta = 1$, $i_a = 2$ and $w = 1$

$\frac{\Phi_0}{\Theta}$. With the definition of the period $\Theta$, the average voltage is

$$< v(t) > \quad = \quad iR\sqrt{1 - (\frac{I_C}{i})} \tag{3.67}$$

$$= \quad R\sqrt{i^2 - I_C^2}. \tag{3.68}$$

When the applied current $i(t)$ exceeds the critical current $I_C$, part of the current goes into the resistor and thus creates a voltage across the junction. This induced voltage causes a time-dependant current $i_J$ through the connection of phase change $\varphi$ and a voltage across the junction. This voltage and current is periodic in time with the period $\Theta$. The period $\Theta$ is defined by the rate of $\Phi_0$ and $< v(t) >$ and thus the frequency is $f =< v(t) > /\Phi_0$.

If $i < I_C$, the average voltage $< v(t) >$ will have a smaller period. The voltage

44

signal is not changed sinusoidally. When $i \gg I_C$, the voltage and current across the junction oscillates sinusoidally.

Practical SQUID magnetometer counts the number of a periodic voltage to measure the flux. With existence of external magnetic flux and shunted resistor, the voltage across the Josephson junction can be measured. For the simplicity, if the $\beta_c \ll 1$, the capacitance will be ignored in the analysis. Also, the inductance of superconductor $L$ is not considered in this initial analysis. The current relation tells us

$$i = i_{J_1} + i_{J_2} + i_{R_1} + i_{R_2}. \tag{3.69}$$

The above equation can be written as

$$i = I_C \sin \varphi + \frac{1}{R} \frac{\Phi_0}{2\pi} \frac{d\varphi}{dt}, \tag{3.70}$$

where

$$I_C = 2I_{C_1} \cos \frac{\pi \Phi_{ext}}{\Phi_0}. \tag{3.71}$$

If the driving current $i$ is greater than the effective critical current $I_C$ at zero applied flux, then a voltage will be produced across the Josephson junction. This voltage $v(t)$ has a DC component $< v(t) >$

$$< v(t) > = iR \sqrt{1 - [\frac{2I_{C_1}}{i} \cos \frac{\pi \Phi_{ext}}{\Phi_0}]^2} \tag{3.72}$$

$$= iR \sqrt{1 - (\frac{i_{max}}{i})^2} \tag{3.73}$$

Since the maximum critical current $i_{max}$ is periodic with respect to the applied flux, the average voltage $< v(t) >$ has the same periodicity of a flux quantum $\Phi_0$.

## 3.5 Circuit Description

We now proceed to show the equivalent electronic circuit model of the voltage-current relation of an ideal Josephson junction describing in Equation 3.22. A Josephson junction is a two-port nonlinear element and as shown in Fig. 3.12b. Fig. 3.12a shows the circuit implementation of this nonlinear dynamic equation. We will use divide and conquer strategy to analyze this equivalent electronic circuit model. This strategy divides the model into four parts: from left to right, LVCVS (Linear Voltage Controlled Voltage Source), INT(INTegrator), NLVCCS( Nonlinear Voltage Controlled Voltage Source) and LVCCS (Linear Voltage Controlled Current Source ).

Now we start discussing each part in details. The left one is a LVCVS, a linear voltage controlled voltage source with the gain of 1. The function of this component is to provide the voltage source $v(t)$ . This component first catches the voltage $v(t)$ across the Josephson junction and then feeds it into the integrator.

The next component is an INT. It is an idea integrator which processes the voltage $v(t)$ information obtaining from the LVCVS. The INT, carrying with a coefficient, implements the formulation of

$$\frac{2\pi}{\Phi_0} \int_0^t v(\tau)d\tau. \tag{3.74}$$

In the specific circuit form of an idea integrator, a capacitor is placed in negative feedback loop of an operational amplifier.

Following the INT, we observed that SIN, a nonlinear voltage controlled voltage source, is used to generate a sinusoidal voltage change of the output voltage from the integrator.

In the last part, we would like to convert the output voltage from the SIN into the current with a coefficient of $I_0$. Therefore, we use a linear voltage controlled current source (LVCCS) to support this function.
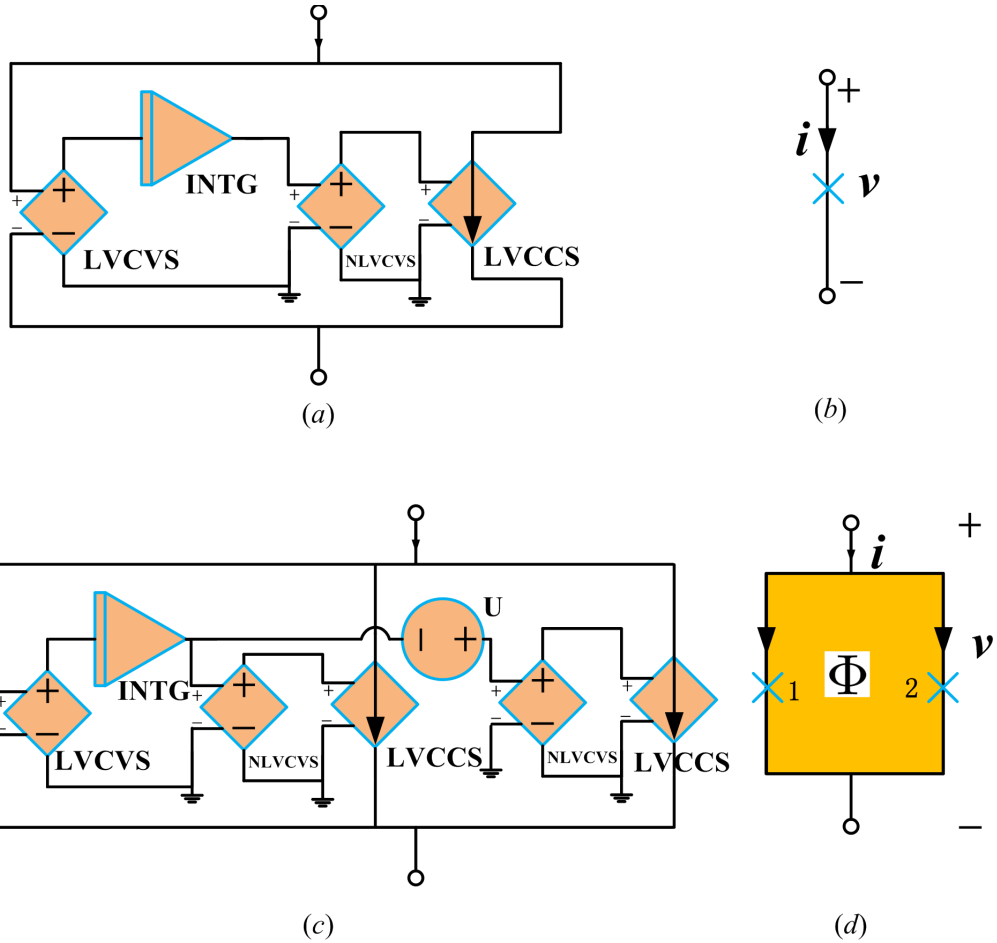
FIGURE 3.12: (Color online) Equivalent circuit models of an ideal Josephson junction and a DC SQUID. (a) Block diagram of an ideal Josephson junction model. LVCVS denotes a linear voltage controlled voltage source with a gain of 1. This component catches the voltage $v(t)$ across the Josephson junction and feeds it into the integrator. INTG represents an ideal integrator with an integral $\int$ over time $t$ of the voltage $v(t)$ and a coefficient $\frac{2\pi}{\Phi_0}$. NLVCCS is a nonlinear voltage controlled voltage source, which implements the voltage transfer function with the expression of $\sin(V + \Phi_0)$. LVCCS denotes a linear voltage controlled current source with a gain coefficient of $I_c$. All components, including LVCVS,NLVCVS, ING and LVCCS, are implemented by SPICE 3 (Simulation Program with Integrated Circuit Emphasis version 3). (b) Circuit symbol of an ideal Josephson junction. $v$ is an applied voltage and $i$ is the current through the Josephson junction. (c) Block diagram of an ideal DC SQUID model. DC SQUID consists of two parallel Josephson junction. U is an equivalent voltage source with the value of $2\pi\frac{\Phi}{\Phi_0}$. This voltage U represents the guage-invariant phase difference between Josephson junction 1 and Josephson junction 2. (d) Circuit symbol of an ideal DC SQUID. $\Phi$ is the external magnetic flux.

47

In the specific circuit form of an idea integrator, a capacitor is placed in negative feedback loop of an operational amplifier. If we give the initial value of the voltage $v(t)$, the current $i(t)$ can be obtained by SPICE solver.

Beyond the ideal equivalent circuit model, above process gives us a chance to extend our study. One small step is that the equivalent circuit of a general Josephson junction can be easily constructed by adding the necessary passive elements to the ideal Josephson junction model. One possible way is to form a resistive shunted junction(RSJ) model by connecting a parallel resistor to the circuit of an ideal Josephson junction model. Furthermore, If we add a parallel capacitor to the RSJ model, we will obtain a resistivity and capacitively shunted junction (RCSJ) model.

In order to verify our functionality of the equivalent circuit model of a Josephson junction, we first examine the AC Josephson effect of a RSJ model. As shown in Figure 4(a), an ideal DC voltage source is used to drive a Josephson junction. In our RSJ model, the Josephson junction has an junction resistance of 0.5 $\Omega$ , and an critical current of 0.1 mA. Figure 4(b) plots the simulation result of the current as a function of time. Our result is consistent with the analytical result.

The second example is a Josephson junction driven by an ideal DC current source, as shown in Figure 5(a). The simulation result of the voltage versus time is plotted in Figure 5(b). Again, good agreement is observed between this result and the reference result in Reference [2].

The third example is used to study the voltage-current relation of a JJ. The circuit we used is similar to the one shown in Figure 5(a). The only difference is from the DC current source. For each value of the DC current source, the voltage variation with time is simulated and the oscillation results are averaged to obtain a corresponding voltage. Our computational results for the voltage-current relation are shown in Figure 6. It shows our results are almost the same as the reference results in paper [2], which verifies the SPICE equivalent circuit model of the JJ.

With the aid of the model of a single Josephson junction, we could build the framework of the modelling and analysis of a large scale superconducting quantum interference filter devices in a dynamical electromagnetic environment. To do this, we shall have to digress a moment to review an ideal situation: the current interference in a superconducting quantum interference device (SQUID).

A SQUID consists of two Josephson junctions in parallel, as shown in Fig. 3.12d. Two Josephson junctions and the superconducting wires forms the closed superconducting loop with a small area $S$. However, the SQUID is not a useful device unless the external magnetic field acts upon this area. It will produce the net magnetic flux $\Phi_e$. This external magnetic flux $\Phi_e$ plays a key role in adjusting the current interference pattern in a closed superconducting loop.

Based upon the classic condition of the flux quantization, we have that the Gauge-invariant phase difference between junction 1 and junction 2 is

$$\Delta\varphi = \varphi_1 - \varphi_2 \tag{3.75}$$

$$= 2\pi\frac{\Phi_e}{\Phi_0}, \tag{3.76}$$

If we assume

$$\varphi_1 = \varphi_0 - \pi\frac{\Phi_e}{\Phi_0} \tag{3.77}$$

$$\varphi_2 = \varphi_0 - \pi\frac{\Phi_e}{\Phi_0}. \tag{3.78}$$

$$\tag{3.79}$$

We do the superposition of two Josephson currents and then obtain the total interference current

$$i = I_0 \sin\varphi_0 \cos\pi\frac{\Phi_e}{\Phi_0}. \tag{3.80}$$

This total current will rapidly oscillate when the external magnetic flux varies with respect to time $t$. Furthermore, the maximum current happens whenever the external magnetic flux encounters

$$\Phi_e = n\pi\Phi_0. \tag{3.81}$$

It is easy to extend the basic Josephson junction model to the generalized Josephson junction model with a parallel resistance $R$ and a parallel capacitance $C$. The parallel resistance $R$ characterizes the dissipative current due to the normal electron tunnelling through the junction; The capacitance $C$ considers the geometrical structure factor of the junction. Now we could modify the basic junction model into a resistivity and capacitively shunted junction (RCSJ) model:

$$i(t) = I_0(t)\sin\varphi(t) + \frac{1}{R}\frac{\Phi_0}{2\pi}\dot{\varphi} + C\frac{\Phi_0}{2\pi}\ddot{\varphi}. \tag{3.82}$$

If the driving current $i$ is slightly larger than the critical current $I_0$, and the junction is working at a strongly overdamped region, says the capacitance $C = 0$, the time average voltage $\overline{V}$ across the junction has the following simple relation

$$\overline{V} = R\sqrt{i^2 - I_0^2}. \tag{3.83}$$

We found that the $\overline{V}$ is propositional to the shunted resistance $R$ and the square root of $i^2 - I_0^2$.

We have examined qualitative results of a DC SQUID. In the following section, we would like to discuss the equivalent electronic circuit of a DC SQUID. We have noticed that there exists a new quantity, the external magnetic flux. Then, we would ask how do we simulate this physical quantity in our circuit environment?

We first construct an equivalent voltage source $U$ to represent the phase difference $\Delta\varphi$. From Equ. 3.75, we know this phase difference is related to the change of the

external magnetic field. As shown in Fig. 3.12c, we then put the voltage source $U$ between the output port of the integrator of the first junction and the input port of SIN of the second junction. Notice that for the first junction, we do not change the form of the equivalent circuit. However the circuit of the second junction has been changed due to additional external magnetic field.

Until now, we completed the electronic circuit description of a DC SQUID. We are going to look at the larger scale junction network, called one dimensional identical SQUID. One dimensional identical SQUID is also called a multijunction interferometer which has $N$ uniform Josephson junctions connecting in parallel by superconducting wires. Each junction applies the same bias current and the loop area enclosed by two adjacent junctions are identical. The phase difference between two adjacent junctions is still governed by the magnetic flux quantization condition:

$$\varphi_k = \varphi_k - \varphi_{k-1} \tag{3.84}$$

$$= 2\pi \frac{\Phi_k}{\Phi_0}. \tag{3.85}$$

Here $\Phi_k$ is the net magnetic flux through the $k^{th}$ loop. Because the larger number of junctions are placed in parallel, this multijunction interferometer could response to a tiny magnetic field comparing with a symmetrical two junction system.

Recently, it is interesting that a new DC SQUID system consisting of nonuniform loop areas has show extraordinary feature for detecting a magnetic field . The new DC SQUID, called superconducting quantum interference filter (SQIF), exhibits the non-$\Phi_0$ period Vee-shape magnetic flux to voltage transfer relation. Moreover, the global minim of average voltage is achieved at the zero of magnetic field. The novel interference pattern makes a SQIF useful for an absolute magnetic field sensor.

Table 3.2: *The major properties of series array of dc SQIUDs as current amplifier*

| Items | Value |
|---|---|
| Technology | thin-flim Nb |
| Loop numbers | 1000 |
| Bandwidth | |
| Dynamic range | |
| Noise level | |
| DC voltage response function | $\langle V \rangle$ |
| Noise level | |
| Target | linear flux-to-voltage conversion |
| Limitations | background shielding and homogeneity on Junctions |

Table 3.3: *SQIF loop size in literature.*

| Loop number | Connection | Loop areas ($\mu m^2$) | The junction width ($\mu m$) |
|---|---|---|---|
| 211 | Series [12] | [38 , 200] | 2 |
| 29 | Series [42] | [29,166] | N/A |
| 20 | Series [54] | [35,700] | N/A |

## 3.6 Superconducting Quantum Interference Filters (SQIFs)

The SQUID magnetometer is the direct application of the Josephson junction. A conventional superconducting magnetic field sensor includes a superconducting quantum interference device(SQUID) and a pick-up coil which focus external magnetic field into the SQUID-loop[53, 43, 42, 41, 31, 13, 11]. For the identically coupled SQUID array, the DC voltage $< v(t) >$ is a periodic function of external flux $\Phi_{ext}$ with a period of flux quantum $\Phi_0$. Table 3.2 presents the major properties of series array of dc SQIUDs as current amplifier

Furthermore, SQIFs are SQUIDs network with a special distribution of loop areas. The SQIFs can be used as absolute magnetic field sensors. In order to increase the signal strength, the network topology of either serial SQUID array or parallel SQUID array is used. The sensitivity of the sensor is enhanced by the square root of the numbers of loops, $\sqrt{N}$ [15, 16, 19, 30, 50, 39]. Table 3.3 gives some typical SQIF loop sizes in literature.
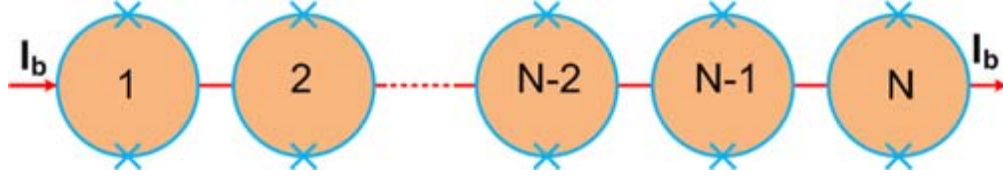
FIGURE 3.13: The diagram of 1D uniform series SQUID array
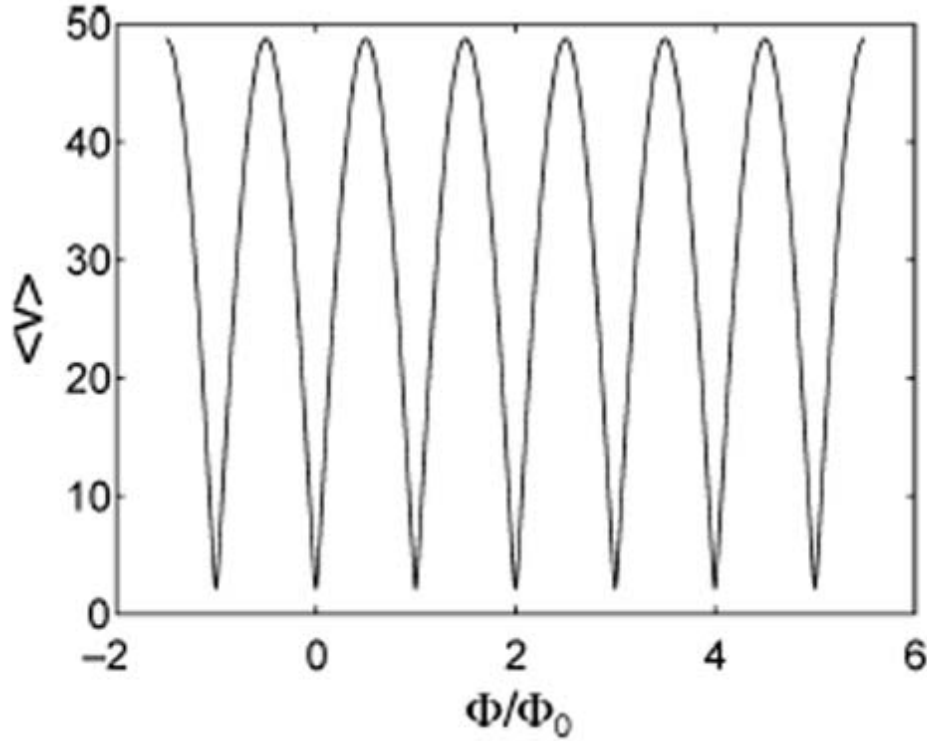


FIGURE 3.14: The average voltage response $< v(t) >$ as a function of the external magnetic flux for an uniform SQUID array, where N = 50, $\beta = 1$ and $I_b = 1.001 I_C$.

Fig. 3.13 gives the configuration of an uniform 1D SQUID array with a series topology. Typically, the grid area in SQUID array is given by $S_g = 10^{-5} \times 2 \times 10^{-5} = 2 \times 10^{-10}$ m$^2$ = 20 $\mu$m$^2$. A typical magnetic flux $\Phi$ is given by $< B, S >= 2.5133 \times 10^{-6}$ $T \times 20$ $\mu m^2 = 5.0266 \times 10^{-16}$ $T - m^2$ $\approx \frac{1}{4}\Phi_0$

Fig. 3.14 gives the voltage response with different external flux values. Fig. 3.15 gives the configuration of an uniform 1D SQUID array with a parallel topology.

53
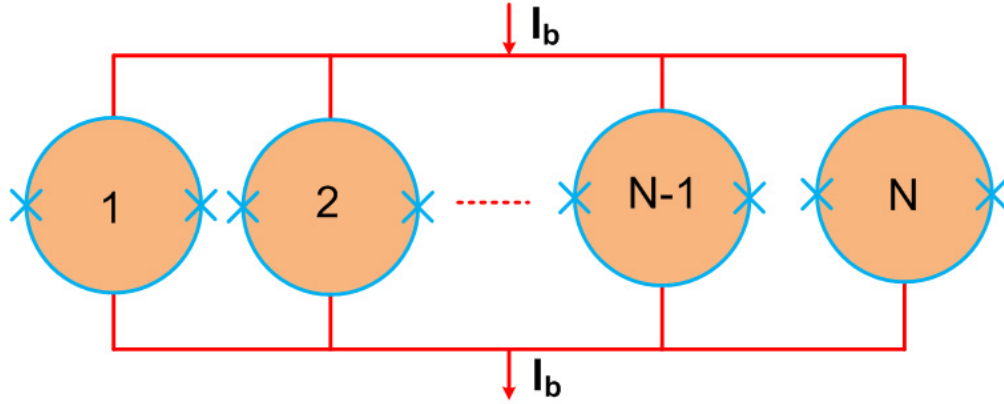
FIGURE 3.15: The diagram of 1D uniform parallel SQUID array
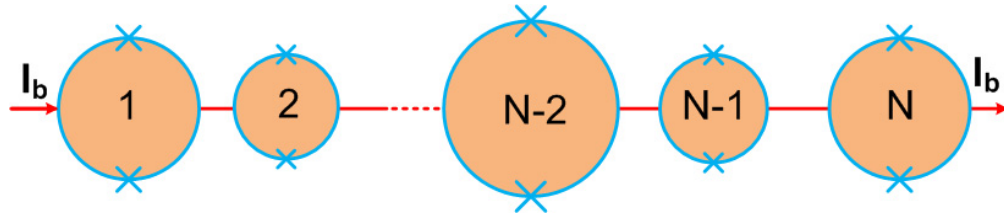


FIGURE 3.16: The diagram of 1D nonuniform parallel SQUID array

Fig. 3.16 gives the configuration of a nonuniform 1D SQUID array with a series topology. The individual loop size is different and the whole loop distribution can be optimized to the desired voltage pattern. For the non-uniform SQUID array, the average voltage response $< v(t) >$ is shown in Fig. 3.18. When the external magnetic field is zero, the corresponding voltage response is zero. If we choose the linear part as the operation region, very small change of external flux $\Phi_{ext}$ will have a relative large variation of average voltage $\Delta < v(t) >$. To increase the linearity, the larger number of loops are used. Therefore, this system can be used as a low noise amplifier (LNA) even without a metallic antenna. Two functions are receiving the signal and amplify the small signal. The dynamic range is defined by the the ratio of the largest voltage and the smallest voltage.
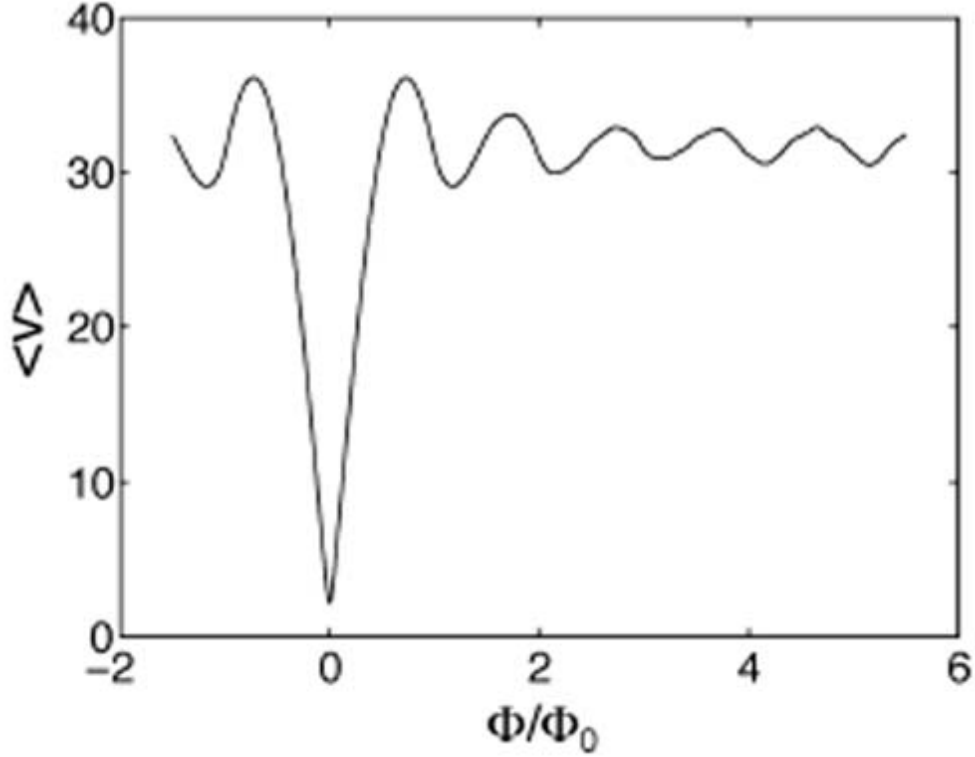
FIGURE 3.17: The average voltage response $< v(t) >$ as a function of the external magnetic flux for a nonuniform SQUID array, where N $= 50$, $\beta = 1$ and $I_b = 1.001 I_C$.

## 3.7 Uniform and Nonuniform 2D SQIF B-field Antenna

We are going to investigate the analysis and synthesis of 2D SQIF array. [55, 54, 40, 38, 35, 34, 33, 32]

### 3.7.1 Uniform Distributions

In order to characterize the SQIF area effect, we studied three different uniform 2D SQIF arrays: $20 \times 10$, $20 \times 15$ and $15 \times 20$. This first SQIF array is a $20 \times 10$ rectangular array. We increase 5 layers along $y$ direction for the second array. The third array has the same area size but exchange the order of the parallel and series connection. For all three cases, the $x$ direction array space $\Delta x$ is fixed at 10 $\mu$m and the $y$ direction array space $\Delta y$ is fixed at 20 $\mu$m .

55
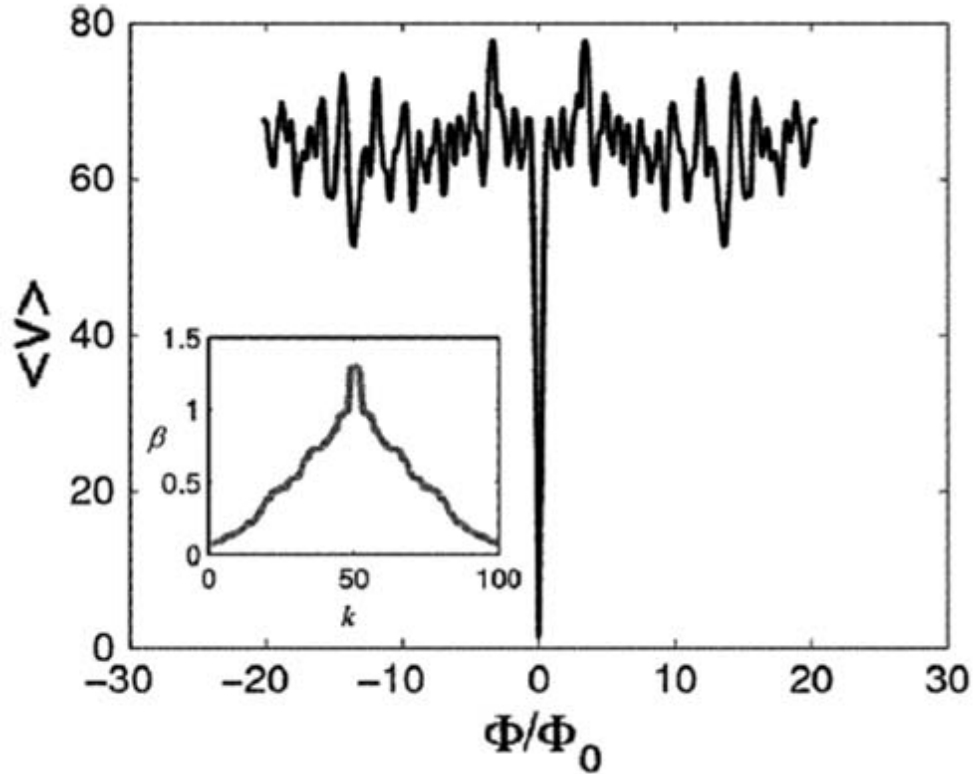
FIGURE 3.18: Voltage response for an arrangement of triangle distribution structures. N=100.

Two sources are used in our system. First, as shown in Fig. 3.20, an external magnetic field $\boldsymbol{B}_{ext}$, propagating along $x$ direction, is excited with an amplitude 0.2 V/m. The polarization of $\boldsymbol{B}_{ext}$ is $z$ direction. The second sinusoidal source is excited at the position $(0, 0, -20)$ m to $(0, 0, 20)$ m. The source has a magnitude of 100 V. The critical current is 0.1 mA and the resistance is 0.2 Ohm.

### 3.7.2 Chebyshev distribution

There is a nature question to ask, without changing the total 2D SQIF array area, whether certain nonuniform interference array distributions will increase or decrease the performance of $\boldsymbol{B}$ antenna system. To answer this question, one of potential solutions is to precisely synthesize a 2D SQIF array with a Chebyshev distribution.

FIGURE 3.19: The $15 \times 20$ rectangular SQIF array with a SQUID dimension of $10~\mu$m $\times 20~\mu$m

Chebyshev distributions are generally utilized in antenna array synthesis techniques. In the following sections, we will start with describing the construction method of the Chebyshev distribution of the first kind and Chevyshev distribution of the second kind along the $y$ direction. All other electric parameters and physic size are the same configuration with respect to uniform cases.
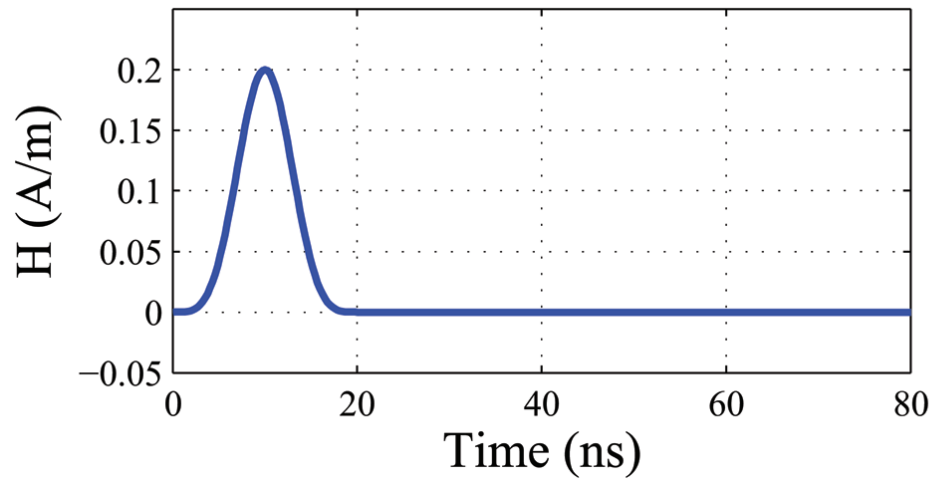
FIGURE 3.20:   An external magnetic field pulse with a peak value of 0.2 A/m
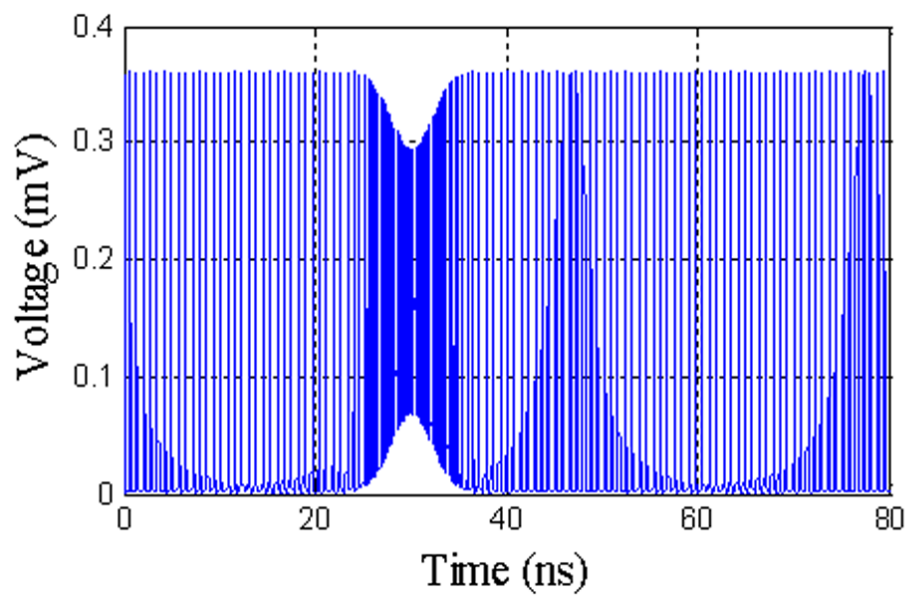


FIGURE 3.21:   Transient voltage response of a $20 \times 10$ SQIF array
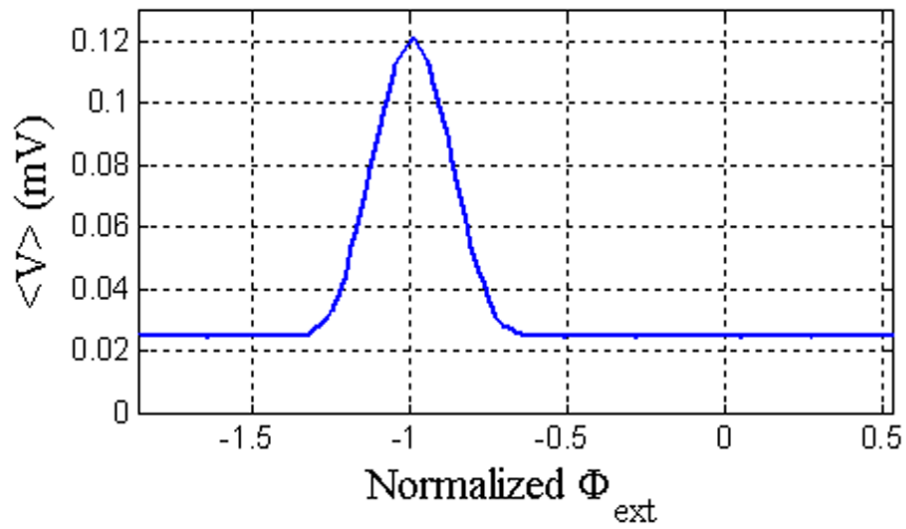
FIGURE 3.22: Averaged voltage response after filtering
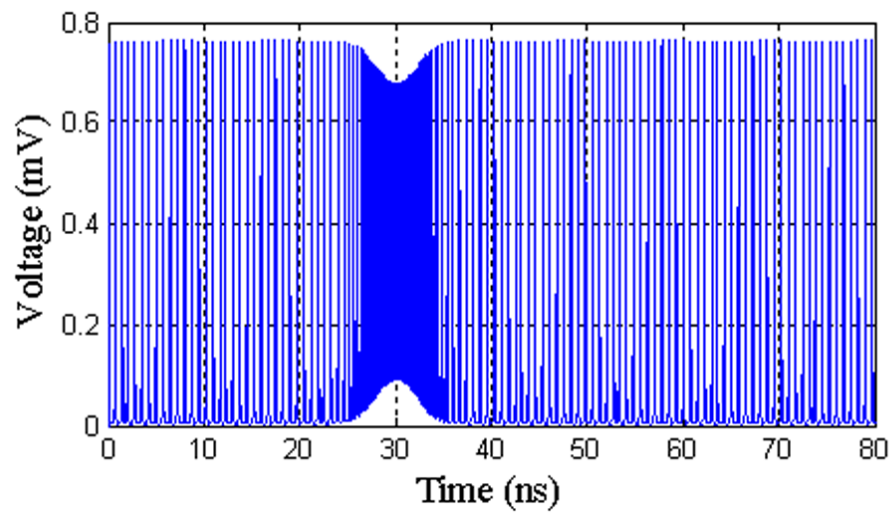


FIGURE 3.23: Transient voltage response of a 15 × 20 SQIF array

59
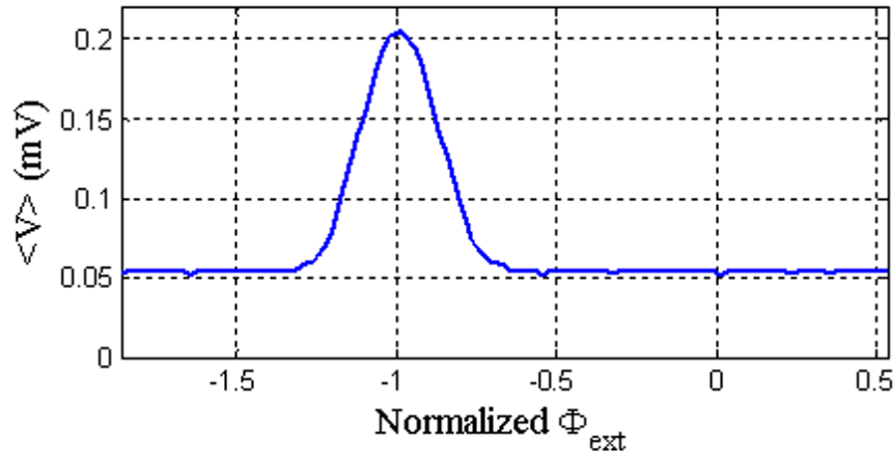
FIGURE 3.24: Averaged voltage response after filtering

### 3.7.3 Chebyshev distribution of the first kind

Mathematically, Chebyshev polynomial of the first kind is defined by $T_n(x) = \cos(n\arccos(x))$. The first six terms are

$$T_0(x) = 1 \tag{3.86}$$

$$T_1(x) = x \tag{3.87}$$

$$T_2(x) = 2x^2 - 1 \tag{3.88}$$

$$T_3(x) = 4x^3 - 3x \tag{3.89}$$

$$T_4(x) = 8x^4 - 8x^2 + 1 \tag{3.90}$$

$$T_5(x) = 16x^5 - 20x^3 + 5x \tag{3.91}$$

The domain of $x$ belongs to $[1,1]$. The polynomials have values between -1 and 1 and all extremes have a value of magnitude one. This is the equal ripple property of Chebyshev polynomials.

A Chebyshev polynomial of the first kind with degree $n$ has $n$ different simple Chebyshev roots in the interval $[1,1]$. In our case, we would like to transform these Chebyshev roots $r_k$ to superconducting junctions' interpolation position nodes $p_k$ in

60
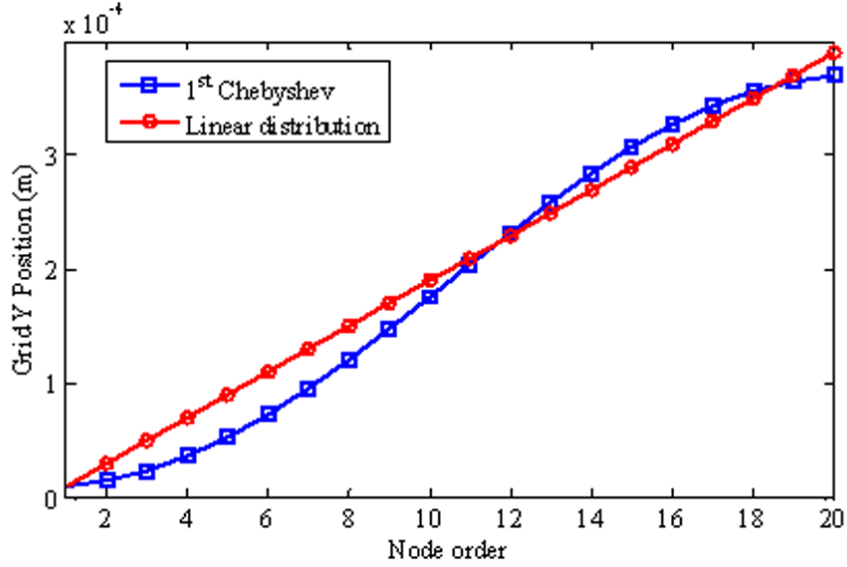
FIGURE 3.25: Compare nodes positions with uniform and $1^{st}$ kind Chebyshev distributions.

the domain [10 $\mu$m , 390 $\mu$m]. The mapping is given by the formula $p_k = r_k \times 180 + 190$

Since the roots of $T_{20}$ are given by

$$r_k = cos(\frac{\pi}{2}\frac{2k-1}{20}), \text{ here } k = 1, 2, \cdots, 20. \quad (3.92)$$

The root vector $\boldsymbol{r}$ is [-0.9969 -0.9724 -0.9239 -0.8526 -0.7604 -0.6494 -0.5225 -0.3827 -0.2334 -0.0785 0.0785 0.2334 0.3827 0.5225 0.6494 0.7604 0.8526 0.9239 0.9724 0.9969]. Therefore, the nodes vector $\boldsymbol{p}$ is [10.5549 14.9734 23.7017 36.5248 53.1269 73.0994 95.9503 121.1170 147.9798 175.8774 204.1226 232.0202 258.8830 284.0497 306.9006 326.8731 343.4752 356.2983 365.0266 369.4451] , here the unit is $\mu$m.

Fig. 3.25 compares $1^{st}$ kind Chebyshev distributions with the nonuniform distributed nodes vector $\boldsymbol{p}$ with a linear distribution with a fixed space of 20 $\mu$m.

Fig. 3.26 gives the received transient voltage from 0 ns to 80 ns. The received peak voltage value $V_{max}$ is captured at $t = 30$ ns. Fig. 3.27 gives the averaged voltage after a low-pass filter.
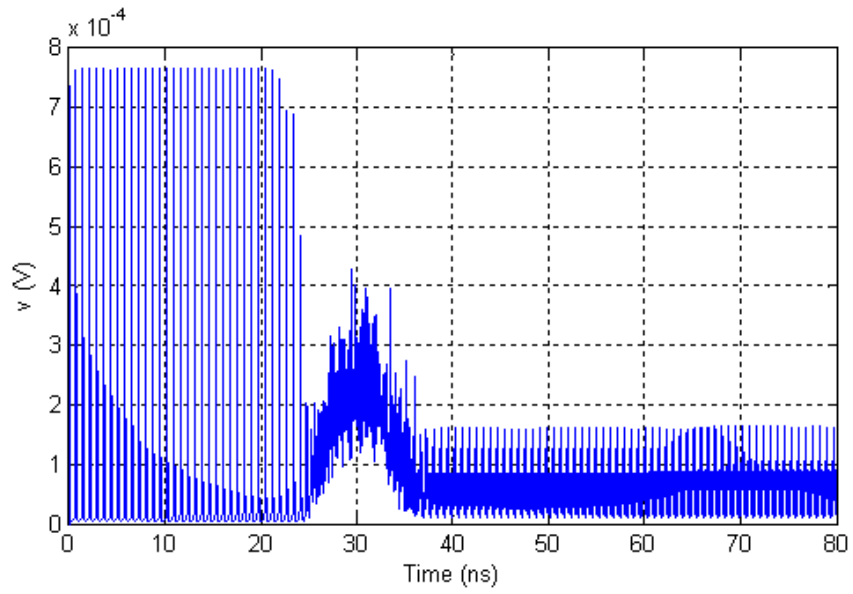
FIGURE 3.26: The received transient voltage at SQIF.
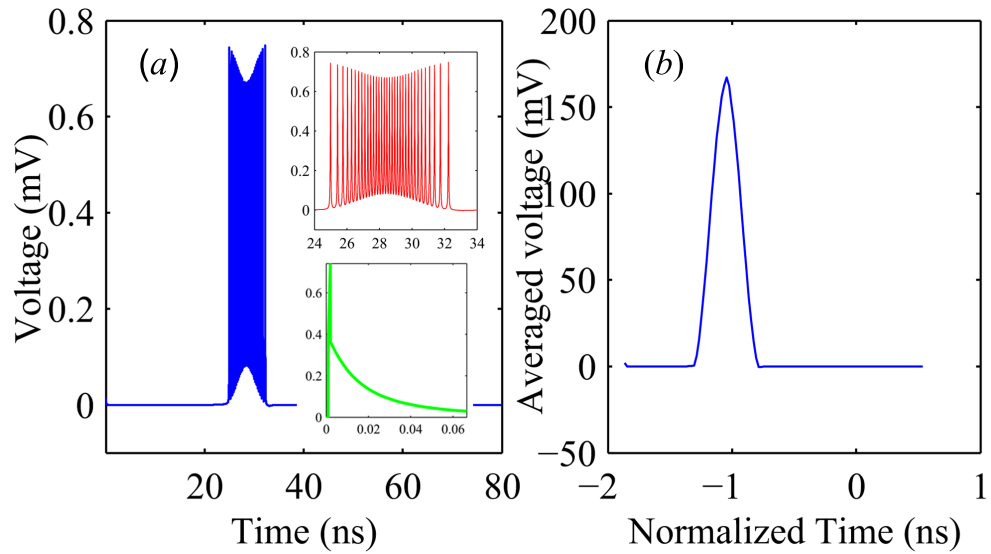


FIGURE 3.27: Averaged voltage after a low-pass filter.

### 3.7.4 Chebyshev polynomial of the second kind

Mathematically, Chebyshev polynomial of the second kind is defined by

$$U_n(\cos(\theta)) = \frac{\sin((n+1)\theta))}{\sin\theta} \tag{3.93}$$

The first six terms are

$$U_0(x) = 1 \tag{3.94}$$

$$U_1(x) = 2x \tag{3.95}$$

$$U_2(x) = 4x^2 - 1 \tag{3.96}$$

$$U_3(x) = 8x^3 - 4x \tag{3.97}$$

$$U_4(x) = 16x^4 - 12x^2 + 1 \tag{3.98}$$

$$U_5(x) = 32x^5 - 32x^3 + 6x \tag{3.99}$$

Again, the domain of $x$ belongs to $[1, 1]$. The polynomials have values between -1 and 1 and the all extremes have magnitude one. This is the equal ripple property of Chebyshev polynomial. A Chebyshev polynomial of the second kind with degree $n$ also has $n$ different simple Chebyshev roots in the interval $[1,1]$. We transform these Chebyshev roots $r_k$ to superconducting junctions' interpolation position nodes $p_k$ in the domain $[10 \ \mu m \ , 390 \ \mu m]$. The mapping is given by the formula $p_k = r_k \times 180 + 190$. Since the roots of $U_{20}$ are given by

$$r_k = \cos(\frac{k\pi}{(20+1)}), \ here \ k = 1, 2 \cdots, 20. \tag{3.100}$$

The root vector $\boldsymbol{r} = $ [-0.9888 -0.9556 -0.9010 -0.8262 -0.7331 -0.6235 -0.5000 -0.3653 -0.2225 -0.0747 0.0747 0.2225 0.3653 0.5000 0.6235 0.7331 0.8262 0.9010 0.9556 0.9888]. Therefore the nodes vector $\boldsymbol{p}=$[12.0105 17.9969 27.8256 41.2770 58.0507 77.7718 100.0000 124.2386 149.9462 176.5486 203.4514 230.0538 255.7614 280.0000
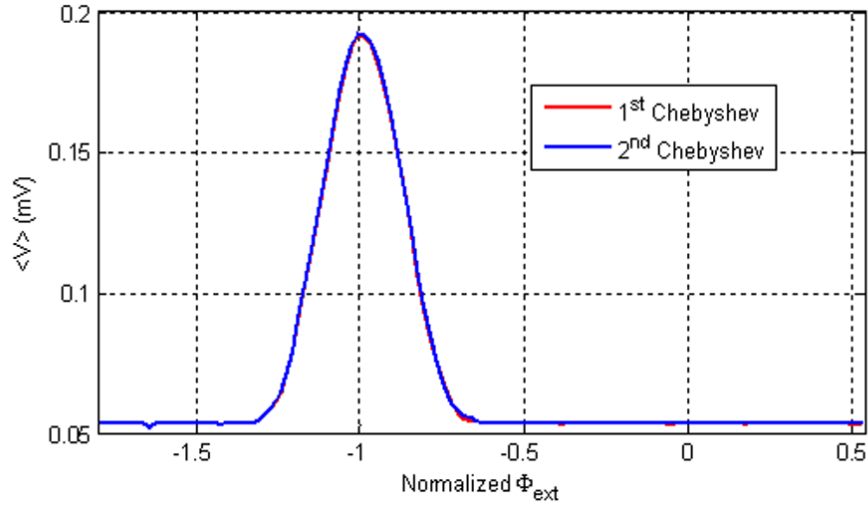
FIGURE 3.28: Comparisons of two kinds of distributions.

302.2282 321.9493 338.7230 352.1744 362.0031 367.9895], here the unit is $\mu$m. Fig. 3.28 compares two kinks of Chebyshev distributions. The space distribution has a little effect on the averaged voltage response. Nonuniform distribution might be a possible design choice for best performance. However two numerical investigations (fig. 3.29) shows the hypothesis might be wrong. It is worth to further investigate the optimal distribution in which the averaged voltage might exceed the performance of uniform distribution without increasing the number of junctions.

## 3.8   Bias current $I_b = 0.99$ mA

In last section, we introduce the concept of a SQIF. Now we will demonstrate how the equivalent circuit of Josephson junctions benefit us in analyzing the superconducting quantum interference filter device. We will find this simulation convenience is the result of multijunction current equation arrays in new SPICE language.

Before we discuss the circuit model of 1D SQIF, it is worthy to review the structure of 1D SQIF. We consider two configurations of 1D Junction array. First, if 1D junction array consists of $N$ general Josephson Junctions in parallel, we call this
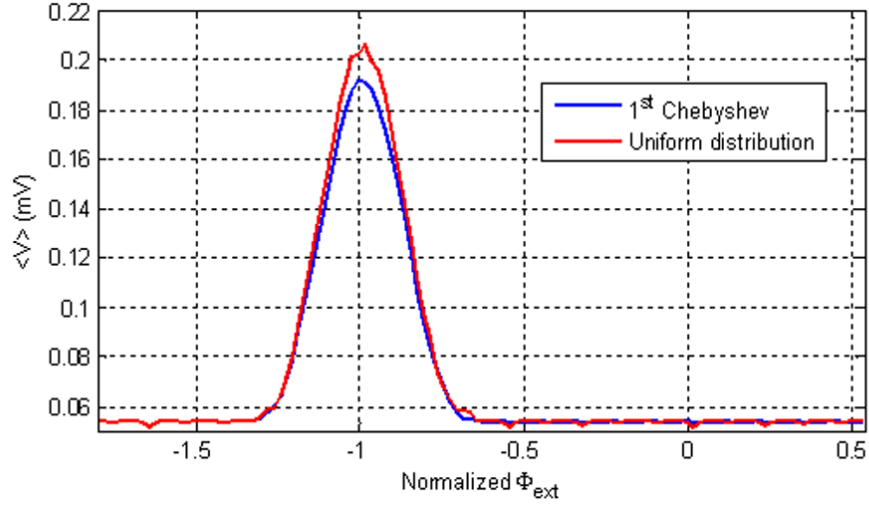
FIGURE 3.29: Comparison of 1st Chebyshev and uniform distribution.

junction array 1D parallel SQIF array. Adjacent junctions forms $N-1$ enclosed superconducting loops with an area $A_n$. If this junction array consists of $M$ SQUID in series , we call 1D series SQIF array. You also notice that 1D series SQIF includes $2M$ Josephson junctions.

According Kirchhoff's current law, the total current $i$ in 1D parallel SQIF is the sum of currents passing through individual junction, resistive channel and capacitive channel. Therefore, for a $N$ junction parallel array, the current interference equation is

$$ i \;\; = \;\; \sum_{n=1}^{N} (I_{0,n} \sin \varphi_n + \frac{1}{R_n} \frac{\Phi_0}{2\pi} \dot{\varphi}_n + C_n \frac{\Phi_0}{2\pi} \ddot{\varphi}_n). \tag{3.101} $$

This is a large scale second order nonlinear dynamical equation of the gauge invariant phase $\varphi$ with a driving current $i$.

In order to complete the description of the dynamics of 1D parallel SQIF, we need supply the magnetic flux quantization condition of adjacent two junctions'
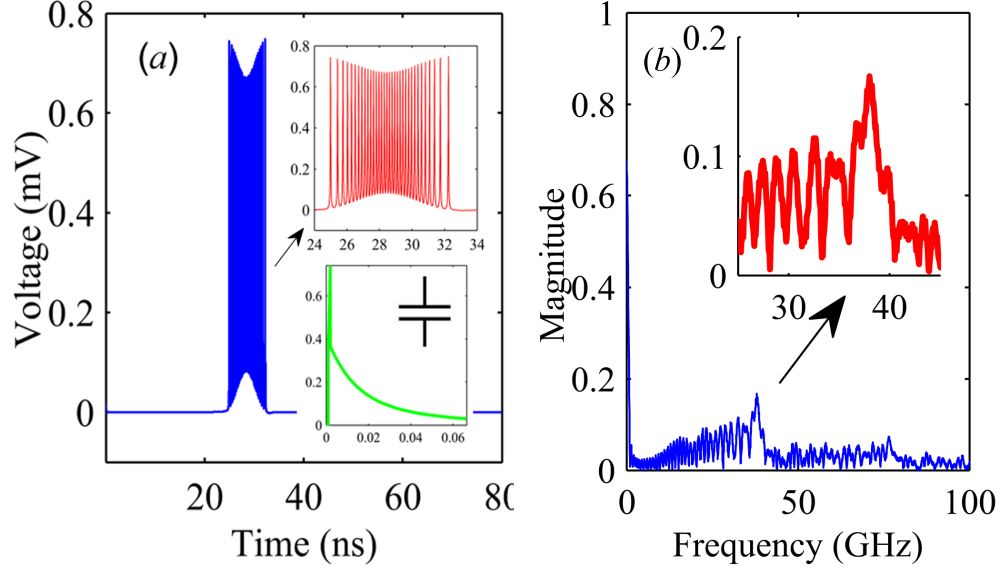
FIGURE 3.30: $I_b = 0.99$ mA. The transmitting Blackman-Harris Window (BHW) pulse signal $S_{BHW}(t)$ is clearly detected by the 2D SQIF array. The excitation duration time $t$ is 80 ns. The magnitude $M$ is 0.2 V/m. The sequence $S_{BHW}[n]$ represents the discretized signal of $S_{BHW}(t)$ calculated by the Modified Trap integration methods . The time interval $\Delta t$ is nonuniform and the sampling points $n = 40017$. The characteristic frequency $f_{char}$ of the BHW pulse is 60 MHz. The 2D SQIF array size $A$ is $16 \times 20$. (a) The received transient voltage waveform $R_{BHW}(t)$. The enlarged green picture at right bottom plots the waveform from 0 to 0.06 ns. The initial value exists due to the voltage at the internal capacitance. The red enlarged curve shows the strong high-frequency oscillation from 25 ns to 34 ns. The peak oscillation voltage $\max\{R_{BHW}(t)\}$ is 0.7435 mV. (b) Averaged voltage $V_{BHW}(t)$ with filtering the high frequency oscillation modulating on the BHW pulse.

phase difference :

$$\varphi_{n+1} - \varphi_n \quad = \quad \frac{2\pi}{\Phi_0} \int \boldsymbol{B} \cdot d\boldsymbol{s}_n. \tag{3.102}$$

here $\boldsymbol{B}$ is the external magnetic field. $\boldsymbol{s}_n$ is the loop area enclosed by the $(n+1)^{th}$ junction and the $n^{th}$ junction.

The average voltage response in this structure is governed by the structure factor

$$S_N(\boldsymbol{B}) \quad = \quad \frac{1}{N} \sum_{n=1}^{N} \frac{I_{0,n}}{I_0} \exp(\frac{2\pi i}{\Phi_0} \sum_{m=0}^{n-1} \int \boldsymbol{B} \cdot d\boldsymbol{s}_m). \tag{3.103}$$
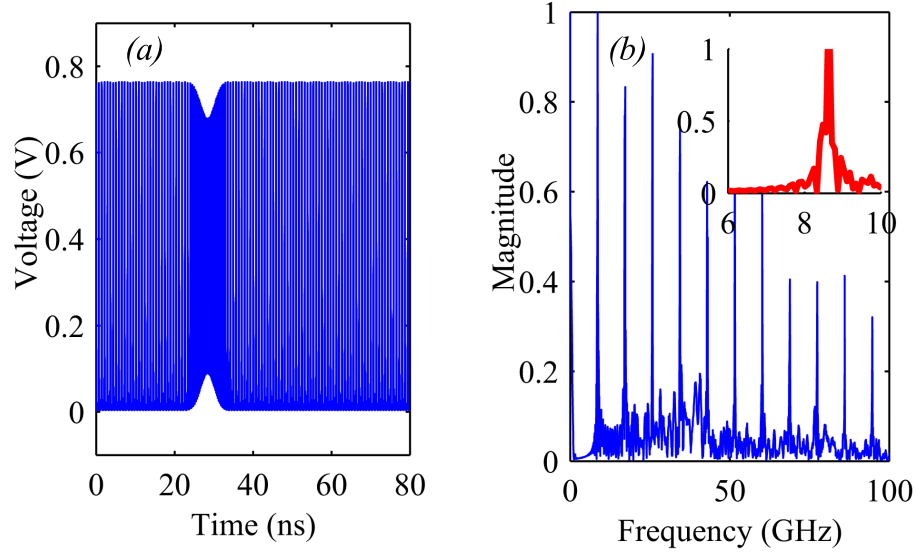
FIGURE 3.31: $I_b = 1.01$ mA. The transmitting Blackman-Harris Window (BHW) pulse signal $S_{BHW}(t)$ is clearly detected by the 2D SQIF array. The excitation duration time $t$ is 80 ns. The magnitude $M$ is 0.2 V/m. The sequence $S_{BHW}[n]$ represents the discretized signal of $S_{BHW}(t)$ calculated by the Modified Trap integration methods . The time interval $\Delta t$ is nonuniform and the sampling points $n = 40017$. The characteristic frequency $f_{char}$ of the BHW pulse is 60 MHz. The 2D SQIF array size $A$ is $16 \times 20$. (a) The received transient voltage waveform $R_{BHW}(t)$. The enlarged green picture at right bottom plots the waveform from 0 to 0.06 ns. The initial value exists due to the voltage at the internal capacitance. The red enlarged curve shows the strong high-frequency oscillation from 25 ns to 34 ns. The peak oscillation voltage max$\{R_{BHW}(t)\}$ is 0.7435 mV. (b) Averaged voltage $V_{BHW}(t)$ with filtering the high frequency oscillation modulating on the BHW pulse.

Here, the average critical current $I_0$ is denoted by

$$I_0 = \frac{1}{N} \sum_{n=1}^{N} I_{0,n}. \tag{3.104}$$

If we do not consider the secondary inductance effect from the circulating current in the loop, the average voltage $\overline{V}$ will be the function of the external magnetic field $\boldsymbol{B}$, which is given by [?]

$$\overline{V} = I_0 R \sqrt{J_N^2 - |S_N(\boldsymbol{B})|}. \tag{3.105}$$

Where the normalized resistance $R$ is defined by

$$R = \frac{1}{N} \sum_{n=1}^{N} \frac{1}{R_n} \tag{3.106}$$

$$J_N = \frac{i}{NI_0} \tag{3.107}$$

$J_N$ is defined by

$$J_N = \frac{i}{NI_0} \tag{3.108}$$

The above analytic result gives the preliminary qualitative relationship of 1D SQIF array and also guides the experimental configuration. However, the simulation work on modelling and analyzing SQIF array based on the SPICE description can be utilized with leveraging the power of computing. This SPICE approach is not quite the same as the analytical method in that it might not tell us much of the fundamental SQIF but it might tell us much of great interest about the new phenomena that occur in complex circuit-field situations. Furthermore, the most important point is that it would have an enormous number of technical applications.

## 3.9   The SPICE model of two dimensional SQIF

Now we proceed to construct and analyze a 2D SQIF array by using our circuit elements. Fig. 3.32 shows the typical equivalent circuit diagram of two-dimensional SQIF with $M$ row in series and $N$ column junction in parallel. Each row is decoupled by normal-metal-resistor films. This structure has benefits in increasing the level of the output voltage and dynamical range, improving the sensitivity of a weak magnetic signal and maintaining strong robustness under the fluctuation of the critical current. Therefore, it had been considered as a far-field wideband magnetic sensor[44, 36, 55, 54, 53, 43, 41, 42].
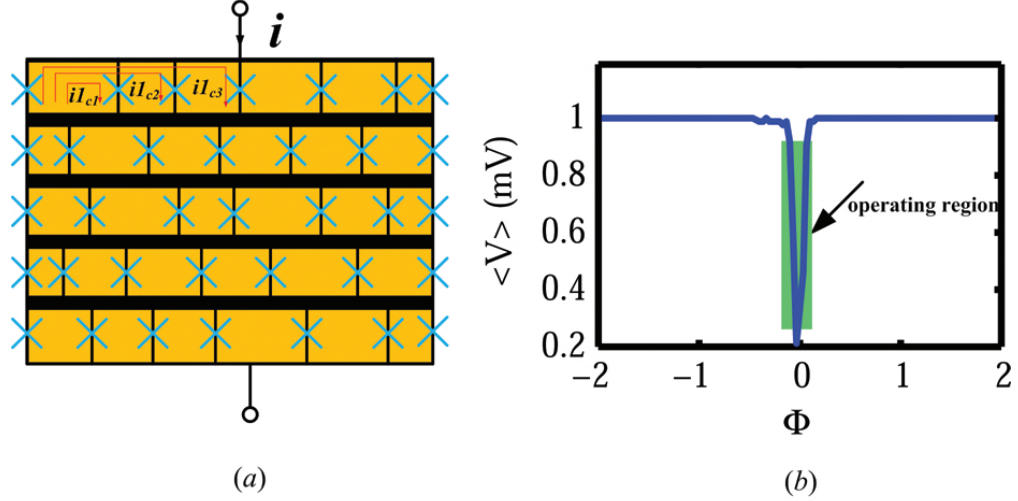
FIGURE 3.32: (Color online) The typical equivalent circuit diagram of two-dimensional SQIF with M row in series and N column junction in parallel.

Our model considers the superposition of all circulating currents $\{i1_{c1},\ i2_{c2},\ i3_{c3}\ \cdots\}$ through all 1D SQIFs. Fig. 3.32b gives the simulated average voltage-flux relationship of a $20 \times 20$ SQIF. $\langle V \rangle$ is the average voltage after filtering and $\Phi$ is normalized external magnetic flux. The green box is the linear operating region in which a small radio frequency (RF) signal can be amplified to a sensible voltage signal.

The inductive voltage across $V$ the junction is arisen by the rate of change of the magnetic flux with the following expression

$$V \ = \ \dot{\Phi}. \tag{3.109}$$

We want to use two steps to decompose the 2D SQIF array. The first step is to look at the rows. As shown in Fig. 3.32a, if we observed the first row, or any other individual row in we find that each row can be treated as a 1D parallel SQIF. The second step is much easier than the first one. We just simply consider 1D parallel SQIF in series.

We have observed the globla structure. Now we move to the localized structure formed by the adjacent junctions. Here, we first define the smallest loop formed

by adjacent junctions as an elementary loop. We call the multiple consecutive elementary loops form a composite loop. We utilize the normal-metal-resistive film to isolate the phase couplings among each row.

How do we treat the gauge invariant phase difference among junctions with respect to the external magnetic field? Two options looks feasible. One possible way is to force the phase difference condition at elementary loops with the relation

$$\varphi(m, n + 1) - \varphi(m, n) \quad = \quad 2k\pi + \frac{2\pi\Phi_n}{\Phi_0}. \tag{3.110}$$

The second direction is to force the phase difference condition at composites loops in the following relation

$$\varphi(m, n + 1) - \varphi(m, 1) \quad = \quad 2k\pi + \frac{2\pi\Phi_n}{\Phi_0}. \tag{3.111}$$

Here $n$ starts from 1 to $N - 1$. Observing the left side, we have obtain $N - 1$ phase difference terms. We use the difference of the other junction minuses the first one as the phase constrain condition. Therefore, we could implement a SPICE model of 2D SQIF with the external magnetic source.

## 3.10   Results and Discussions for a SQIF in an EM Environment

In this section, we will focus on design considerations and simulation results based on the above SQIF framework which was implemented in Wavenology EM. We will observe the interaction between the dynamical magnetic field and 2D SQIF. Then, we discuss the output voltage performance with electrical and geometrical parameters of a Josephson junction. We also demonstrate how loop area size distributions relate to the voltage response across the junction. Finally, we study the effect of array size on the voltage response.

### 3.10.1   Find The Linear Operation Region

A far-field wideband magnetic field sensor need to operate at the linear operation region of a SQIF. We will use three steps to obtain this region. First, we excite a transient linear magnetic field $H$ source, as shown in Fig. 3.33(a). The polarization direction of this magnetic field is normal to the plane of a 2D SQIF with an array size of $20 \times 10$. The magnitude of this magnetic field varies from -3 A/m to 3 A/m. The flux quantization condition converts the magnetic field into a discretized magnetic flux. The quantized magnetic flux produces the nonlinear interference current. This interference current is transferred to the voltage due to the internal Josephson junction resistance channel (here $R = 0.2\ \Omega$). In the second step, Fig. 3.33(b) shows the simulated transient voltage response. The rapid nonuniform oscillation is built. We find that a global voltage minimum is located at the time of 20 ns. This phenomenon corresponds to the situation of a zero dynamic magnetic field. Stationary voltage points (V = 0.18 mV) happen at $t = \{12.5,\ 15,\ 17.5,\ 22.5,\ 25,\ 27.5\}$ ns.

In the last step, if we average the transient voltage signal, we can identify the existence of a linear operation zone and two saturated zones. As shown in Fig. 3.33(c), the average voltage response is plotted versus the normalized magnetic flux. The V-shape linear operation zone is in the range of [-0.04, 0.04]. This region becomes extremely important for designing a far-field magnetic field sensor. We can bias a proper static magnetic field in this region to set up the appropriate operation point. In the next section, we will demonstrate that, at the operation point, a weak dynamical magnetic signal can be detected and amplified. This mechanism resembles a traditional RF amplifier but under a novel working condition. As shown in Fig. 3.33(c), we notice that, outside the linear operation region, the voltage level maintains a constant value of 0.18 mV. We call this zero slope region the saturated region. In this region, the external dynamic magnetic field cannot be effectively

amplified no matter how large it is.

Furthermore, we are curious about the robustness of the linear operation zone when the critical current encounters a statistical distributions due to the variation of fabrication conditions. We use three critical current distributions: an identical distribution, a normal distribution and a uniform distribution. Fig. 3.34 shows simulated transient voltage response of a $50 \times 50$ SQIF identical array. We observe that the rapid voltage oscillation happens for these three distributions. Using the filtering method, we obtain the average voltage $\langle V \rangle$ response of the 2D SQIF, as shown in Fig. 3.35. The agreement of three average voltage responses demonstrates that the flux-voltage characteristics of this 2D SQIF is highly robust under the variation of critical currents. This feature will be practically useful when we fabricate a 2D SQIF.

### 3.10.2  Geometric Effects

In order to optimize a 2D SQIF, we consider the geometric effect with three array configurations: a $20 \times 10$ array, a $20 \times 15$ array and a $15 \times 20$ array. Here, the default bias current is 0.101 mA. The transmitting magnetic pulse is a Blackman-Harris Window (BHW) signal[37].

Fig. 3.36 shows three receiving transient voltage responses. All three 2D SQIFs can recover the original BHW signal. Fig. 3.37 gives the average voltage $\langle V \rangle$ comparison of the three array sizes. We have two findings in Fig. 3.37. First, if we change the 2D SQIF size from $15 \times 20$ to $20 \times 15$, which means we do not change the total area of a 2D SQIF array, the average voltage increases about 0.08 mV. Second, we notice that the increase of the number of parallel junctions improves the average voltage level. This voltage increase comes from the positive current interference between parallel junctions.
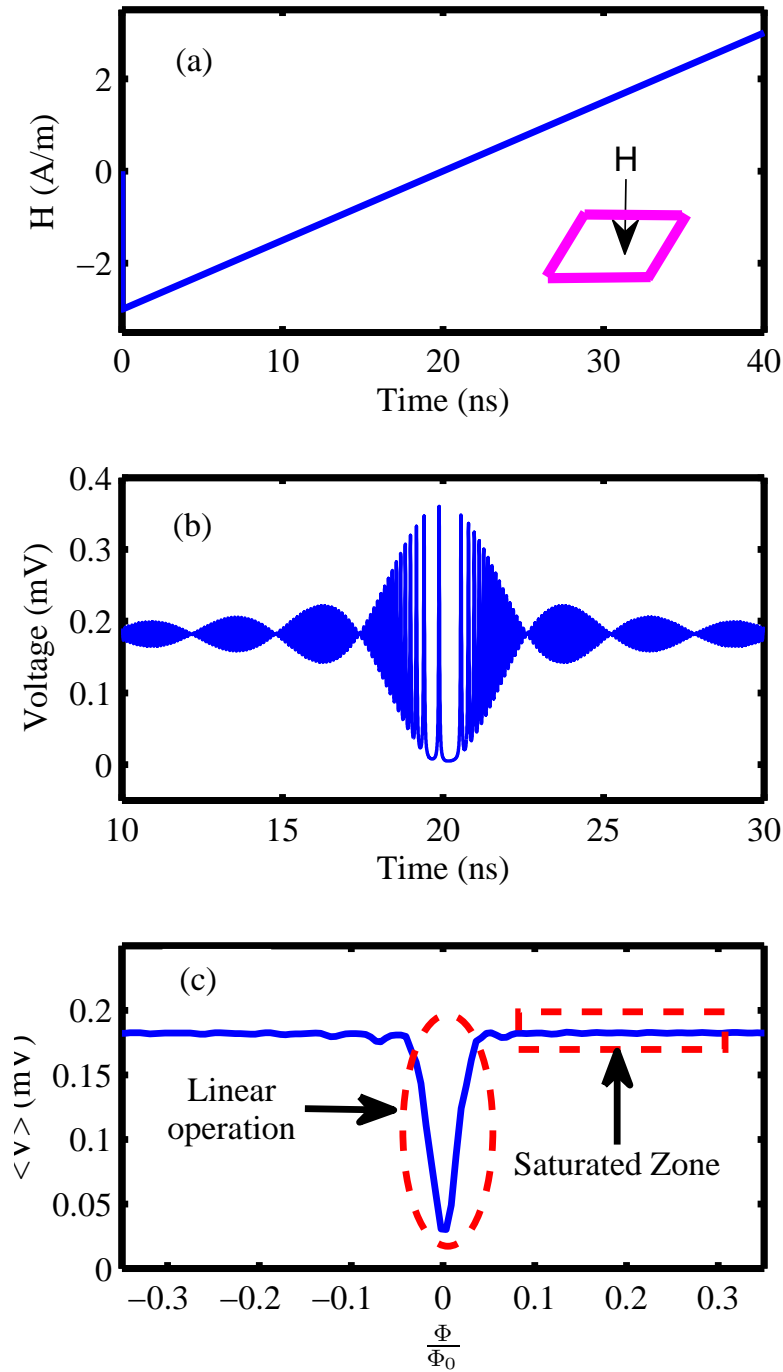
FIGURE 3.33: A 2D uniform superconducting quantum interference filter modulated by a transient linear magnetic field. (a) A linear magnetic field with a magnitude from -3 A/m to 3 A/m. (b) Transient voltage response of a 2D uniform SQIF with an array size of $20 \times 10$. (c) Averaged voltage as a function of normalized magnetic flux. $\Phi$ is the external magnetic flux through an elementary loop. The elementary loop area is 20 $\mu$m $\times$18 $\mu$m. A linear operation zone and a statured zone are observed.
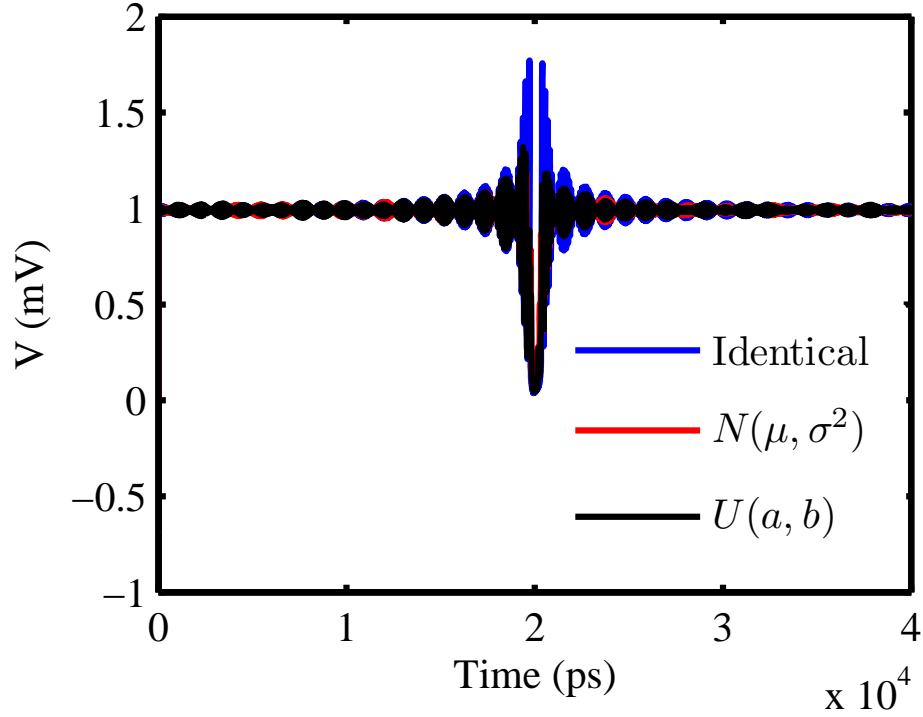
FIGURE 3.34: The simulated transient voltage responses of a $50 \times 50$ 2D SQIF with three critical current distributions: an identical distribution, a normal distribution and a uniform distribution. Here $\mu = I_0 = 0.1$ mA, $\sigma = \frac{I_0}{3}$, $a = 1 - 0.4I_0$ and $b = 1 + 0.4I_0$.

### 3.10.3 Electrical parameter effects

Let us now discuss two electrical parameter effects for a 2D DC SQIF: the bias current and the junction resistance. The question is whether the bias current will dramatically affect the detection performance of a 2D SQIF and how the value of the junction resistance can affect the received transient voltage.

### The Critical Current

The bias current, which is either larger or smaller than the critical current, affects the operation state of a SQUID. However, it is not clear how the bias current affects the operation state. To study this, we consider two cases of a 2D SQIF: $i_b > I_c$ and $i_b < I_c$. In both cases, we assume that the critical current $I_c$ is 0.1 mA and the array size
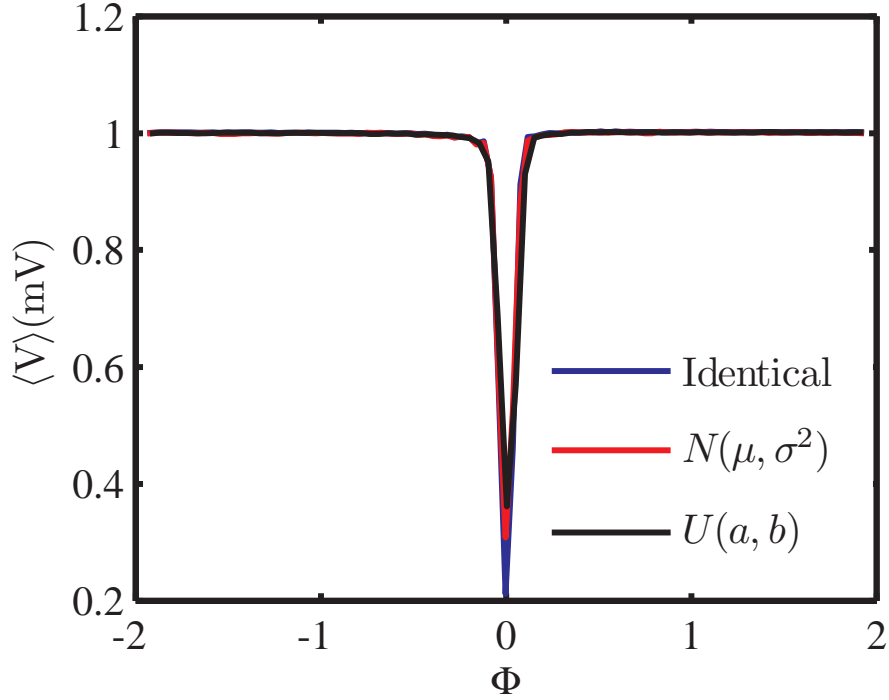
FIGURE 3.35: The averaged voltage $\langle V \rangle$ responses of a $50 \times 50$ 2D SQIF.

of this 2D SQIF is $16 \times 20$. The characteristic frequency of the BHW pulse is 60 MHz. Its magnitude is 0.2 V/m. The excitation duration time $T$ is 80 ns. The field simulation is computed by the finite-difference tim-domain method. The transient voltage signal is calculated by the Modified Trap integration methods. The time interval $\Delta t$ of $V$ is nonuniform and the sampling points are $n = 40017$.

For the first case, we set the bias current equal for individual loops to 0.101 mA, which is one percent larger than the critical current. The reason we do this is that we want to let Josephson junction operate at the RCSJ model. The transient voltage response should be generated across the 2D SQIF. Fig. 3.38 shows the time evolution and frequency characteristics of the voltage response.

In Fig. 3.38(a), we first observed that the transient voltage response has two kinds of rapid oscillations. From 25 ns to 33 ns, the voltage has faster nonlinear oscillations since the external magnetic pulse triggers the 2D SQIF. Outside that
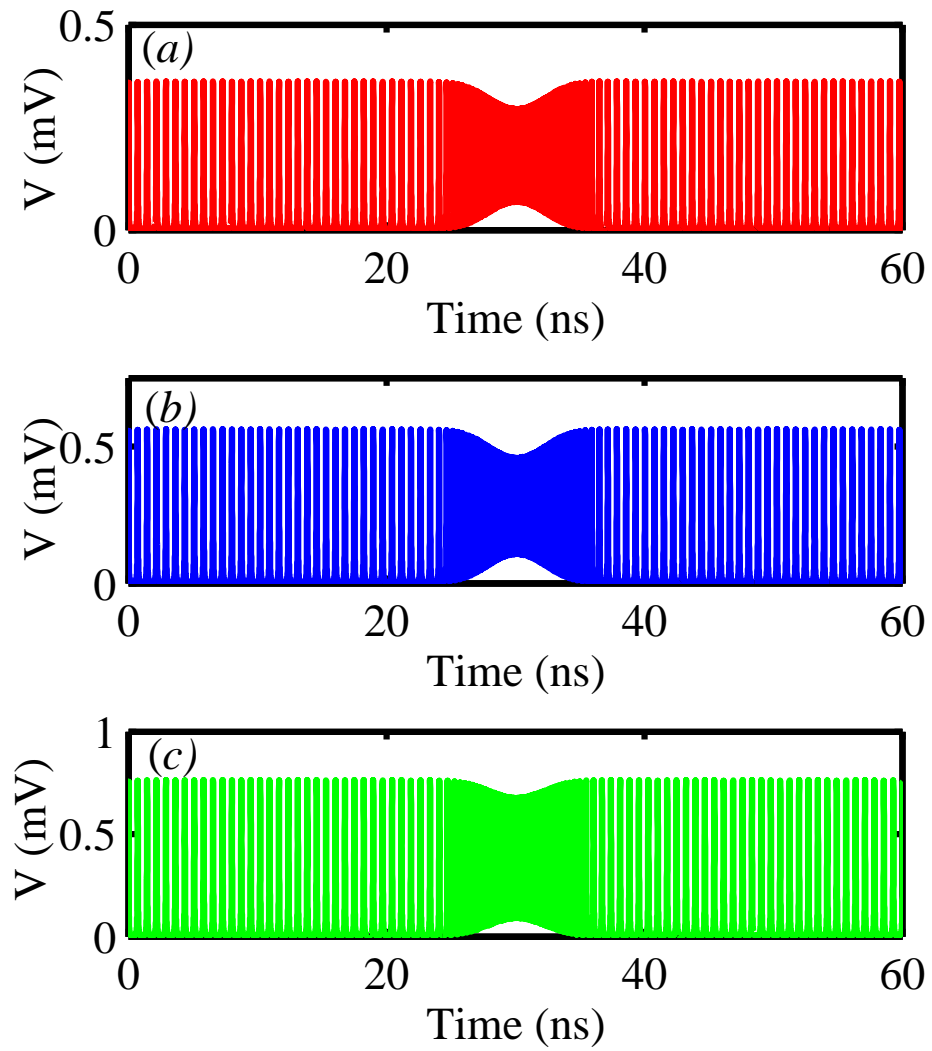
FIGURE 3.36: (Color online) The transient voltage responses of three different array size: (a) $15 \times 20$, (b) $20 \times 10$ and (c) $20 \times 15$.
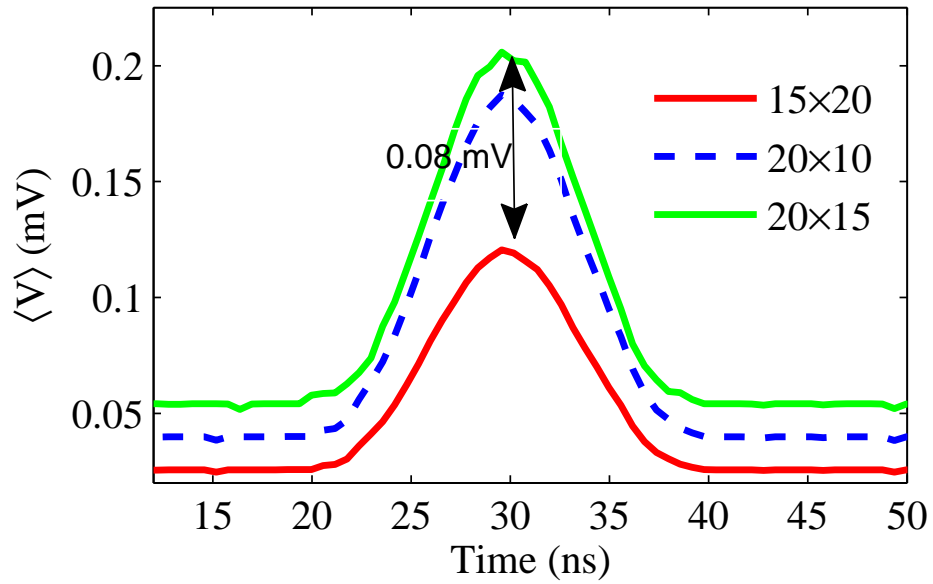
FIGURE 3.37: (Color online) The averaged voltage responses after filtering.
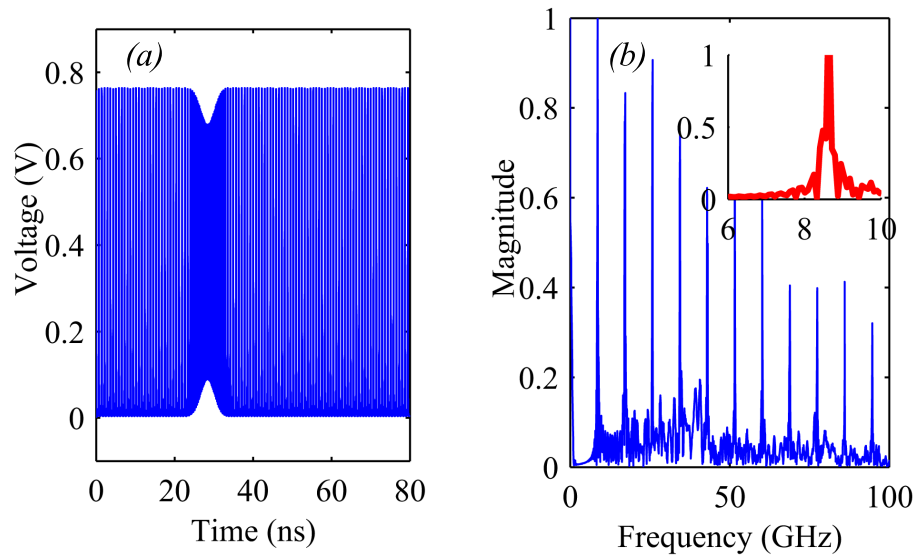


FIGURE 3.38: $I_b = 0.101$ mA. The array size of a 2D SQIF is $16 \times 20$. (a) The transient voltage waveform response. (b) Calculated the frequency spectrum by the fast Fourier transform (FFT).
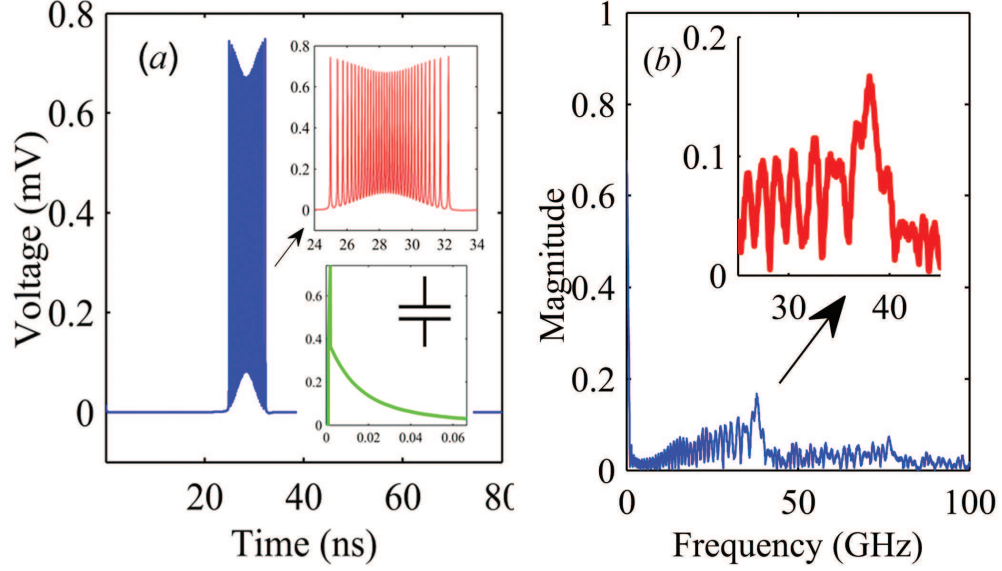
FIGURE 3.39: $I_b = 0.099$ mA. (a) The received transient voltage waveform $R_{BHW}(t)$. (b) Averaged voltage $V_{BHW}(t)$

region, we observed that the intrinsic oscillation has a lower uniform oscillation. Fig. 3.38(b) calculated the frequency spectrum by the fast Fourier transform (FFT).

Let's consider the second case with $I_b = 0.099$ mA, which is slightly smaller than the critical current. Fig. 3.39 shows the time evolution and frequency characteristics of the voltage response. In Fig. 3.39(a), the enlarged green curve at right bottom plots the waveform from 0 to 0.06 ns. The initial value exists due to the voltage across the internal capacitance. The red enlarged curve shows the strong high-frequency oscillation from 25 ns to 33 ns. The peak oscillation voltage is 0.7435 mV. It is interesting that the voltage is zero from 0 ns to 25 ns. The reason for this is that the internal bias current can not trigger the oscillation. After the 25 ns, the original signal is recovered because the 2D SQIF operates at the small-signal linear amplification region. Fig. 3.39(b) calculated the frequency spectrum by the fast Fourier transform (FFT).
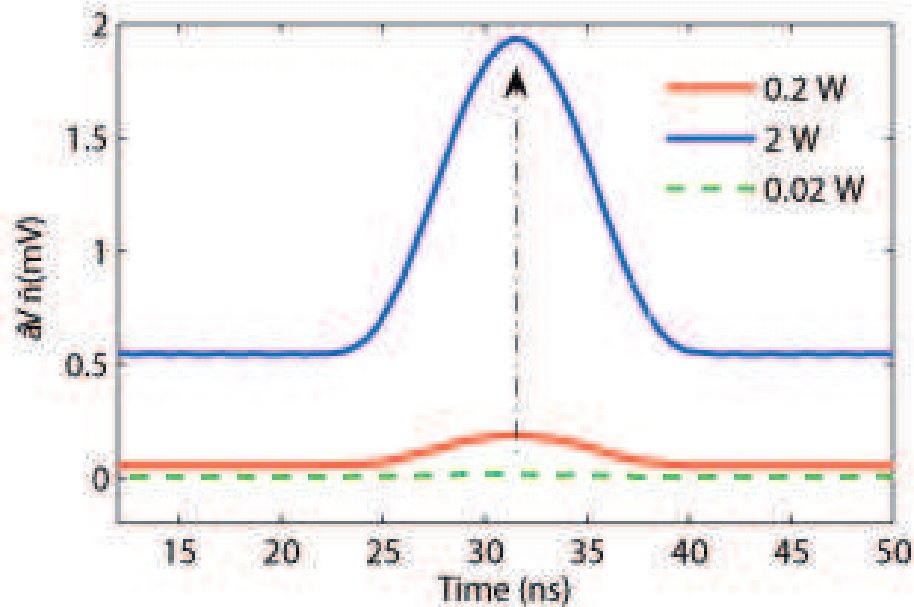
FIGURE 3.40: (Color online) The averaged voltage responses with different junction resistance: $R = 0.02\ \Omega$, $0.2\ \Omega$ and $2\ \Omega$

*The Junction Resistance*

Next, we consider the average voltage response versus the variation of the junction resistance. The junction resistance is an important physical parameter which characterizes the normal electron tunneling of the Josephson junction. Fig. 3.40 shows the averaged voltage responses with the resistance $r = 0.02\ \Omega$, $0.2\ \Omega$ and $2\ \Omega$. The voltage response exhibiters the magnitude variation without dispersion. When the resistance is $0.02\ \Omega$, the receiving averaged voltage signal is very small in this experiment.

*3.10.4   A SQIF Far-field Sensor*

The creation of a 2D SQIF framework, the existence of the linear operation zone and the simulation of the voltage response are key to complete the design of an effective far-field magnetic field sensor. In Fig. 3.33(c), we have identified the linear operation
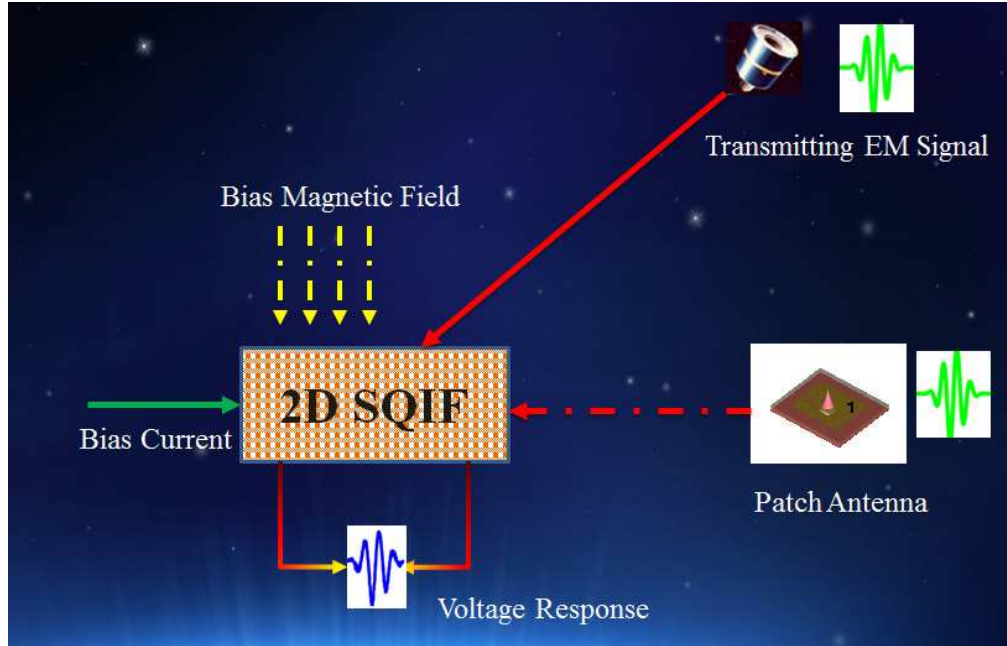
FIGURE 3.41: (Color online) The schematic diagram of a 2D SQIF device in a dynamical electromagnetic field environment. We assume that the Josephson junction resistance is 0.2 $\Omega$ and the critical current is 0.1 mA. The unit length inductance of the superconducting wire is $10^{-8}$ H/m. The junction capacitance is zero.

region and the saturated zone. What would happen when a 2D SQIF is working at different biased static magnetic fields? To answer this question, Fig. 3.41 illustrates the schematic diagram of a 2D SQIF device in a dynamical electromagnetic field environment. Let us imagine that a modulated Blackman-Harris Window (BHW) signal, with a frequency band from 100 MHz to 400 MHz and a magnitude 0.1 A/m, is transmitting from a far-field magnetic field source. The 2D SQIF is tuned at the operation linear region with a bias current 0.101 mA.

Now, let us check the voltage responses with three bias magnetic fields: the small signal condition $H_1 = 0.0068$ A/m, the normal condition $H_2 = 0.1$ A/m and the saturation condition $H_3 = 0.5$ A/m. Fig. 3.42 gives the comparison of transient and average voltage responses with two bias operation magnetic fields. Comparing Fig.3.42(a) with (b), we observe that the larger bias magnetic field produces a faster

nonlinear oscillations. Furthermore, in Fig.3.42(c), we find that the transmitting signal is recovered very well with the bias static magnetic field $H_2$, and if the bias magnetic field $H_1$ is too small, the original signal might not be recovered. This above observation has two-fold meanings. First, it provides the direct evidence of the importance of a proper bias static magnetic field. Second, the successful detection of the original signal reflects the important step towards understanding and designing a practical SQIF magnetic field sensor in a dynamic electromagnetic environment.

Furthermore, If we use a bias magnetic field $H_3 = 0.5$ A/m to do the experiment, the 2D SQIF will operate at the saturated zone. Fig. 3.43 shows the dispersion phenomena arising in this received voltage signal. This result provides the design guidance to avoid the device to operate at the saturated zone.

Next, we extract the envelop signal to capture the transient voltage signal feature, which is modulated by the external magnetic field. Fig. 3.44 gives the envelope waveform extracted by a probabilistic amplitude demodulation (PAD) technique[61]. Here, the PAD is one of amplitude demodulation methods based on probabilistic methods of machine learning.

In summary, working at the linear operation zone by tuning the bias current and the bias magnetic field, a 2D SQIF can act as a dynamic magnetic field receiving antenna and a linear amplifier simultaneously. The simplicity of this idea makes it very appealing for high dynamic range intelligence antenna applications.

### 3.10.5  Design a co-mingled E and B Field Antennas System

In the previous subsection, we have shown that the 2D SQIF can be used as a far-field magnetic field sensor. By connecting a far-field transmitter to the 2D SQIF, we can build a directed wireless link. For practical system level applications, we first require an additional bidirectional wireless link which communicates between the far-field transmitter and the near-field transmitter. Furthermore, the magnetic flux coupling
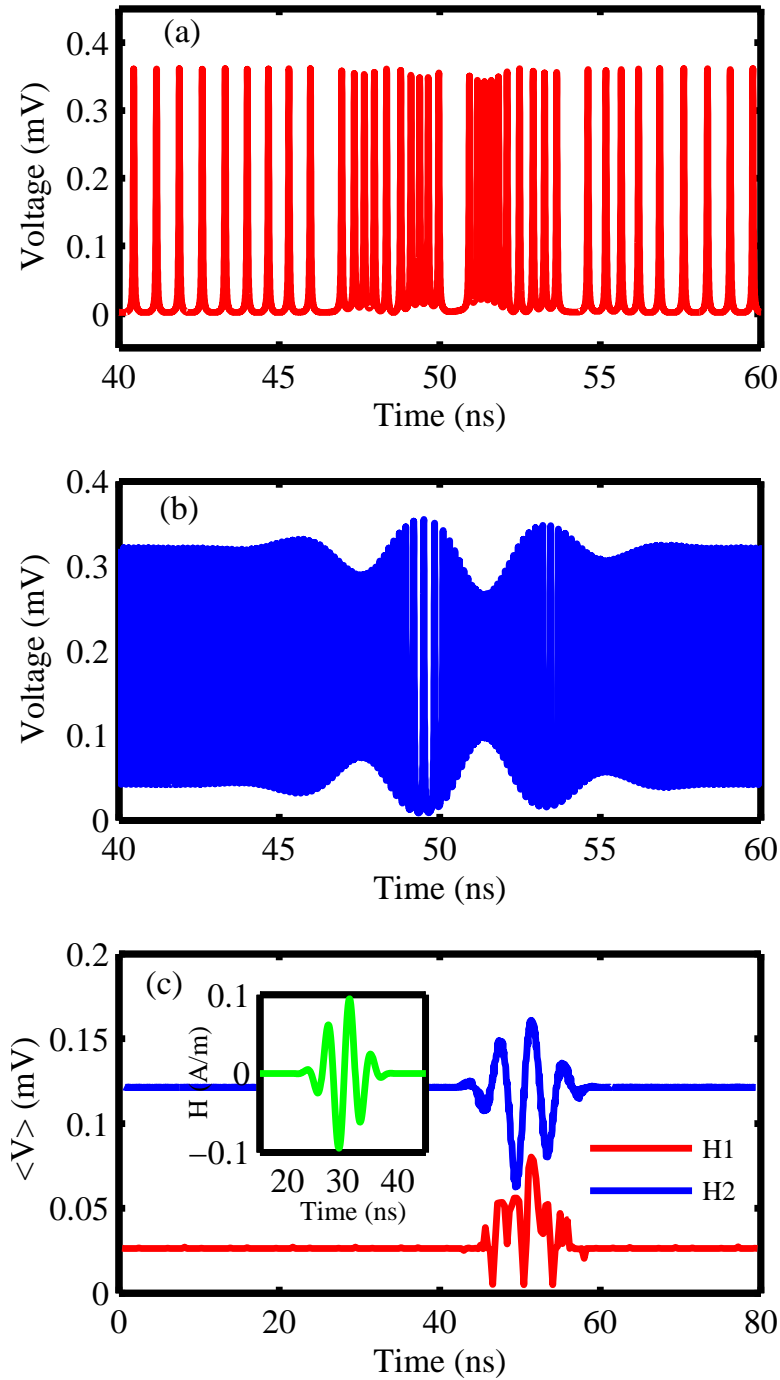
FIGURE 3.42: Comparison of average voltage responses with two different operation magnetic fields. (a) Transient voltage response when the operation static magnetic field $H_1$ is 0.0068 A/m. (b) Transient voltage response when the operation static magnetic field $H_2$ is 0.1 A/m. (c) Comparison of average voltage responses when applying the external electromagnetic signal. The inner figure shows the transmitting broadband signal with a frequency band from 100 MHz to 400 MHz.
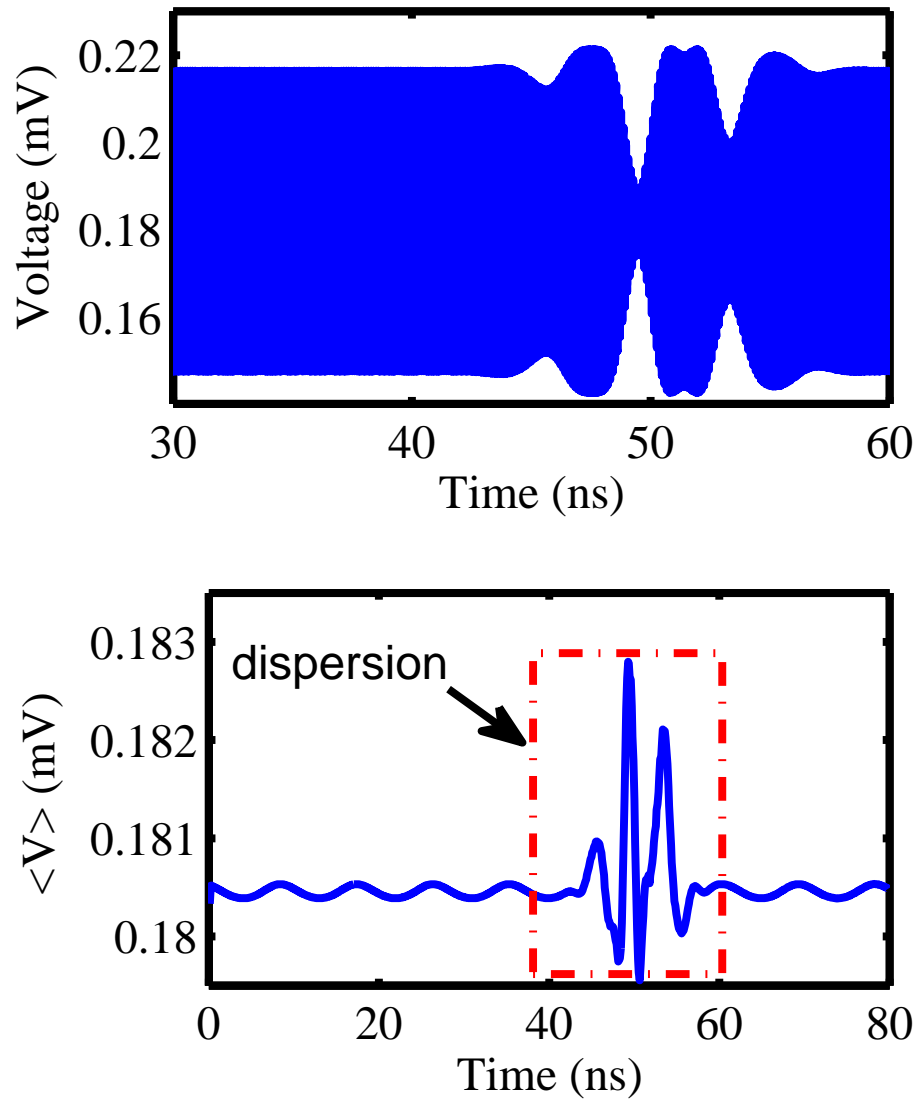
FIGURE 3.43: (Color online) The voltage response of the SQIF. (a) Transient voltage response when the operation static magnetic field $H_3$ is 0.5 A/m. (b) The dispersion is observed for average voltage response.
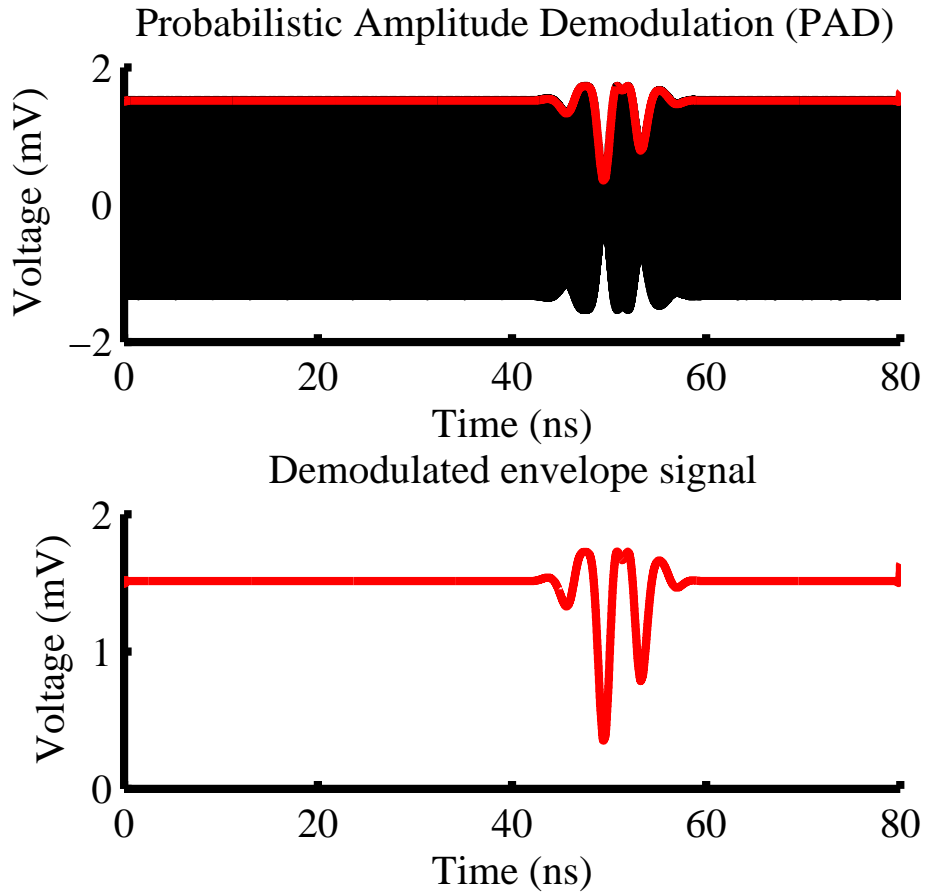
FIGURE 3.44:      (Color online) The envelope waveform of the transient voltage response of the SQIF when the operation static magnetic field $H_3$ is 0.5 A/m. The waveform is extracted by Probabilistic Amplitude Demodulation (PAD) technique[61].

link between the near-field transmitter and the 2D SQIF should be minimized. Since the magnetic flux is related to the product of the surface area and the magnetic field passing through that area, we will use the directional component of the magnetic field as the second constraint. In Fig. 3.41, we illustrate this co-mingled wireless communication system consisting of a 2D SQIF, a far-field transmitter, and a near-field transmitter.

The key challenge for this co-mingled wireless communication system is to design

a non-traditional antenna in the presence of a near-field transmitter. This antenna encounters two major operational constraints: first, it has a minimum magnetic field interference to the nearby 2D SQIF; secondly, the main beam of this antenna should point to the far-field transmitter. Here we assume that the antenna is located at the $xy$ plane and the far-field transmitter is put along the $z$ direction. Many traditional antennas, such as monopoles and patch antennas, can easily satisfy the second far-field radiation constraint; few antennas may meet the first constraints. However, the antenna satisfying both constraints is seldom investigated and poses a practical antenna design challenge for us.

We further assume that the distance between the near-field antenna and the 2D SQIF is about 1000 mm, the detectable magnetic field signal of the 2D SQIF is 0.02 A/m and the minimum magnetic field signal-to-interference ratio of the 2D SQIF is 10 dB. Therefore, related to the first constraint, the interference magnetic field from the near-field antenna should be less than 0.0063 A/m, called the threshold value of a magnetic field of a 2D SQIF.

We proposed an impedance-matched U-slot patch antenna in Fig. 3.45. This antenna has a resonant frequency of 221 MHz and its maximum radiation direction points to the $z$ direction, which satisfies the second constraint. As shown in Fig. 3.46, we found, at the position (-989.0588, -104.0985, 0) mm, a minimum magnetic field value component $H_x = 0.006$ A/m is less than the threshold value 0.0063 A/m. This $H_x$ satisfied the first constraint. Furthermore, we investigated the variation of $H_x$ when the U-slot patch antenna encounters 1 degree title along four directions. In Fig. 3.47, we first gave the comparison of $H_x$ values. We found that the "right" tilt does not affect the value of $H_x$. However, the "up" and "left" tilt angles increase to $H_x$ to 0.0073 A/m and 0.0085 A/m respectively. The "down" tilt decreases $H_x$ to 0.0052 A/m because the ground plane of the U-slot antenna partially acts as the isolation part.
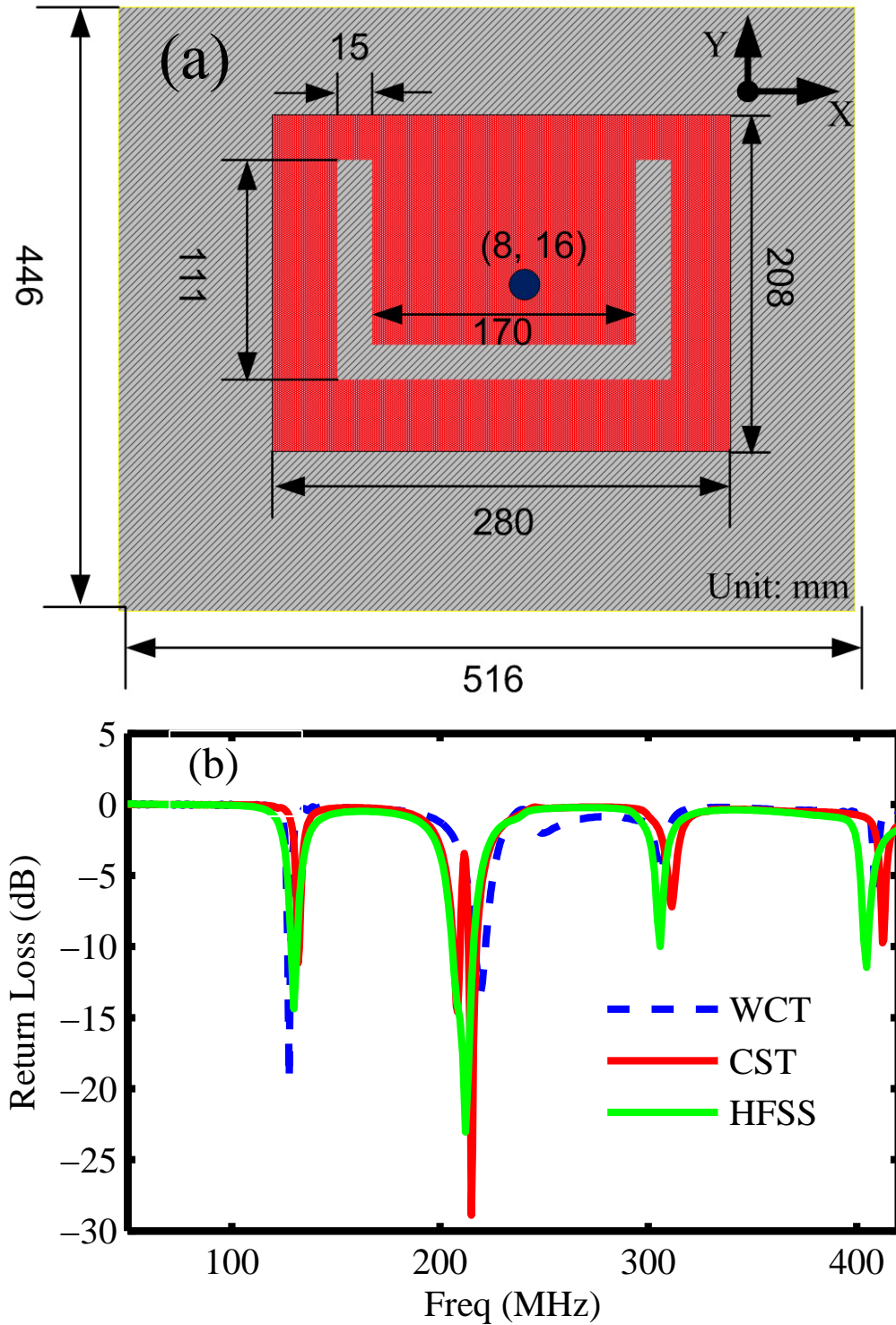
FIGURE 3.45: Proposed impedance-matched antenna. (a) Geometry of antenna configuration. The feed position is at (8,16) mm. $\epsilon_r = \mu_r = 4.5$. (b) The simulated return loss of the antenna in WCT, CST and HFSS. The second resonant frequency is 221 MHz.
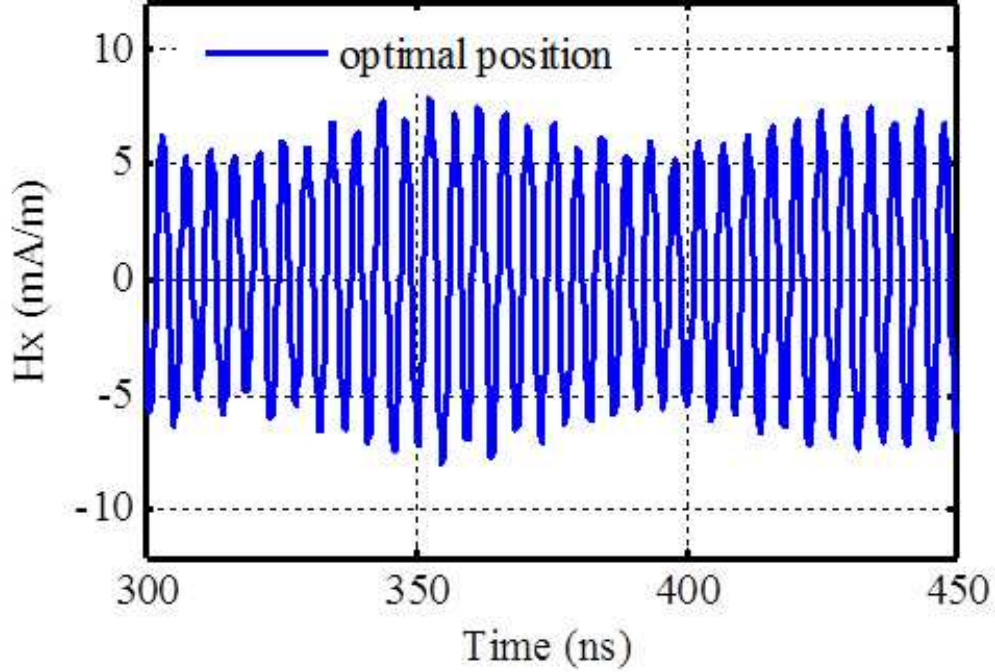
FIGURE 3.46: (Color online) The simulated $H_x$ value at the optimal position (-989.0588, -104.0985, 0) mm.

## 3.11 Inadequacies of Our Simulations

When we discuss the bias current, we have not touch the limiting cases. One direction is toward the higher part of the bias current. That is, we may ask what the saturation bias current is making the device nonfunctional. The opposite direction is toward the lower part of the bias current. In this routine, we could seek the answer what the minimal bias current makes the device work properly. These investigations on bias current operation range would have practical engineering meaning.

## 3.12 A possible Generalization

Our approach has demonstrated the large scale 2D SQIF modelling with supporting more than 5,000 junctions. There is an interesting problem which require 2D SQIF to contain a larger number of junctions, say $> 40,000$ junctions. This action brings
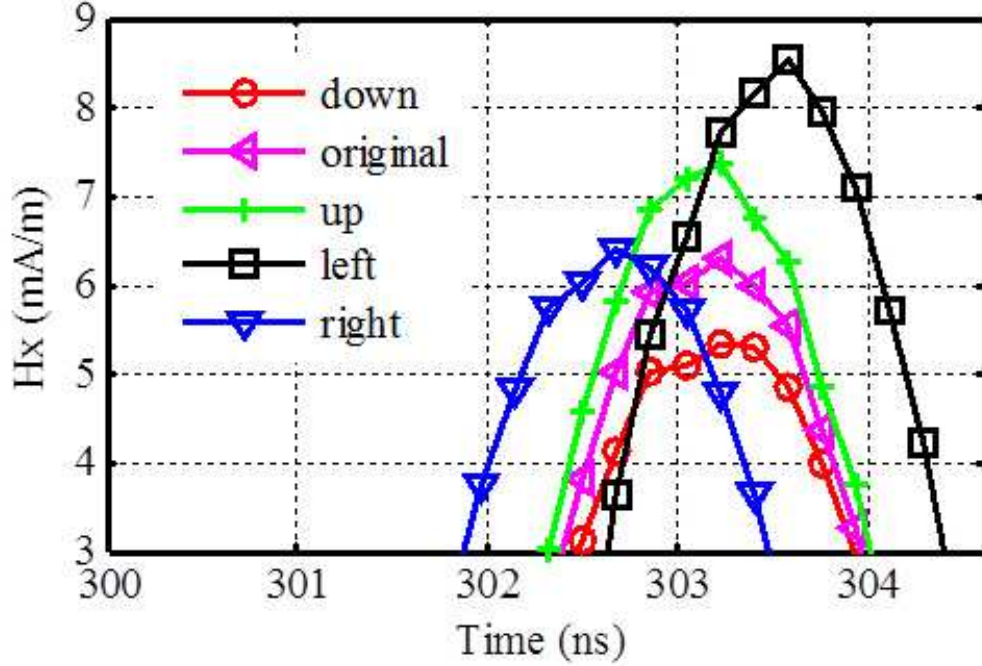
FIGURE 3.47: (Color online) $H_x$ for four tilt directions. Observation points: "left" is at (-989.3634, -121.5489, 0) mm, "right" is at (-985.1201, -86.6481,0) mm, "down" is at (-988.7542, -104.0985, -17.4504) mm, "up" is at (-988.7542, -104.0985, 17.4504) mm.

the computing challenge at the personal computing platform. As a consequence, new computing strategies, such as parallel computing or Graphic Processing Unit (GPU) acceleration, might be utilized in order to reduce the simulation time. The proper solution from the simulation will allow us to design a practical wideband far-field magnetic field sensor in a dynamical electromagnetic environment.

## 3.13   Conclusion

In summary, we developed a complete framework for modeling B-antenna in a dynamic electromagnetic field environment. Because this framework separates the interface and Josephson junction circuit implementation, this strategy accelerates design, analysis and optimization of a 2D SQIF in a dynamic electromagnetic en-

vironment. This work not only allows us to explore the dynamics of a 2D SQIF and evaluate the electrical and geometrical effects, but also allows us to investigate magnetic field interactions between B-antenna and external electromagnetic waves. Our findings on the average voltage response of the device offer compelling evidence that the bias static magnetic field plays a key role in designing an effective far-field magnetic field sensor. Furthermore, our work demonstrates the capability of a 2D SQIF as a dynamic magnetic field-to-voltage transducer [60]. Since this device can function as both a robust and sensitive low noise pre-amplifier as well as an antenna, which only senses the magnetic field component of far-field electromagnetic wave signals, we call it a magnetic-antenna or a B-antenna. Furthermore, we design a co-mingled E and B field antennas system. Our work not only directly benefits the sensor design in Very High Frequency/Ultra High Frequency (VHF/UHF) bands, but also opens a new dimension of novel ultra-sensitive receiving antenna technology.

# Appendix A

## SPICE code: Memristor Model

```
V1  1  101  SIN(0  5.3  1e8)
Rs  101  100  50
V2  100  0  SIN(0  0.5  1.455e9)
*V1  1  0  PULSE(-2  2  0nS  0NS  0nS  10nS  10nS)
Roff  1  2  15k
B1  2  0  V=I(B1)*(-14930)*(V(15))

*The state equation model of the memristor
*Va  10  0  pwl(0  0  0.1  0  0.2  1  100  1  )
B2  0  10  V=V(15)*(1-V(15))*6.0916e11*I(B1)
*B2  0  10  V=1e4*I(B1)*(1-(2*V(15)-1)^20)
*Op-amp
Rin  0  11  1e12
E1  12  0  0  11  1e6
R2  12  13  1k
C2  13  0  1e-20
E2  14  0  13  0  1
R3  14  15  1u

*gain  ratio
R1  10  11  1
C1  15  11  1  IC=0.6V

rload  15  0  1e6
```

.TRAN 0 50ns 0.01ns UIC
.END

# Appendix B

## Matlab Code for Averaging Voltage Response

```
function [res, t] = Smooth(vec, dt, nSmooth, mSkip, iStart)
%% [res, t] = Smooth(vec, dt, nSmooth, mSkip, iStart)
% Please be aware that this only works for the limited
    bandwidth.
% Smooth a signal vector.
% Input:
%   vec      : a singal vector
%   dt       : time step for the vector
%   nSmooth  : smooth width is nSmooth * dt
%   mSkip    : every mSkip * dt to do a smooth
%   iStart   : the first index to smooth, iStart >= 1
%% Output:
%   res      : resultant smoothed signal vector
%   t        : time vector for resultant vector
%% Author: Tian Xiao    WCT.     2010-10-05
%  Modified:  Lin Wang 2012/01/23
if nargin == 4, iStart = 1; end;
len = length(vec);
i = iStart : mSkip : len - nSmooth;
for j = 1 : length(i)
    res(j) = sum(vec(i(j) : i(j) + nSmooth)) / nSmooth;
end
t = i * dt + (iStart - 1 + nSmooth / 2) * dt;
```

# Bibliography

[1] V. I. Arnold. *Ordinary Differential Equations.* New York : Springer-Verlag, Berlin, 3rd edition, 1992.

[2] Constantine A. Balanis. *Antenna Theory : Analysis and Design.* John Wiley, Hoboken, NJ, 3rd edition, 2005.

[3] M. Barahona and C. S. Poon. Detection of nonlinear dynamics in short, noisy time series. *Nature*, 381(6579):215–217, 1996.

[4] Cristoforo Sergio Bertuglia and Franco Vaio. *Nonlinearity, Chaos, and Complexity : the Dynamics of Natural and Social Systems.* Oxford University Press, Oxford ; New York, 2005.

[5] Joseph Blanc and David L. Staebler. Electrocoloration in $SrTiO_3$: Vacancy drift and oxidation-reduction of transition metals. *Phys. Rev. B*, 4(10):3548, Nov 1971.

[6] J. Borghetti, Z. Y. Li, J. Straznicky, X. M. Li, D. A. A. Ohlberg, W. Wu, D. R. Stewart, and R. S. Williams. A hybrid nanomemristor/transistor logic circuit capable of self-programming. *Proc. Natl. Acad. Sci. U.S.A*, 106(6):1699, 2009.

[7] J. Borghetti, G. S. Snider, P. J. Kuekes, J. J. Yang, D. R. Stewart, and R. S. Williams. 'Memristive' switches enable 'stateful' logic operations via material implication. *Nature*, 464(7290):873, 2010.

[8] M. G. Bray and D. H. Werner. Passive switching of electromagnetic devices with memristors. *Appl. Phys. Lett.*, 96:073504, 2010.

[9] H. W. Broer. *Nonlinear Dynamical Systems and Chaos.* Birkhser, Basel;Boston, 1996.

[10] S Bush. Hp nano device implements memristor. *Electronics Weekly*, pages 05–02, 2008.

[11] P. Caputo, J. Oppenlander, C. Haussler, J. Tomes, A. Friesch, T. Trauble, and N. Schopohl. High-performance magnetic field sensor based on superconducting quantum interference filters. *Applied Physics Letters*, 85(8):1389–1391, 2004.

[12] P. Caputo, J. Tomes, J. Oppenlander, C. Haussler, A. Friesch, T. Trauble, and N. Schopohl. Two-tone response in superconducting quantum interference filters. *Ieee Transactions on Applied Superconductivity*, 17(2):722–725, 2007.

[13] P. Caputo, J. Tomes, J. Oppenlander, C. Haussler, A. Friesch, T. Trauble, and N. Schpohl. Superconducting quantum interference filters as absolute magnetic field sensors. *Ieee Transactions on Applied Superconductivity*, 15(2):1044–1047, 2005.

[14] F. l Chernousko. *Control of Nonlinear Dynamical Systems : Methods and Applications*. Springer Berlin Heidelberg, New York, NY, 2008.

[15] I. Chiorescu, P. Bertet, K. Semba, Y. Nakamura, C. J. P. M. Harmans, and J. E. Mooij. Coherent dynamics of a flux qubit coupled to a harmonic oscillator. *Nature*, 431(7005):159–162, 2004.

[16] A. Cho. Quantum mechanics - physicists unveil schrodinger's squid. *Science*, 287(5462):2395–2395, 2000.

[17] L. O. Chua. Memristor - missing circuit element. *IEEE Trans. Circuit Theory*, 18(5):507, 1971.

[18] L. O. Chua and S. M. Kang. Memristive devices and systems. *Proc. IEEE*, 64(2):209, 1976.

[19] J. Clarke and R. H. Koch. The impact of high-temperature superconductivity on squid magnetometers. *Science*, 242(4876):217–223, 1988.

[20] P. A. Cook. *Nonlinear Dynamical Systems*. Prentice Hall, New York, 2nd edition, 1994.

[21] S. Dietrich, M. Angerbauer, M. Ivanov, D. Gogl, H. Hoenigschmid, M. Kund, C. Liaw, M. Markert, R. Symanczyk, L. Altimime, S. Bournat, and G. Mueller. A nonvolatile 2-Mbit CBRAM memory core featuring advanced read and program control. *IEEE J. Solid-State Circuits*, 42(4):839, apr. 2007.

[22] L. Gyorgyi and R. J. Field. A 3-variable model of deterministic chaos in the belousov-zhabotinsky reaction. *Nature*, 355(6363):808–810, 1992.

[23] Wassim M. Haddad and VijaySekhar Chellaboina. *Nonlinear Dynamical Systems and Control : a Lyapunov-based Approach.* Princeton University Press, Princeton, 2008.

[24] T. W. Hickmott. Low - frequency negative resistance in thin anodic oxide films. *J. Appl. Phys.*, 33(9):2669, 1962.

[25] Morris W. Hirsch, Stephen Smale, and Robert L. Devaney. *Differential Equations, Dynamical Systems, and an Introduction to Chaos.* Academic Press, San Diego, CA, 2nd edition, 2004.

[26] P. C. Ivanov, L. A. N. Amaral, A. L. Goldberger, S. Havlin, M. G. Rosenblum, Z. R. Struzik, and H. E. Stanley. Multifractality in human heartbeat dynamics. *Nature*, 399(6735):461–465, 1999.

[27] Sung Hyun Jo, Kuk-Hwan Kim, and Wei Lu. High-density crossbar arrays based on a Si memristive system. *Nano Lett.*, 9(2):870, 2009.

[28] O. Kavehei, A. Iqbal, Y. S. Kim, K. Eshraghian, S. F. Al-Sarawi, and D. Abbott. The fourth element: characteristics, modelling and electromagnetic theory of the memristor. *Proc. R. Soc A*, 466(2120):2175–2202, 2010.

[29] S. D. Keller, W. D. Palmer, and W. T. Joines. Electromagnetic modeling and simulation of a directly modulated patch antenna. *IEEE Antennas Wireless Propag. Lett.*, 9:779, 2010.

[30] M. B. Ketchen. Scanning squid microscopy. *Science*, 272(5265):1087–1087, 1996.

[31] K. Kornev, I. I. Soloviev, J. Oppenlaender, C. Haeussler, and N. Schopohl. The oscillation linewidth and noise characteristics of a parallel superconducting quantum interference filter. *Superconductor Science & Technology*, 17(5):S406–S409, 2004.

[32] V. K. Kornev, I. I. Soloviev, N. V. Klenov, T. V. Filippov, H. Engseth, and O. A. Mukhanov. Performance advantages and design issues of sqifs for microwave applications. *Ieee Transactions on Applied Superconductivity*, 19(3):916–919, 2009.

[33] V. K. Kornev, I. I. Soloviev, N. V. Klenov, and O. A. Mukhanov. High linearity sqif-like josephson-junction structures. *Ieee Transactions on Applied Superconductivity*, 19(3):741–744, 2009.

[34] V. K. Kornev, I. I. Soloviev, N. V. Klenov, and O. A. Mukhanov. Design and experimental evaluation of sqif arrays with linear voltage response. *Ieee Transactions on Applied Superconductivity*, 21(3):394–398, 2011.

[35] V. K. Kornev, I. I. Soloviev, N. V. Klenov, A. V. Sharafiev, and O. A. Mukhanov. Linear bi-squid arrays for electrically small antennas. *Ieee Transactions on Applied Superconductivity*, 21(3):713–716, 2011.

[36] K. K. Likharev. *Dynamics of Josephson Junctions and Circuits*. Gordon and Breach Science Publishers, New York, 1986.

[37] QH Liu. The pstd algorithm: A time-domain method requiring only two cells per wavelength. *Micr. Opti. Tech. Lett.*, 15(3):158–165, 1997.

[38] P. Longhini, S. Berggren, A. Palacios, V. In, and A. L. de Escobar. Modeling non-locally coupled dc squid arrays. *Ieee Transactions on Applied Superconductivity*, 21(3):391–393, 2011.

[39] V. V. Moshchalkov, L. Gielen, M. Dhalle, C. Vanhaesendonck, and Y. Bruynseraede. Quantum interference in a mesoscopic superconducting loop. *Nature*, 361(6413):617–620, 1993.

[40] J. Oppenlaender, C. Haeussler, A. Friesch, J. Tomes, P. Caputo, T. Traeuble, and N. Schopohl. Superconducting quantum interference filters operated in commercial miniature cryocoolers. *Ieee Transactions on Applied Superconductivity*, 15(2):936–939, 2005.

[41] J. Oppenlander, P. Caputo, C. Haussler, T. Trauble, J. Tomes, A. Friesch, and N. Schopohl. Effects of magnetic field on two-dimensional superconducting quantum interference filters. *Applied Physics Letters*, 83(5):969–971, 2003.

[42] J. Oppenlander, C. Haussler, T. Trauble, and N. Schopohl. Sigmoid like flux to voltage transfer function of superconducting quantum interference filter circuits. *Physica C-Superconductivity and Its Applications*, 368(1-4):125–129, 2002.

[43] J. Oppenlander, T. Trauble, C. Haussler, and N. Schopohl. Superconducting multiple loop quantum interferometers. *Ieee Transactions on Applied Superconductivity*, 11(1):1271–1274, 2001.

[44] Terry P. Orlando and Kevin A. Delin. *Foundations of Applied Superconductivity*. Addison-Wesley, Reading, Mass., 1991.

[45] G. F. Oster. Note on memristors. *IEEE Trans. Circuits Syst.*, 21(1):152, 1974.

[46] G. F. Oster and D. M. Auslander. The memristor: A new bond graph element. *Trans. ASME J. Dyn. Syst. Meas. Control*, 94(3):249, 1972.

[47] Q. Ouyang and J. M. Flesselles. Transition from spirals to defect turbulence driven by a convective instability. *Nature*, 379(6561):143–146, 1996.

[48] Stanford R. Ovshinsky. Reversible electrical switching phenomena in disordered structures. *Phys. Rev. Lett.*, 21(20):1450, Nov 1968.

[49] Eduard Reithmeier. *Periodic Solutions of Nonlinear Dynamical Systems : Numerical Computation, Stability, Bifurcation, and Transition to Chaos.* Springer-Verlag, Berlin;New York, 1991.

[50] D. Robbes, Y. Monfort, M. L. C. Sing, D. Bloyet, J. Provost, B. Raveau, M. Doisy, and R. Stephan. The ac josephson effect in constrictions engraved in bulk yba2cu3o7-delta and dc squid operation at 77-k. *Nature*, 331(6152):151–153, 1988.

[51] W. Robinett, M. Pickett, J. Borghetti, Q. F. Xia, G. S. Snider, G. Medeiros-Ribeiro, and R. S. Williams. A memristor-based nonvolatile latch circuit. *Nanotechnology*, 21(23):235203, 2010.

[52] Walter Rudin. *Principles of Mathematical Analysis.* McGraw-Hill, New York, 3d edition, 1976.

[53] V. Schultze, R. IJsselsteijn, H. G. Meyer, J. Oppenlander, C. Haussler, and N. Schopohl. High-t-c superconducting quantum interference filters for sensitive magnetometers. *Ieee Transactions on Applied Superconductivity*, 13(2):775–778, 2003.

[54] A. V. Shadrin, K. Y. Constantinian, and G. A. Ovsyannikov. Quantum interference filters based on oxide superconductor junctions for microwave applications. *Technical Physics Letters*, 33(3):192–195, 2007.

[55] O. V. Snigirev, M. L. Chukharkin, A. S. Kalabukhov, M. A. Tarasov, A. A. Deleniv, O. A. Mukhanov, and D. Winkler. Superconducting quantum interference filters as rf amplifiers. *Ieee Transactions on Applied Superconductivity*, 17(2):718–721, 2007.

[56] S. H. Strogatz. Exploring complex networks. *Nature*, 410(6825):268–276, 2001.

[57] S. H. Strogatz. Exploring complex networks. *Nature*, 410:268–276, 2001.

[58] D. B. Strukov and R. S. Williams. An ionic bottle for high-speed, long-retention memristive devices. *APPL PHYS A-MATER*, 102(4):1033–1036, 2011.

[59] Dmitri B. Strukov, Gregory S. Snider, Duncan R. Stewart, and R. Stanley Williams. The missing memristor found. *Nature*, 453(7191):80, 2008.

[60] John Talvacchio and *et al. Scaling of SQIF properties with parallel and series SQUIDs.* Presented at Applied Superconductivity Conference, Washington, DC, 2010.

[61] R.E. Turner and M. Sahani. Demodulation as probabilistic inference. *IEEE Audio, Speech, Language Process.*, 19(8):2398–2411, 2011.

[62] X. Wang and Y. Chen. Spintronic memristor devices and applications. *DATE*, 2010.

[63] X. B. Wang, Y. R. Chen, Y. Gu, and H. Li. Spintronic memristor temperature sensor. *IEEE Electron Device Lett.*, 31(1):20–22, 2010.

[64] X. B. Wang, Y. R. Chen, H. W. Xi, H. Li, and D. Dimitrov. Spintronic memristor through spin-torque-induced magnetization motion. *IEEE Electron Device Lett.*, 30(3):294–297, 2009.

[65] Rainer Waser and Masakazu Aono. Nanoionics-based resistive switching memories. *Nature Mater.*, 6(11):833, 2007.

[66] Stephen Wiggins. *Introduction to Applied Nonlinear Dynamical Systems and Chaos.* Springer, New York, 2nd edition, 2003.

[67] Q. F. Xia, W. Robinett, M. W. Cumbie, N. Banerjee, T. J. Cardinali, J. J. Yang, W. Wu, X. M. Li, W. M. Tong, D. B. Strukov, G. S. Snider, G. Medeiros-Ribeiro, and R. S. Williams. Memristor-CMOS hybrid integrated circuits for reconfigurable logic.

[68] J. J. Yang, M. D. Pickett, X. M. Li, D. A. A. Ohlberg, D. R. Stewart, and R. S. Williams. Memristive switching mechanism for metal/oxide/metal nanodevices. *Nat. Nanotechnol.*, 3(7):429–433, 2008.

[69] W. J. Yao and Y. X. E. Wang. An integrated antenna for pulse modulation and radiation.

# Biography

**Personal Information:**

1. Name: Lin Wang

2. Date of Birth: Jan 21, 1980.

3. Place of Birth: Sichuan, China.

**Education:**

1. Ph.D., Electrical and Computer Engineering, Duke University, USA, Dec 2013.

2. M.S., Radio Physics, University of Electronic Science and Technology of China, Chengdu, P.R. China, 2005.

3. B.S., Microwave Engineering University of Electronic Science and Technology of China, Chengdu, P.R. China, 2002.

**Patents & Invention Disclosure Forms:**

1. **L. Wang**, M. Q. Yuan and Q.H. Liu, "Memristor Models in Antenna and Microwave Engineering,"(IDF) The Office of Licensing & Ventures, Duke University, 2013.

2. **L. Wang**, M. Q. Yuan and Q.H. Liu, "Dynamical Magnetic field Detector System Model,"(IDF) The Office of Licensing & Ventures, Duke University, 2013.

3. **L. Wang**, M. Q. Yuan and Q.H. Liu, "2D Superconducting Quantum Filter Antenna,"(IDF) The Office of Licensing & Ventures, Duke University, 2013.

4. **L. Wang** and Q.H. Liu, "Multi-Band Antenna and Versatile Grounding Methods for Multiple Radio Services," August 2010 (# CN 201789063 U).

5. **L. Wang** and Q.H. Liu, "Dual Frequency Electrically Small Antenna," July 2010 (# CN 201732864 U).

6. **L. Wang**, L. Y. Li and Q.H. Liu, "Dual Frequency Electrically Small Antenna," December 2010 (#CN 101916912A).

**Publications:**

1. **L. Wang**, Q. H. Liu, W. T. Jiones, and M. Q. Yuan, "Superconducting Quantum Interference Filter Antennas," (Submitted to IEEE Transactions on Applied Superconductivity).

2. **L. Wang**, Q. H. Liu, W. T. Jiones, and M. Q. Yuan, "Broadband Electromagnetic Radiation Modulated by Dual Memristors," *IEEE Antennas Wireless Propag. Lett.*, vol.10, pp.623-626, 2011.

3. **L. Wang**, M. Q. Yuan and Q. H. Liu, "A Dual-Band Printed Electrically Small Antenna Covered by Two Capacitive Split-Ring Resonators," *IEEE Antennas Wireless Propag. Lett.*, vol.10, pp.824-826, 2011.

4. **L. Wang**, M. Q. Yuan and Q. H. Liu, "Modeling 2D Superconducting Quantum Interference Filter Array in a Dynamic Magnetic Field Environment," *2012 Applied Superconductivity Conference*, Portland, Oregon, USA, Oct 2012. (**Best** presentation of the session)

5. **L. Wang**, Q. H. Liu, W. T. Jiones and M. Q. Yuan, "Magnetic Antenna Based on Two Dimensional DC Superconducting Quantum Interference Filter," 2013 APS/URSI Symposium, Lake Buena Vista, Florida, USA, July 2013.

6. **L. Wang**, Q. H. Liu, W. T. Jiones and M. Q. Yuan, "Two Dimensional DC Superconducting Quantum Interference Filter Framework," 2013 APS/URSI

Symposium, Lake Buena Vista, Florida, USA, July 2013.

7. **L. Wang**, Q. H. Liu, W. T. Jiones and M. Q. Yuan, "Introduction to B-antenna," 2013 APS/URSI Symposium, Lake Buena Vista, Florida, USA, July 2013.

8. **L. Wang** and Q. H. Liu, "On Microstrip Patch Antenna Miniaturization Using the Impedance-matched Magnetodielectric Substrate," 2011 APS/URSI Symposium, Spokane, Washington, USA, July 2011.

9. J. H. Deng, **L. Wang** and Q.H. Liu, "A Macromodel of Memristor using Symbolically Defined Devices," *Applied Mechanics and Materials*, vol.195-196, pp.245-248, 2012.

10. Y.J Ren, **L. Wang** and Q. H. Liu, "Design of X-band Wideband Linear Antenna Array with Reduced Number of Antenna Elements," 2011 APS/URSI Symposium, Spokane, Washington, USA, July 2011.

11. **L. Wang** and Q. H. Liu, "Nonlinear Memristors Loaded Circular Loop Antenna," 2011 APS/URSI Symposium, Spokane, Washington, USA, July 2011.

12. **L. Wang** and Q. H. Liu, "A Multi-band Integrated Antenna Subsystem for Smartbook and Smartpad Applications," 2010 APS/URSI Symposium, Toronto, Ontario, Canada, July 2010.

13. **L. Wang**, L.Y. Li and Q. H. Liu, "A Dual-Frequency Printed Electrically Small Antenna Unit," 2010 APS/URSI Symposium, Toronto, Ontario, Canada, July 2010.

14. **L. Wang** and B. Z. Wang, "A Tri-band PIFA Antenna for Mobile Handset Application," 2006 China-Japan Joint Microwave Conference Proceedings, Chengdu, China, August 2006

101